TECHNISCHE UNIVERSITÄT WIEN

MASTER THESIS

Characterisation of the deforming behaviour of titanium alloys for additive manufacturing

Conducted for the attainment of the academic degree of a
Diplom-Ingenieur (Dipl.-Ing.)

submitted at

TU Wien, Faculty of Technical Chemistry
Institute of Chemical Technologies and Analytics

supervised by

Ao.Univ.Prof. Dipl.-Ing. Dr.techn. Christian Edtmaier
and
Dipl.-Ing. Ella Staufer

by

Elisabeth Ballók
Matriculation number 11817170

Vienna, 2025

Affidavit

I declare in lieu of oath, that I wrote this thesis and carried out the associated research myself, using only the literature cited in this volume. If text passages from sources are used literally, they are marked as such. I confirm that this work is original and has not been submitted for examination elsewhere, nor is it currently under consideration for a thesis elsewhere. I acknowledge that the submitted work will be checked electronically-technically using suitable and state-of-the-art means (plagiarism detection software). On the one hand, this ensures that the submitted work was prepared according to the high-quality standards within the applicable rules to ensure good scientific practice 'Code of Conduct' at the TU Wien. On the other hand, a comparison with other student theses avoids violations of my personal copyright.

Vienna, 2025
Elisabeth Ballók

Danksagung

Zu Beginn möchte ich mich herzlich bei Ao.Univ.Prof. Dipl.-Ing. Dr.techn. Christian Edtmaier bedanken, nicht nur für die Betreuung dieser Diplomarbeit, sondern bereits auch meiner Bachelorarbeit. Ich bin dankbar, dass ich die Gelegenheit hatte, meine ersten Erfahrungen im Fachgebiet zu sammeln und mit vielen großartigen Menschen zusammenzuarbeiten. Mein Dank gilt zudem den Projektpartnern für ihre wertvollen Einblicke und ihre Expertise zu diesem Thema.

Meine Zeit am Institut wäre ohne die entstandenen Freundschaften nicht dieselbe gewesen. Ich danke allen für die bereichernden und intellektuellen Gespräche, vor allem die nach der Arbeit. Besonders danken möchte ich Ella Staufer und Nico Moser; nicht nur für ihre fachlichen Ratschläge, sondern vor allem für die gemeinsame Zeit. Ich hatte Spaß.

Ich danke meinem Freund Daniel, dass er mich immer zum Lachen bringen kann. Und meiner Therapeutin, die mir gezeigt hat, dass alles halb so schlimm ist.

Abschließend möchte ich meiner Familie danken, besonders meinen Eltern. Meinem Vater, der mir bis spät in die Nacht Hochofenprozesse erklärt hat und der immer für mich da war. Meiner Mutter, die mir gezeigt hat, dass ich alles erreichen kann und die immer für mich da ist. Vielen Dank!

Abstract

Titanium holds significant importance in the aerospace sector due to its exceptional properties, such as high specific strength, low density, and good corrosion resistance. In recent years, wire arc additive manufacturing (WAAM) has gained significant attention as a promising, cost-effective technique for fabricating near-net shape components. To effectively produce the wire, mechanical properties, such as ductility, are required. The addition of zirconium to titanium reportedly enhances ductility while retaining good mechanical properties. The deformation behaviour and the microstructural changes during the wire production process have to be analysed to ensure the desired mechanical properties for further processing.

Zirconium, also in the form of ZrH_2 and ZrO_2, was added as an alloying element in various contents along with copper. The samples were fabricated using different manufacturing methods like vacuum arc furnace, vacuum sintering and hot extrusion. To analyse the deformation behaviour, deformation dilatometry tests were performed at various temperatures and strain rates. A cast material in the composition of Ti5.9Cu2Fe2Al, manufactured by an external company, was deformed by hot extrusion and caliber rolling. The microstructure of samples was characterized using optical and scanning electron microscopy. The formed phases were characterized through XRD measurements. Furthermore, the c/a ratio as a function of Zr and the progression of crystallite size during deformation were analyzed. Vickers hardness HV10 and Archimedes density measurements were performed.

The addition of 5 wt% zirconium decreased hardness by 30 HV10 indicating higher ductility. The hardness increased with increasing Zr content due to the progressive grain refinement. The deformation dilatometry tests did not indicate any dynamic recovery or dynamic recrystallization, as no steady flow stress was measured. The true stress increases with increasing strain rate and decreasing temperature. During the rolling process, the microstructure of Ti5.9Cu2Fe2Al exhibited elongation when preheated to 800 °C, while a significant grain refinement was observed at 1000 °C indicating dynamic recrystallization. The grain refinement is evident in the hardness increase from 300 HV10 in the cast material to 520 HV after the last deformation step.

Further analyses of the investigated alloys are necessary to determine the mechanical properties, like tensile strength and elongation, the microstructural stability and consequently their suitability for wire drawing and additive manufacturing.

Deutsche Kurzfassung

Titan ist in der Luft- und Raumfahrt aufgrund seiner außergewöhnlichen Eigenschaften wie hohe spezifische Festigkeit, geringe Dichte und gute Korrosionsbeständigkeit von großer Bedeutung. In den letzten Jahren hat das Wire Arc Additive Manufacturing (WAAM) als vielversprechende und kosteneffiziente Technik zur Herstellung von "near-net shape" Bauteilen große Aufmerksamkeit erlangt. Um den Draht effektiv herzustellen, sind gewisse mechanische Eigenschaften wie Duktilität erforderlich. Das Analysieren der Mikrostruktur nach der Verformung is erforderlich, um die gewünschten mechanischen Eigenschaften für die weitere Verarbeitung zu gewährleisten.

Aus der Literatur ist bekannt, dass die Zugabe von Zirkonium zu Titan die Duktilität verbessert, wobei die guten mechanischen Eigenschaften erhalten bleiben. Daher wurde Zirkonium, auch in Form von ZrH_2 und ZrO_2, als Legierungselement zusammen mit Kupfer hinzugefügt. Die Proben wurden mit verschiedenen Fertigungsverfahren wie Vakuumlichtbogenofen, Vakuumsintern und Warmstrangpressen hergestellt. Zur Analyse des Verformungsverhaltens wurden Verformungsdilatometrietests bei verschiedenen Temperaturen und Verformungsgeschwindigkeit durchgeführt. Ein gegos-senes Material in der Zusammensetzung Ti5,9Cu2Fe2Al, das von einem externen Unternehmen hergestellt wurde, wurde durch Warmstrangpressen und Kaliberwalzen verformt. Die Mikrostruktur der Proben wurde durch optische Mikroskopie sowie Rasterelektronenmikroskopie analysiert. Die gebildeten Phasen wurden durch XRD-Messungen charakterisiert. Außerdem wurden das c/a-Verhältnis in Abhängigkeit des Zr Gehalts und die Entwicklung der Kristallitgröße während der Verformung analysiert. Die Vickershärte HV10 und die Archimedische Dichte wurden bestimmt.

Der Zusatz von 5 Gew.-% Zirkonium verringerte die Härte um 30 HV10, was auf eine höhere Duktilität hindeutet. Die Härte nahm mit steigendem Zr-Gehalt aufgrund der fortschreitenden Kornverfeinerung zu. Die Verformungsdilatometrietests ergaben keine Hinweise auf eine dynamische Erholung oder dynamische Rekristallisation, da keine gleichmäßige Fließspannung gemessen wurde. Die echte Spannung nimmt mit steigender Dehnungsrate und sinkender Temperatur zu. Eine Dehnung des Gefüges in Walzrichtung konnte beim Kaliberwalzen von Ti5,9Cu2Fe2Al bei 800 °C beobachtet werden. Der Walzprozess bei 1000 °C führte zu einer deutlichen Kornverfeinerung, was auf eine dynamische Rekristallisation hindeutet. Die Kornverfeinerung zeigt sich ebenfalls im Anstieg der Härte von 300 HV10 im Gussmaterial auf 520 HV10 nach dem letzten Verformungsschritt.

Weitere Analysen der hergestellten Legierungen sind erforderlich, um die mechanischen Eigenschaften, wie Zugfestigkeit und Dehnung, sowie die mikrostrukturelle Stabilität zu bestimmen. Die Eignung der Legierungen für das Drahtziehen und die additive Fertigung kann nach weiteren Messungen beurteilt werden.

Contents

1 Introduction

In 1791, William Gregor made a significant discovery by extracting impure titanium oxide by eliminating iron from ilmenite ($FeTiO_3$). Martin Heinrich Klaproth obtained titanium oxide from rutile (TiO_2) in 1795. He named the element titanium in reference to the titans of Greek mythology. The first extraction of pure titanium was achieved by Matthew Albert Hunter in 1910 through the heating of titanium tetrachloride ($TiCl_4$) with sodium. Wilhelm Justin Kroll revolutionized the extraction of titanium by introducing the 'Kroll process' a commercial method that used magnesium as a reducing agent to reduce $TiCl_4$ [1].

Nowadays, titanium is utilized in various fields due to the versatile material properties. The aerospace sector benefits from the low density, high specific strength and elevated temperature capabilities, the latter is important for the use in turbines [2]. Biomedical and dental engineering are other prominent sectors. Biocompatibility, corrosion and wear resistance are beneficial for these purposes [3].

The processing of Ti and Ti alloys poses many difficulties, such as low thermal conductivity and high affinity to interstitial elements like oxygen and hydrogen, which can degrade mechanical properties like ductility. Therefore, additive manufacturing is gaining more importance as a near-net shape manufacturing process that is cost-effective due to the decrease of the 'buy-to-fly' ratio [4].

One can differentiate the process by the used starting material - powder or wire - and the heat source - electron beam, laser, or electric arc [2]. The AM technologies using powder as the starting material guarantee a good dimensional accuracy, however the deposition rate is low at 0.12 to 0.6 kg/h. To ensure a economical production of aerospace parts, a deposition rate of several kg/h has to be ensured. Therefore, wire arc additive manufacturing (WAAM) is the preferred production method [4].

Ti wires are typically produced by rolling, extrusion or drawing [5]. As high forces are necessary for the wire production, the deformation behaviour of Ti alloys is analysed in this thesis in relation to microstructure and, consequently, mechanical properties, mainly hardness. Furthermore, Ti-Zr alloys are produced using different Zr sources and production methods, as the addition of Zr promises good ductility properties.

2 Theoretical Background

2.1 Titanium and Titanium Alloys

Titanium is classified as a nonferrous and light metal with a density of 4.51 g cm^{-3}. Certain properties make titanium alloys particularly interesting in various fields: high specific strength, high melting point and excellent corrosion resistance. Due to the high melting temperature of 1670 °C in contrast to Al (660 °C), the main representative of the light metals, titanium can be used for high-temperature applications. However, there is a temperature limitation of about 600 °C, as oxygen can diffuse through the oxide layer and cause embrittlement [6]. Because of the strong affinity to oxygen, an extremely thin oxide layer (α-case) develops at room temperature in the presence of air. The α-case leads to good corrosion resistance, making Ti alloys resistant to aggressive environments, such as coastal or acidic environments [6]. Renowned for its exceptional properties, titanium finds extensive applications in diverse fields, with a primary focus on the aerospace sector due to the high specific strength. Beyond aviation, titanium and its alloys are increasingly used in areas such as biomedical engineering, marine and shipbuilding or sports and leisure [1].

Titanium has two different modifications. At low temperatures titanium crystallizes in a hexagonal close packed (hcp) lattice and is referred to as α-titanium. Above the so-called α/β transus temperature a body centered cubic (bcc) structure, β-titanium, is stable. The α/β transus temperature is determined by the composition of the alloy, and its substitutional and interstitial elements, however for pure titanium it is 882 $\pm$ 2 °C. The lattice parameters for α-Ti are a = 2.95 Å and c = 4.68 Å and the c/a ratio is 1.587 [6, 7]. The different crystal lattices influence the properties of the phases and consequently of the alloys. For example, the β phase has a higher ductility but a moderate tensile yield strength. On the other hand, the α phase is relatively brittle, however it exhibits higher strength [1, 8].

Figure 1 shows a classification of alloying elements regarding their influence on phase stabilization and the α/β transus temperature. Zirconium and tin have little to no influence on the α/β transus temperature, therefore they are referred to as neutral elements. Certain elements, such as aluminium and oxygen, stabilize the α phase at higher temperatures, therefore they are called α stabilizers. Aluminium is the most used α stabilizer, due to its large solid solubility in both phases and its frequent occurrence [6]. Al is also an effective strengthener and it lowers the density [8]. β stabilizers decrease the α/β transus temperature, with a distinction between β isomorphous and β eutectic elements. Molybdenum, vanadium or niobium as β isomorphous elements are of significant importance due to their high solubility in titanium [1]. Sufficient alloying element content can stabilize β-Ti to room temperature [6]. This thesis focuses on the β eutectoid elements such as copper and iron, because of their formation of intermetallic precipitations (see Chapter 2.3.1).

Depending on the amount of each stabilizer, five types of titanium alloys can be introduced: α-Ti, near α-Ti, $\alpha + \beta$ Ti, near β-Ti and β-Ti. Alloy categorized in $\alpha + \beta$-Ti contain about 4 to 6 % of β stabilizers, with alloy Ti6Al4V (Ti64) as the most prominent representative. This alloy is most widely used, partly because it has been extensively studied and characterized, partly due to its excellent combination

of properties of the α and β phase. Typically $\alpha + \beta$ Ti alloys are weldable, have high strength, good toughness and still retain titanium's low density, because of the moderate percentage of β stabilizers. The microstructure can be characterized in three different types: lamellar, equiaxed or a combination of both (bi-modal). With heat treatments the microstructure and therefore the properties can be influenced [1].

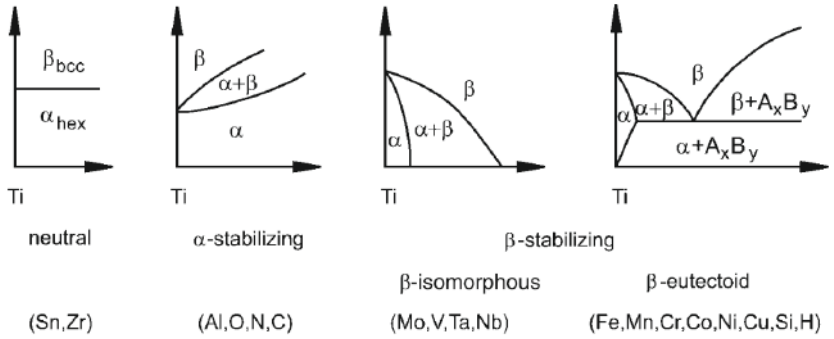

Figure 1: Classification of alloying elements regarding their influence on phase stabilization and the α/β transus temperature [1].

2.2 Wire arc additive manufacturing - WAAM

Titanium poses challenges in traditional fabrication methods, such as machining, casting and forging, due to its properties. For example, during hot working or machining, oxygen dissolves easily in titanium due to its high solubility and affinity. Additional challenges arise from its low elastic modulus, low thermal conductivity and especially the high reactivity with ceramic crucible material. Furthermore, molten titanium is highly viscous, affecting the casting process unfavorably and potentially leading to the formation of pores during solidification [8].

Additive manufacturing (AM) is an alternative to the traditional fabrication methods and is increasingly gaining attention. AM can manufacture near-net shape parts cost effectively due to the decrease of the 'buy-to-fly' ratio [4].

The AM processes can be categorized by the used starting material - powder or wire - and the heat source - electron beam, laser or electric arc [2]. The AM technologies using powder as the starting material guarantee a good dimensional accuracy, however the deposition rate is low at 0.12 to 0.6 kg/h. To ensure an economical production of aerospace parts, a deposition rate of kg/h has to be ensured. Therefore, wire arc additive manufacturing (WAAM) is the preferred production method [4].

A typical WAAM process consists of three stages, which can be modified to ensure the optimal manufacturing process. First a model and the production steps have to be calculated and programmed with a software system. Then the material in form of a wire can be deposited on a substrate with an electric arc as the heat source. Figure 2 depicts a schematic WAAM system. The WAAM systems have to be adjusted to the respective element/alloy. For titanium a closed chamber of tracing shielding device have to be used to ensure an inert atmosphere during the process

to prevent oxidation. The last stage is a post-heat or post-mechanical treatment [8, 9].

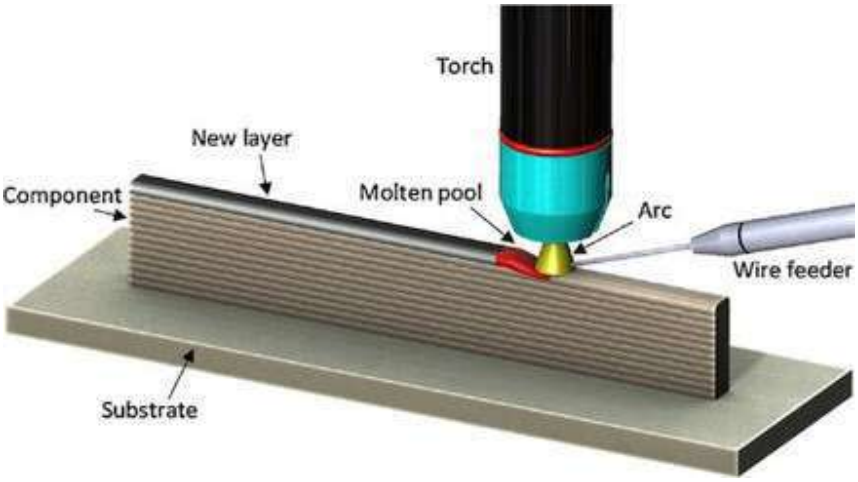

Figure 2: Schema of a wire arc additive manufacturing (WAAM) process [9]

There are various advantages of WAAM including the production of near-net-shape components without molds. Compared to powder-based additive manufacturing processes, WAAM has a high deposition rate, high material utilization and short production lead time [8].

Disadvantages of WAAM are insufficient dimensional accuracy and surface quality, hence post-treatments are necessary [4]. Due to the slow cooling rate, successive remelting and solidification thermal cycles, unwanted microstructure changes can occur such as columnar grain growth. The columnar grains influence the strength and anisotropy, however there are various approaches to minimize grain growth. For example, a higher feed speed favours the formation of equiaxed grains. With this method more nucleation sides are available, therefore the growth of the columnar grains can be restrained. Another approach is the addition of alloying elements (< 0.13 wt%) as nucleation particles like boron or carbon that refine the columnar grains [8, 9]. It is to be noted that with boron or carbon, the columnar grains remain as there is no full columnar to equiaxed transition. With the addition of copper the eutectoid formation of $\beta \rightarrow \alpha + Ti_2Cu$ inhibts the columnar grain growth (see Chapter 2.3.1) [10].

2.3 Alloying elements

2.3.1 Copper

As discussed in the previous chapter, the WAAM process has a disadvantage of forming columnar grains, which are undesirable because of the anisotropic mechanical properties. The addition of copper is a promising method to inhibit the formation of columnar grains.

Figure 3 shows the calculated phase diagram for Ti-Cu alloys. An eutectoid transformation $\beta \rightarrow \alpha + Ti_2Cu$ can be seen at 6.5 wt% Cu at approximately 800 °C. This reaction is an active eutectoid transformation, meaning that copper diffuses fast in titanium. Therefore the eutectoids can form even during rapid cooling rates, which take place in the WAAM process. This characteristic can result in a very fine eutectoid microstructure, which improves strength and ductility of the material [11].

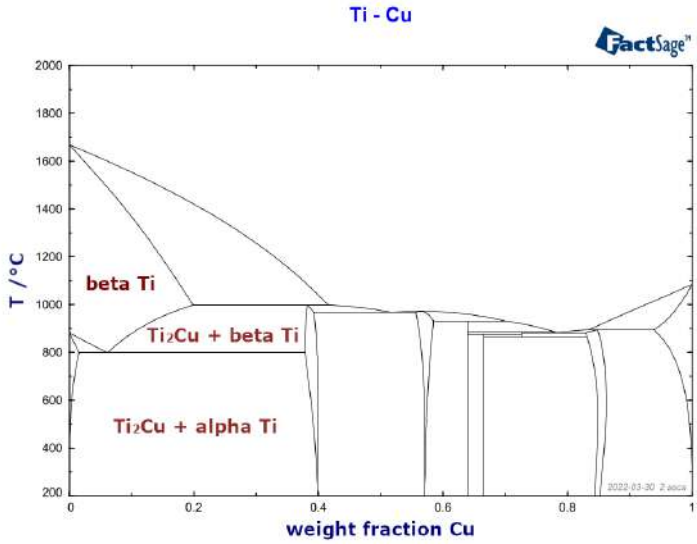

Figure 3: Calculated phase diagram for Ti-Cu (FactSage)

Zhang et al. [10] report, that the addition of copper resulted in a complete transformation of columnar grains into equiaxed grains and also in the refinement of the prior β grains. This result was obtained after the laser metal deposition process, hence no post treatments or process adaptations were necessary.

It is to be noted, that even despite the active eutectoid transformation, martensite α' can still form due to the rapid cooling in additive manufacturing processes. Martensite α' is undesirable due to its high strength but low ductility. However, after the deposition of layers, the cooling rate from the β phase decreases continuously during the cyclic heating, enabling the formation of eutectoid Ti_2Cu [10, 11].

2.3.2 Zirconium

Titanium and zirconium, both belonging in the group IV in the periodical table, exhibit similarities regarding their chemical properties. Both elements transform from

a hexagonal α to a body centered cubic β structure with increasing temperature. Their atomic diameters are alike with 2.92 Å for Ti and 3.20 Å for Zr. The lattice ratio c/a for α-Ti is 1.58 and 1.59 for α-Zr [6, 12]. Taking these properties into consideration, the complete solid solubility of Zr in α and β-Ti is not surprising, which is evident in the with FactSage calculated phase diagram of Ti and Zr shown in Figure 4. Zr is incorporated into the α-Ti lattice substitutionally, resulting in an increase in the lattice parameters a and c, however the c/a ratio remains at 1.58 [12].

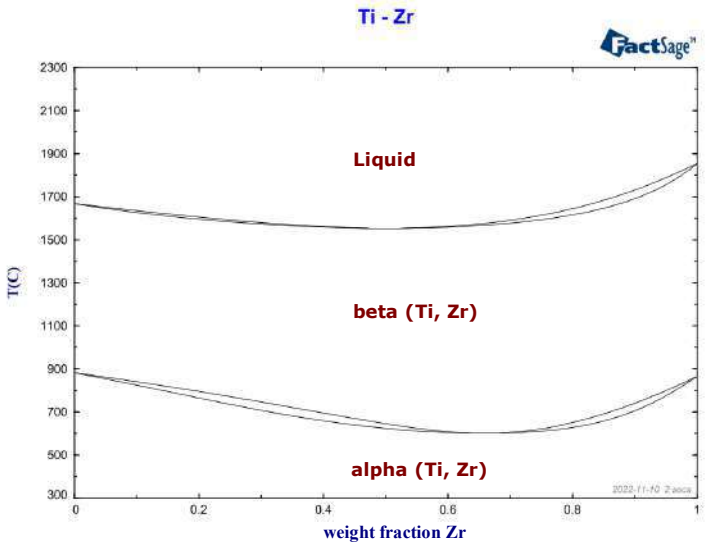

Figure 4: Calculated phase diagram for Ti-Zr (FactSage)

Furthermore, mechanical properties of the two elements are comparable, such as good corrosion resistance and biocompatibility, making the Ti-Zr alloy especially suitable for medical applications [13].

The addition of Zr to Ti is promising, because it leads to grain refinement and improvement of ductility while remaining high strength. The mechanism of the grain refinement is likely due to solute drag mechanism relating to slow diffusion of Zr in α-Ti. The slow diffusion rate leads to an decrease of the velocity of migrating grain boundaries (GB), which causes an enrichment of Zr at GB [14]. To minimize the accumulation of Zr at GB water quenching after heat treatment is advised [15]. The good ductility can be explained by the activation of pyramidal slips [16].

Alshammari et al. [17] investigated the influence of Zr up to 10 wt% in Ti matrix. The binary samples were pressed and vacuum sintered at 1300 °C for 2 h. An increasing grain refinement of the prior β grains and the α lamellae with increasing Zr content could be observed. The grain refinement as well as solid solution strengthening lead to an increase of hardness and strength with higher Zr addition. The yield stress and the ultimate tensile strength reach, respectively, a maximum of 587 MPa and 651 MPa at 10 wt% Zr. The ductility increases up to the addition of 6 wt% Zr to 19.9 %, afterwards a decrease can be observed.

Kondoh et al. [15] observed a formation of fine and equiaxed α-Ti grains with the addition of up to 10 wt% ZrH_2. The use of ZrH_2 as a source of zirconium was justified by the alleged combustion of pure zirconium during the milling process due to its high reactivity. The observed samples were manufactured using spark plasma sintering (SPS), subsequent dehydrogenation and homogenization heat treatments and lastly hot extrusion.

SPS at 1100 °C led to the dissolution of ZrH_2 and the installation of Zr in the Ti matrix, as observed in XRD measurements. The thermal decomposition temperature range of ZrH_2 is 600 to 1000 °C [18]. The low solubility of hydrogen in Ti results in a precipitation of TiH_2. A vacuum dehydrogenation heat treatment at 1000 °C follows to decompose the formed TiH_2. The main decomposition of TiH_2 takes place in the temperature range of 440 to 780 °C and ceases at 960 °C [19, 20]. Through SEM-EDS measurements, an H content after the dehydrogenation heat treatment of less than 0.01 wt% was observed. SEM mappings and XRD measurements showed the decomposition of hydrides and uniform solution of Zr in the Ti matrix after the homogenization heat treatment at 1000 °C.

The grain refinement was induced by dynamic recrystallisation (DRX) during hot extrusion. With the addition of 10 wt% ZrH_2 a yield stress of 852.7 MPa, an ultimate tensile strength of 858.2 MPa and an elongation of 25.3 % was achieved. As previously stated, the primary mechanisms contributing to the strengthening of Ti-Zr alloys include grain refinement and the incorporation of Zr through solid solution [15, 21] .

Issariyapat et al. [22] manufactured Ti alloys with up to 10 wt% ZrH_2 by laser powder bed fusion, with similar results in strength, but a lower results in ductility. The sample with 3 wt% ZrH_2 exhibits a good strength-to-ductility ratio, with yield stress of 655.6 MPa, an ultimate tensile strength of 741.1 MPa and an elongation of 21.0 %.

Another option for incorporation zirconium is the addition of ZrO_2. In addition to Zr, oxygen enhances as an interstitial element the strength through grain refinement and solid solution hardening. Kondoh et al. [23] investigated Ti-ZrO_2 samples produced by SPS, subsequent homogenization heat treatment and hot extrusion. The addition of 2 wt% ZrO_2 resulted in a yield stress of 941.1 MPa, an ultimate tensile strength of 1042.8 MPa and an elongation of 26.4 %. DTA indicates an instability of ZrO_2 at 780 °C. XRD measurements did not detect ZrO_2 after heat treatment above 800 °C, confirming the dissolution of ZrO_2. Zr and O incorporated in the Ti lattice due to their high solubility. The solid solubility of ZrO_2 in α-Ti should be up to 20 wt% ZrO_2 at low temperatures. With higher ZrO_2 content precipitation of ZrO_2 can be found [24].

Han et al. [25] investigated the addition of ZrO_2 up to 10 wt%. The samples were produced via pressing and sintering. It can be said, that with up to 4 wt% ZrO_2 the mechanical properties could be improved. XRD measurements of the Ti-4 wt% ZrO_2 sample showed the presence of ZrO_2, which indicates that no reaction between Ti and ZrO_2 took place even at a sintering temperature of 1100 °C, contrary to Kondoh et al. [23]. Nevertheless a dispersion of Zr in the form of ZrO_2 in grains and grain boundaries can be noted.

2.3.3 Hydrogen

With the addition of Zr in the form ZrH_2 or ZrO_2 the effects of hydrogen and oxygen regarding its influence on mechanical properties of Ti alloys are to be discussed in the next two chapters.

Hydrogen, as shown in Figure 1, is a β eutectoid stabilizer. The with FactSage calculated phase diagram of Ti - H is depicted in Figure 5. Hydrogen decreases the α/β transus temperature from 882 °C to an eutectoid temperature of 300 °C. The eutectoid transformation results in α-Ti and hydride phases such as fcc δ-TiH_x (x = 1.5 - 2.0 [26]). The solubility of hydrogen in α-Ti is up to 7 at% at 300 °C followed by steep decrease [27]. At room temperature the hydrogen solubility in α-Ti is approximately 0.02 wt% [7] and is limited to 125 to 150 ppm due to risk of hydrogen embrittlement [6]. H occupies the tetrahedral interstitial sites resulting in a lattice expansion [26].

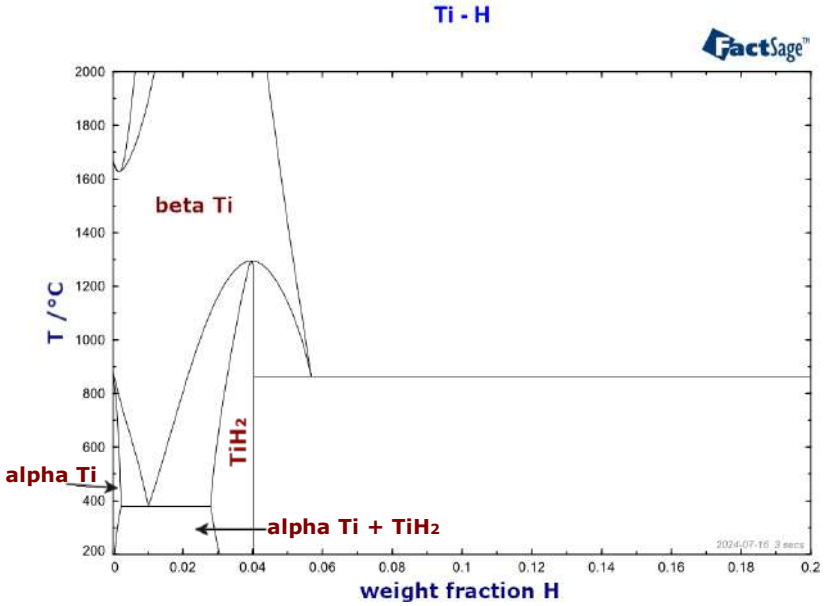

Figure 5: Calculated phase diagram for Ti-H (FactSage)

The addition of hydrogen can lead to embrittlement and reduction of the threshold for crack propagation. The embrittlement can be caused by precipitation or the decomposition of hydride phases, which become brittle at room temperature [28]. A controlled introduction of hydrogen in the material can lead to improvement in its production and processing. Thermohydrogen processing (THP) uses hydrogen as a temporary alloying element, which will be removed at the end during an annealing. With the addition of hydrogen, hot workability and superplastic forming improve. Furthermore, THP leads to grain refinement and improved mechanical properties [29, 30].

With sufficiently high hydrogen concentration, titanium powders can be produced via the HDH (hydride–dehydride) process, which utilizes the room temperature embrittlement [29, 31].

2.3.4 Oxygen

Mechanical properties of commercially pure (CP) Ti and Ti alloys depend strongly on interstitial element such as oxygen. The addition can happen voluntarily (i.e. ZrO_2) or as impurities during the production process due to the high affinity of Ti for O. As previously mentioned, oxygen is a α stabilizer (Figure 1). Figure 6 depicts the with FactSage calculated phase diagram of Ti - O. In this calculation oxygen is soluble in α-Ti up to 14 wt%, which is consistent with literature value of 12 wt% [32]. Oxygen occupies as a interstitial element the octahedral interstitial sites of Ti, resulting in an increase of the lattice parameter c and the c/a ratio [12]. Oxygen, as well as N, C and Fe, can increase strength of CP Ti due to solid solution strengthening [33].

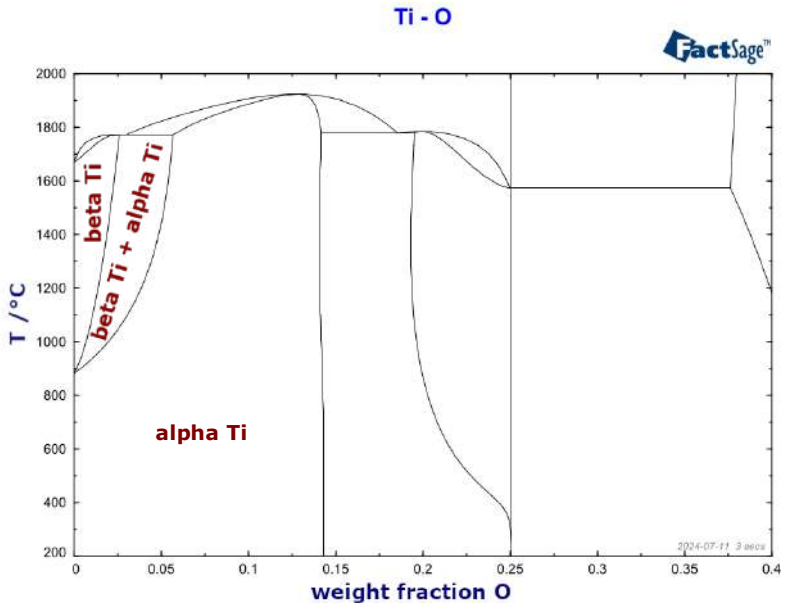

Figure 6: Ti-O phase diagram up to an oxygen weight fraction of 40 % (FactSage)

Oh et al. [34] investigated the effect of oxygen as an interstitial element on CP Ti and Ti6Al4V. Oxygen was added up to 0.351 and 0.336 wt%, respectively. An increase in hardness and tensile strength could be observed in both sample series, whereas Ti6Al4V was influenced less strongly by the oxygen addition. Ductility decreases with increasing oxygen concentration. Again, the oxygen addition shows a greater effect on CP Ti than on Ti6Al4V, which could be explained by the lattice expansion due to Al and V during the alloying process.

2.4 Deformation

Due to its hcp crystal structure, α-Titanium has limited deformation capability, rendering the phase less ductile compared to the bcc β-titanium. Therefore, α and $\alpha + \beta$ alloys can only be deformed at elevated temperatures. As the β phase content increases, the deformation temperature decreases, allowing for the deformation of some metastable β alloys even at room temperature without edge cracking [1, 8].

Deformation at elevated temperatures and strain rates, referred to as hot working, is a possibility to break down and refine coarser prior β grains. The resulting microstructure, thus the mechanical properties, are influenced by many factors as the used strain rate and temperature as well as the composition and initial microstructure of the alloy. For example, hot working in the $\alpha + \beta$ region can achieve the formation of The deformation below the α/β transus temperature prevents the coarsening of prior β grains. The primary α particles elongate during hot working and break up due to dynamic recrystallisation [7].

$\alpha + \beta$-titanium alloys are typically deformed during hot working in the $\alpha + \beta$ region, typically 30 to 55 °C below the α/β transus temperature. Hot working in this region ensures a microstructure with better mechanical properties like ductility and low cycle fatigue compared to β rolling, meaning hot working 30 to 55 °C above α/β transus temperature. β rolling can improve creep and fracture toughness properties [7]. Hot working in the $\alpha + \beta$ region results in deformed or equiaxed primary α in the transformed β matrix [35]. It is important to prevent a reducing environment and thus hydrogen uptake. Additionally, the preheating time should be sufficient to heat up the whole sample, but not excessively long to prevent unnecessary oxidation and primary α grain growth [7].

Other mechanisms for refinement of β grains, which can occur during hot working, are dynamic recovery (DRV) and dynamic recrystallization (DRX) [36]. The microstructure of α and near α-Ti alloys after deformation is significantly influenced by the temperature. The microstructure is determined by DRV, when processed below the α/β transus temperature. Processing above α/β transus temperature is controlled by DRX, resulting in deformed grains containing highly developed subgrains [37]. A similar trend can also be observed in the deformation of Ti6Al4V [38].

Under rapid cooling rate, β-titanium can transform in different α phases, so called martensite. This formation can be differentiated into hexagonal $\alpha^{'}$ and orthorhombic $\alpha^{''}$. Both types of martensite exhibit an increase in hardness but also in embrittlement and are therefore not desirable [39]. The orientation of $\alpha^{'}$ and α to the β phase is similar. Hence, the microstructure of the martensite also forms needle-like laths in a basket-weave structure because of the diffusionless nucleation process [1, 8].

To determine the martensitic start temperature M_s, Mo equivalent ($Mo_{eq.}$) can be calculated (Equation 1). The equations represents the stability of the β phase, determined by the sum of the weighted averages of the alloying elements in wt% in contrast to the most effective β stabilizer molybdenum. α stabilizers increase the martensitic start temperature, whereas β stabilizers cause a decrease in M_s [6]. There are different equations, which differ in the coefficient of some alloying elements as well as the elements taken into account. The modified $Mo^{B}_{eq.}$ equation proposed

by Bania [40] is the most commonly utilized. It takes also aluminium into account as a stabilizer of the α phase. The equation $Mo_{eq.}^{W}$ [41] takes more alloying elements into account, ie. Zr. In this thesis the equation $Mo_{eq.}^{W}$ will be preferred because the influence of zirconium is considered [42].

$$\begin{aligned} Mo_{eq.}^{B} &= 1.00Mo + 0.22Ta + 0.28Nb + 0.44W + 0.67V + 1.6Cr + 1.11Ni \\ &\quad + 2.9Fe + 0.77Cu + 1.43Co + 1.54Mn1.0Al(\%wt) \\ Mo_{eq.}^{W} &= 1.00Mo + 0.22Ta + 0.28Nb + 0.59W + 1.25V + 1.84Cr + 2.46Ni \\ &\quad + 1.93Fe + 1.51Cu + 2.67Co + 2.26Mn + 0.3Sn + 0.47Zr + 3.01Si \\ &\quad - 1.47Al(\%wt) \end{aligned} \tag{1}$$

2.5 Aim of this work

The production of titanium via WAAM presents difficulties such as columnar grain growth or the production of the wire itself. A promising possibility to inhibit the formation of columnar grain growth is the addition of copper due to its eutectoid formation of α-Ti and Ti_2Cu. To produce wires for the WAAM process ductility of the alloy has to be given. Zr is a promising alloying element as it enhances the ductility of the alloy as well as mechanical strength due to grain refinement.

The goal of this master thesis is to investigate the influence of zirconium on the microstructure and mechanical properties of titanium and Ti-Cu systems. Different Zr sources (pure Zr, ZrH_2, and ZrO_2) were examined concerning their impact on microstructure and mechanical properties. Due to the use of ZrO_2, the influence of oxygen also had to be taken into account. In addition to various Zr sources, the samples were produced using different fabrication processes, such as arc melting, sintering and hot extrusion. The production methods were compared regarding microstructure and mechanical properties.

The second objective focuses on the deformation behaviour analysis of the fabricated Ti-Zr alloy systems, as well as Ti5.9Cu2Al2Fe, a promising alloy system provided by GfE. Hot extrusion test of the Ti5.9Cu2Al2Fe alloy were carried out resulting in different rod diameters. The wire production was simulated by rolling Ti5.9Cu2Al2Fe at two different temperatures, one above and one below the α/β transus temperature. The deformation behaviour of this material was examined and compared. Furthermore, the deformation behaviour of the self-fabricated Ti-Zr systems will be investigated using a deformation dilatometer under varying deformation speeds and temperatures.

3 Experimental and Material

3.1 Powders and materials

For the preparation of the extruded and sintered samples, elemental powders were used, shown in Figure 7. Metal pellets and flakes were used for samples produced in the arc furnace. Characteristics of these materials are summarized in Table 1.

Table 1: Characteristics of powders and materials

powder	purity	particle size	manufacturer
Ti	99%	<45 µm	Eckart TLS GmbH
ZrH_2	99%	4.5 - 6.5 µm	Thermo Scientific Chemicals
ZrO_2	-	-	Z-Tech
pellet	purity		manufacturer
Ti	99.9%		Onyxmet
Zr	99.9%		Onyxmet
Cu	-		Buntmetall Amstetten GmbH

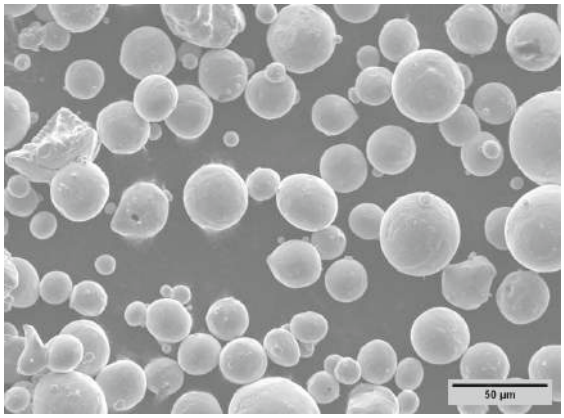

(a) Ti

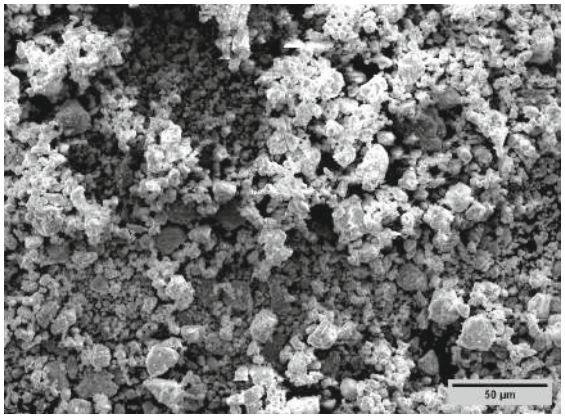

(b) ZrH_2

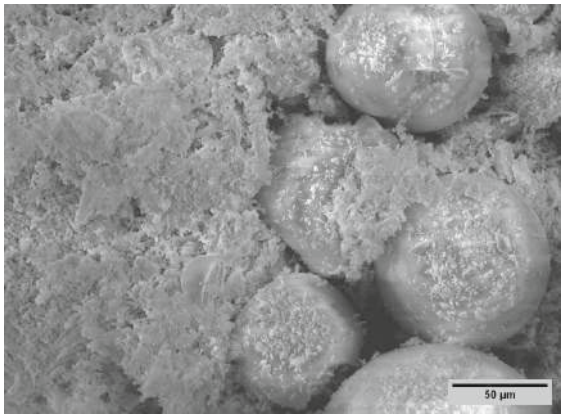

(c) ZrO_2

Figure 7: SEM-ETD images of powders utilized in the production of samples through hot extrusion and sintering

3.2 Arc furnace

To produce small quantities of samples the arc furnace was used (Compact Arc Melter MAM-1, Edmund Bühler GmbH). The metal pellets of Ti, Cu and pure Zr were placed in the desired composition inside an evacuation chamber featuring a cooled copper plate. The composition of the samples is summarized in Table 2. Prior to commencing the melting process under argon, the chamber was evacuated and aerated three times. To ensure sufficient homogenization of the samples, they were remelted three times in the arc furnace, with the sample being flipped each time. The resulting button melts were cut in half for the sample preparation. Afterwards, the sample series Ti6.5CuxZr was heat treated at 1000 °C for 30 h in an argon atmosphere to ensure a homogeneous microstructure.

Table 2: Composition of the samples produced in the arc furnace

	x (wt%)
TixZr	5, 10, 15
Ti6.5CuxZr	3, 5, 8, 10, 12, 15

3.3 Pressing and Sintering

The sample series Ti-ZrH_2 utilized the powders depicted in Figure 7. The samples were pressed and subsequently sintered in vacuum to ensure the secure manipulation of ZrH_2. The first samples with 3, 5 and 10 wt% ZrH_2 were prepared by mixing the powders in Turbular for 1 h. For the next experiments with the same ZrH_2 content, the sample mixtures were milled for 17 hours on a rolling mill at 158 rpm with a ratio of 1:10 hardmetal balls.

All samples were pressed using the Alfred J. Amsler & Co. Schaffhausen with a pressing pressure of 5 $t\,cm^{-2}$. If it was not possible to press the powder mixtures successfully, the loose powder fillings underwent sintering in an alumina crucible instead. The samples were sintered up to 1100 °C under vacuum. The detailed temperature profile of the sintering is depicted in Figure 8. The samples were furnace cooled. Afterward the samples were heat treated at 1000 °C for 1 h under argon atmosphere and water quenched.

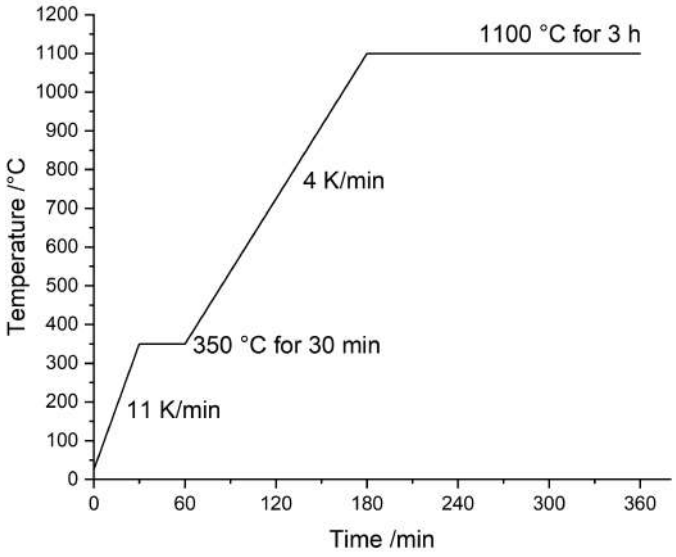

Figure 8: Temperature profile used for vacuum sintering. Afterwards samples were furnace cooled.

3.4 Hot Extrusion

The direct hot extrusion process was performed on the extrusion press V. Jessernigg and Urban. The production of samples could be achieved through either a powder metallurgical approach or directly from a casting material.

The samples $TixZrO_2$ (x = 0.5, 1, 2, wt%) were prepared using the first method. The desired composition of powders was mixed with hardmetal grinding balls in a Turbular mixer for 1 h. Afterwards the mixture was transferred in a steel cylinder (ST35) with dimensions of 60 mm height, 40 mm outer diameter, and 36 mm inner diameter. The cylinder was sealed with caps made of the same material, which were welded to the ends. To ensure lubrication during the extrusion process, the cylinders were coated with boron nitride. The samples were preheated at 1000 °C for 20 min, while the press was preheated at 350 °C. The extrusion ratio employed was 1:11.1 resulting in a rod of 12 mm. The extrusion speed was set to 10 $mm\,s^{-1}$. Exemplary, the obtained rod of sample $Ti1ZrO_2$ is shown in Figure 9. The steel casing of the rods was machined off, resulting in rods with a a diameter of 10 mm. The samples were heat treated at 1000 °C for 24 h under argon atmosphere. To analyse, the samples were taken from the marked sections (rear, middle, front)

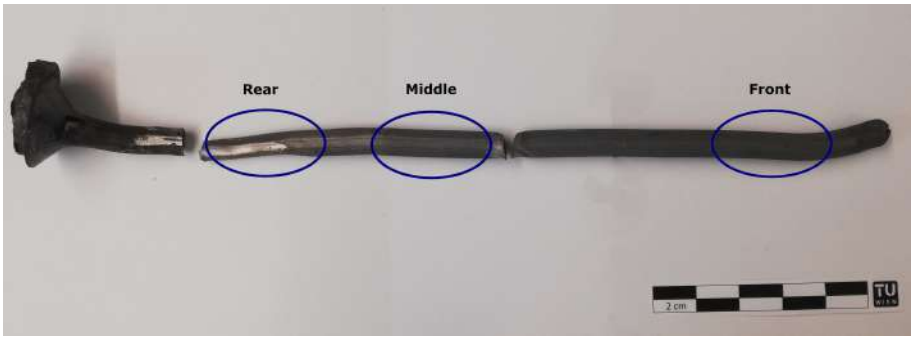

Figure 9: Rod of Ti1ZrO_2, obtained from hot extrusion. Samples were taken from the marked sections (rear, middle, front).

Ti5.9Cu2Fe2Al was produced through gravity melting by the external manufacturer GfE. The nominal and actual composition, which was analyzed by GfE, of the cast material is summarized in Table 3. Despite the slight difference in composition, the cast material and the obtained samples are referred to as Ti5.9Cu2Fe2Al. Two hot extrusion runs were conducted, resulting in two different rod diameters (4 and 8 mm). Prior to hot extrusion, the material was coated with boron nitride and preheated at 1100 °C for the 8 mm rod or 1200 °C for the 4 mm rod each for 30 min. The temperature of the press and extrusion speed remained consistent with the conditions of the previous experiment with the sample series TixZrO_2. The extrusion ratio of 1:33.3 was utilized, resulting in the formation of a 8 mm rod. Furthermore, the extrusion ratio of 1:25 was used to obtain three 4 mm rods. The heat treatment for the 8 mm rod was conducted at 1000 °C for 24 h under argon atmosphere, identical to the parameters used for the TixZrO_2 samples.

Table 3: Nominal and actual composition of the cast material Ti5.9Cu2Fe2Al produced by GfE

	Composition (wt%)			
	nominal	actual		actual
Ti	90.1	89.0	Si	0.001
Cu	5.9	6.2	C	0.006
Fe	2.0	2.2	H	0.001
Al	2.0	2.1	N	0.005
			O	0.03

Samples were taken from three different sections (rear, middle, front) of the rod to analyse the homogeneity of the rod. The sections are marked in Figure 9. To determine the influence of the deformation on the microstructure, the extruded samples were cut in the extrusion direction and also perpendicular to it.

3.5 Caliber rolling

Caliber rolling of the cast material Ti5.9Cu2Fe2Al was employed to simulate the wire drawing process. The caliber roll Friedrich Krupp - Grusonwerk AG Magdeburg-

Bruckau was used. The casting material Ti5.9Cu2Fe2Al was initially cut into a rectangular shape with a cross-section of 7.5 by 7.5 mm. Table 4 summarizes the crosssections and the degree of deformation for the ten calibers. The degree of deformation φ was calculated using equation 2 [43].

$$\varphi = ln\frac{A_0}{A} \tag{2}$$

φ ..... degree of deformation (-)
A_0 ..... sample crosssection before rolling (mm^2)
A ..... sample crosssection after rolling (mm^2)

Before passing through the first caliber, the material was preheated under argon gas at 800 °C or 1000 °C for 15 minutes. After the first rolling, the material was heated again for 5 minutes before proceeding to the second caliber, for which the sample was rotated by 90°. Subsequently, the material was cut perpendicular and longitudinal to the rolling direction. This entire process was repeated through all ten calibers, with samples taken at every second caliber.

Table 4: Crosssections and degree of deformation of caliber rolling

	crosssection (mm^2)	φ
Starting material	7.5 x 7.5	
1. caliber	8 x 8	-
2. caliber	7.2 x 7.2	0.08
3. caliber	6.5 x 6.5	0.29
4. caliber	6 x 6	0.45
5. caliber	5.6 x 5.6	0.58
6. caliber	5.2 x 5.2	0.73
7. caliber	4.8 x 4.9	0.87
8. caliber	4.4 x 4.5	1.04
9. caliber	4 x 4	1.26
10. caliber	3.7 x 3.7	1.41

3.6 DIL

For the deformation measurements the cylindrical samples were required to have a diameter of 5 mm and a length of 10 mm. Therefore, these samples were manufactured using the arc furnace with slight modifications. The button melts were produced as described in Section 3.2. After the button melts were produced, a different cooled copper plate was installed. This plate featured a central hole designed for a cylindrical mold with the desired 5 mm diameter opening. Following the melting process, a vacuum was drawn through this opening, created within a vacuum chamber. The melt was pulled into the cylindrical mold, resulting in a cylindrical sample. In Figure 10, an example of a sample inside the cylindrical mold is depicted. Afterwards, the sample was cut to the required length of 10 mm.

Figure 10: Sample for dilatometry measurements in cylindrical mold after melting in arc furnace

The deformation properties were measured using the DIL 805A/D Quenching and Deformation Dilatometer - TA Instruments. To ensure uniform force distribution, the sides of the cylindrical sample were coated in graphite and small discs were installed. The sample was secured between the Si_3N_4 stamps. Thermocouples were welded to the sample. Figure 11 shows the interior of the dilatometer with an installed sample. After evacuation, the goal temperature of 700 and 900 °C, which was achieved in 2 min, was maintained for 3 min. Subsequently, the deformation took place at a strain rate of 0.01 and 10 s^{-1}. The sample was rapidly cooled with helium.

Figure 11: DIL 805A/D Quenching and Deformation Dilatometer with an installed sample

3.7 Sample Preparation

All samples were cut using the Accutom-5 cutting machine (Struers GmbH) with a diamond-embedded cutting wheel. The best results were obtained at a speed of 3000 rpm and a feed rate of 10 $m\,s^{-1}$. Subsequently, the samples were embedded in Bakelite (DuroFast, Struers GmbH). This embedding process was carried out using the CitoPress-1 (Struers GmbH) at 180 °C and 250 bar for 6 minutes.

The embedded samples were then grinded and polished using Tegramin-30 and Tegra-Pol 30 (Struers GmbH). To grind the samples, SiC-Paper with a grain size of P500, P1200 and P4000 was used. Afterwards, the samples were polished for 15 min with a MD/DP-Nap cloth. A mixture of OPS NonDry (0.25 µm SiO_2 suspension, diluted 1:1 with water) and H_2O_2 22% in a ratio 2:1 was used. After each step, the samples were cleaned with water and then subjected to ultrasonic cleaning in isopropanol for approximately 5 minutes.

To visualize the microstructure, all samples were etched with 1 % HF for a few seconds. When foaming began, the sample was rinsed with water.

3.8 SEM

The microstructure of the samples was examined using the FEI Quanta 200 scanning electron microscope (Thermo Fisher Scientific Inc.). The scanning electron microscope was operated in high-vacuum mode with a cathode acceleration voltage of 20 kV.

The sample composition was determined using an energy-dispersive X-ray spectroscopy detector (EDAX Octane Pro, Ametek Inc.).

3.9 X-ray diffractometry

To characterize the resulting phases, the samples were measured using an XPERT II: PANalytical XPert Pro MPD (Theta-Theta diffractometer) equipped with a copper anode. The measurement was carried out the $2°\theta$ range of 10 to 110 degrees with a step size of 0.02 degrees, and each step was measured for 80 seconds.

An analyse of the lattice parameters a and c as well as the c/a ratio of the hexagonal lattice structure of α-Ti was conducted using the Rietveld refinement.

3.10 Hardness

Hardness of all samples was determined using the Vickers method with a load of 10 kg, whereby five indents were made. The extruded samples were measured in the perpendicular and extrusion directions. The machine EMCO-Test M4U-025 was used and the indents were evaluated with an optical microscope. Equation 3 was used to calculate the hardness.

$$HV = 0.1891 \cdot \frac{F}{d^2} \tag{3}$$

HV ..... Vickers Hardness (-)
F ..... Indention force (N)
d ..... Average of the diagonal lengths (mm)

3.11 Density

The Archimedes density was determined for all samples using the scale Mettler Toledo XS204. Since the entire sample of button melts was generally weighed, only a single weighing was performed. Therefore, the standard deviation of the scale is assumed to be 0.1 mg and is not explicitly stated for the individual measurements. Equation 4 was used to calculate the density using the measured mass of the samples in both air and water.

$$\rho = \frac{m_{air} \cdot \rho_{water}}{m_{air} - m_{water}} \tag{4}$$

ρ ..... Density of measured sample (g cm^{-3})
m_{air} ..... Mass of sample in air (g)
ρ_{water} ..... Density of water (g cm^{-3})
m_{water} ..... Mass of sample in water (g)

3.12 Overview of produced samples

Table 5 provides an overview of the production methods for the Ti-Zr samples, including the applied heat treatments. To ensure a good comparison of the produced Ti-Zr alloys in the discussion, the nominal Zr concentrations for the TixZrH$_2$ and TixZrO$_2$ sample series were calculated, and the corresponding values are indicated in parentheses in the table.

Additionally, the deformation parameters of the hot extruded or caliber rolled Ti5.9Cu2Al2Fe samples are given.

Table 5: Overview of the produced samples, including the production methods and heat treatment parameters.

Sample name	Composition (wt%)					Preheating	Production method	Heat treatment
	Cu	Zr (nominal)	ZrH$_2$	ZrO$_2$	Ti			
TixZr		5, 10 , 15			bal		arc melting	1000 °C/ 30 h at Ar
Ti6.5CuxZr	6.5	3, 5, 8, 10, 12, 15			bal		arc melting	1000 °C/ 30 h at Ar
TixZrH$_2$		(2.94, 4.89, 9.79)	3, 5, 10		bal		vacuum sintering at 1100 °C/ 3 h	1000 °C/ 1 h at Ar water quenched
TixZrO$_2$		(0.37, 0.74, 1.48)		0.5, 1, 2	bal	1000 °C/ 20 min	hot extrusion	1000 °C/ 24 h at Ar
	Cu	Al	Fe		Ti			
Ti5.9Cu2Al2Fe	5.9	2	2		bal		gravity melting by GfE	
Ti5.9Cu2Al2Fe_4mm	5.9	2	2		bal	1200 °C/ 30 min	hot extrusion	
Ti5.9Cu2Al2Fe_8mm	5.9	2	2		bal	1100 °C/ 30 min	hot extrusion	1000 °C/ 24 h at Ar
Ti5.9Cu2Al2Fe_800 °C	5.9	2	2		bal	800 °C/ 15 min	caliber rolling	
Ti5.9Cu2Al2Fe_1000 °C	5.9	2	2		bal	1000 °C/ 15 min	caliber rolling	

4 Results and Discussion

4.1 Arc Furnace - TixZr and Ti6.5CuxZr

Samples with the addition of 5, 10 and 15 wt% Zr, produced using the arc furnace, are depicted in Figure 14. The manufacturing of the samples using this method produced optically dense samples. The density of the samples, summarized in Table 6, is over 99.5 % of the theoretical density. This shows that the method can produce suitable samples for further investigations.

Table 6: Density of as-cast TixZr samples; standard deviation of balance assumed to be 0.1 mg due to single weighing of entire sample.

	as-extruded	
sample	density g/cm^3	% theoretical density
Ti5Zr	4.551	99.57
Ti10Zr	4.631	99.75
Ti15Zr	4.716	99.95

The acicular microstructure becomes more refined with increasing Zr content, as observed in Figure 14a, c and e. The observation of primary α-laths and β-phase microstructure in SEM is confirmed by XRD measurements, as only these two phases could be detected (Figure 12). The XRD measurements also show a leftward shift in the α-titanium peaks with increasing Zr concentration. Since zirconium is completely soluble in Ti (as seen in Figure 4), it is incorporated substitutionally into the Ti lattice. For reference, pure α-Ti exhibits a lattice parameter of a = 2.95 Å and c = 4.68 Å , the c/a ratio is 1.587 [6, 7], as mentioned in Chapter 2.1. The lattice parameter a and c as well as the c/a ratio are summarized in Figure 13, as a function of the Zr content. The lattice parameters a and c increase due to the larger radius of Zr than that of Ti. However, the c/a ratio of 1.58 remained nearly constant at approximately the value of pure Ti, regardless of the Zr content. These results are comparable to the literature [44–46].

EDX point analysis shows that during the production of the samples using the arc furnace, the zirconium dissolved homogeneously in the sample. Therefore, further samples with different compositions can be produced using this method.

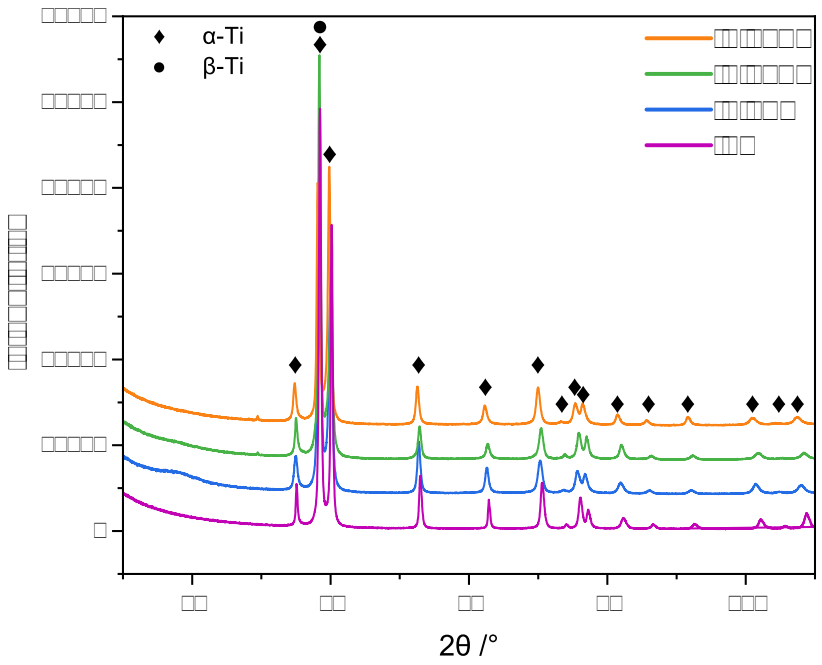

Figure 12: XRD measurements of the sample series TixZr (x = 5, 10, 15 wt%) and pure titanium as reference.

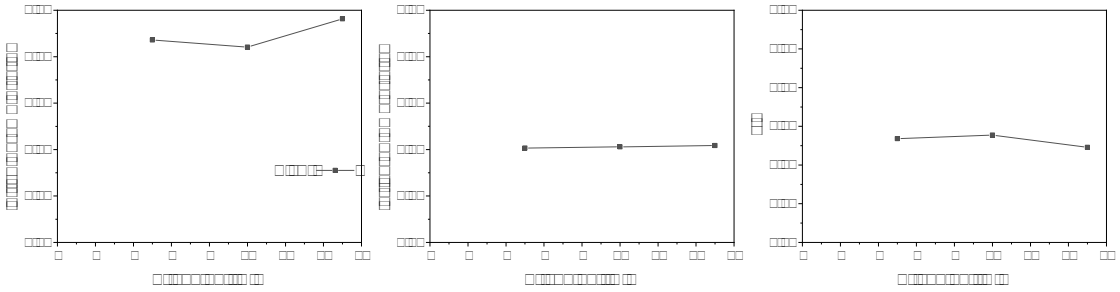

Figure 13: Lattice parameter a and c and the c/a ratio of the TixZr sample series depending on Zr content.

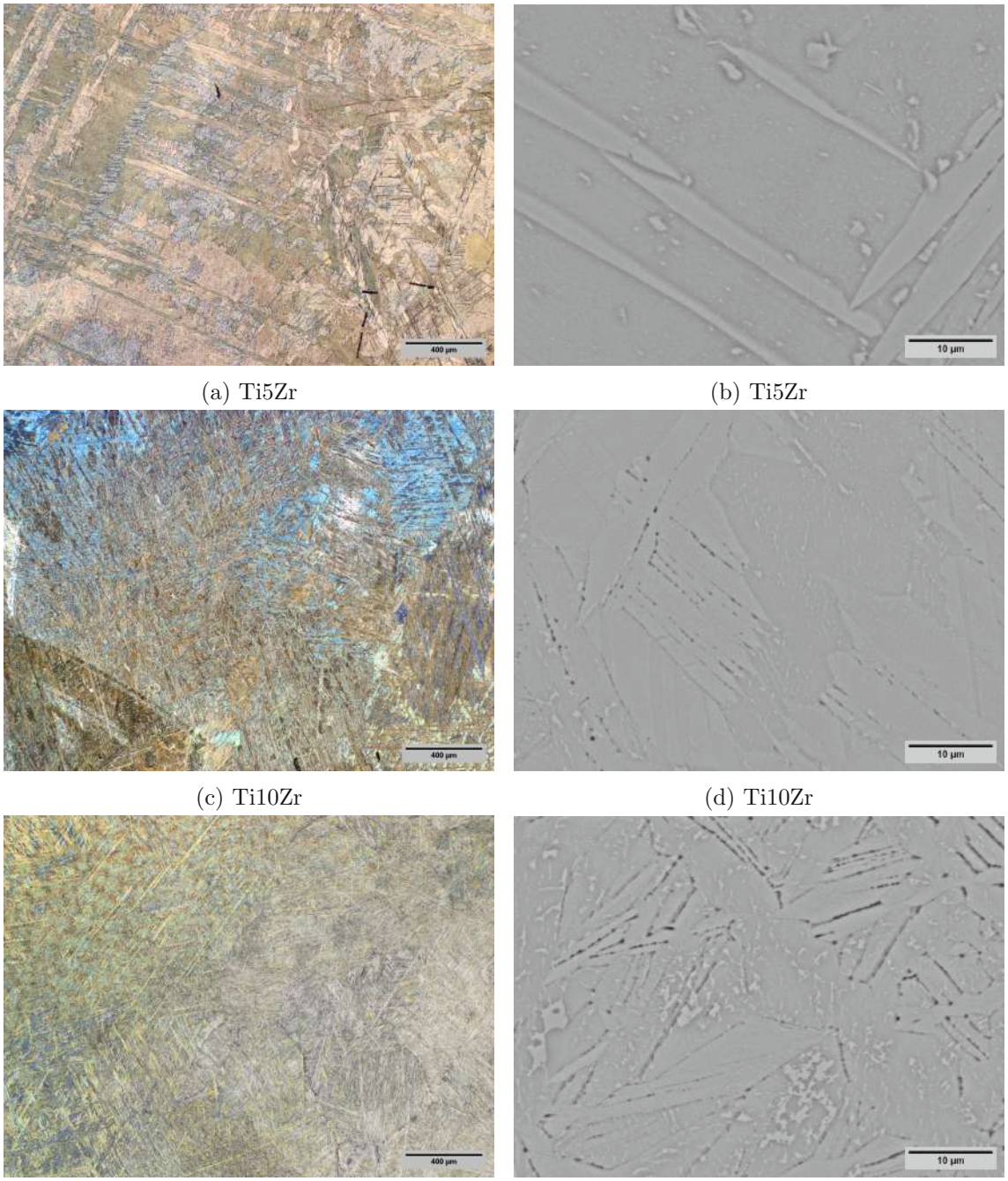

(a) Ti5Zr (b) Ti5Zr

(c) Ti10Zr (d) Ti10Zr

(e) Ti15Zr (f) Ti15Zr

Figure 14: LOM and SEM images of the samples series TixZr (x = 5, 10, 15 wt%) in the as-cast state.

Figure 15a shows the calculated phase diagram of Ti6.5CuxZr (FactSage) with a focus on Zr content up to 15 wt%. Alloys with a Zr content up to 10 wt% form as expected α-Ti and Ti_2Cu. The addition of 6.5 wt% copper leads to the formation of eutectoid in the form of α-Ti + Ti_2Cu (see Figure 3). The addition Zr above 15 wt% may lead to the formation of $CuZr_2$ according to the calculation. However, the $CuZr_2$ phase only forms at temperatures under 300 °C (Figure 15b). Because of the rapid cooling rate in the arc furnace, this phase is not to be expected. With increasing zirconium content the β transus temperature decreases from approximately 800 °C for Ti6.5Cu3Zr to 750 °C for Ti6.5Cu15Zr. Despite the qualification as a neutral element, zirconium decreases the α/β transus temperature slightly [6].

In Table 7 the density of the as-cast and heat-treated (1000 °C for 30 h) Ti6.5CuxZr samples are summarized. It is evident that, except for the as-cast Ti6.5Cu12Zr sample, a density exceeding 99.5 % of the theoretical density can be achieved, similar to the TixZr sample series (Table 6). The density appears to slightly decrease after heat treatment, however the reduction is not statistically significant.

Table 7: Density of Ti6.5CuxZr samples in the as-cast and heat-treated state; standard deviation of balance assumed to be 0.1 mg due to single weighing of entire sample.

	as-cast		heat-treated	
sample	density g/cm^3	% theoretical density	density g/cm^3	% theoretical density
Ti6.5Cu3Zr	4.698	100.05	4.703	100.17
Ti6.5Cu5Zr	4.743	100.37	4.721	99.91
Ti6.5Cu8Zr	4.789	100.35	4.778	100.13
Ti6.5Cu10Zr	4.801	99.95	4.779	99.50
Ti6.5Cu12Zr	4.816	99.60	4.761	98.48
Ti6.5Cu15Zr	4.882	99.97	4.862	99.56

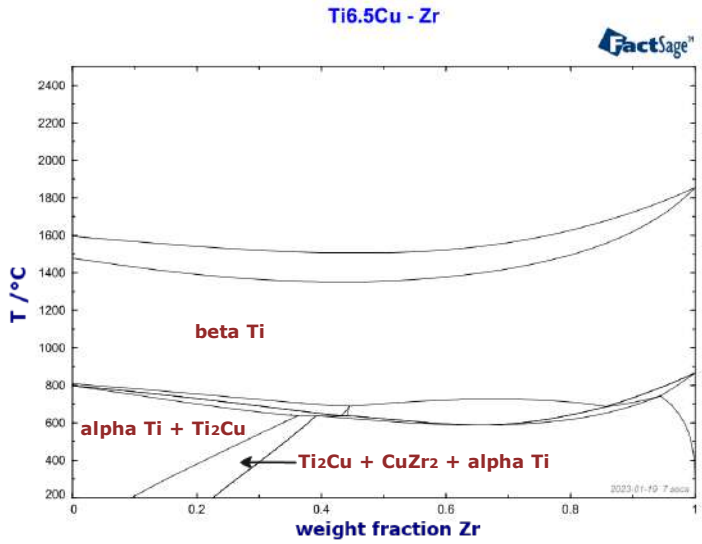

(a) Phase diagram of Ti6.5Cu - Zr

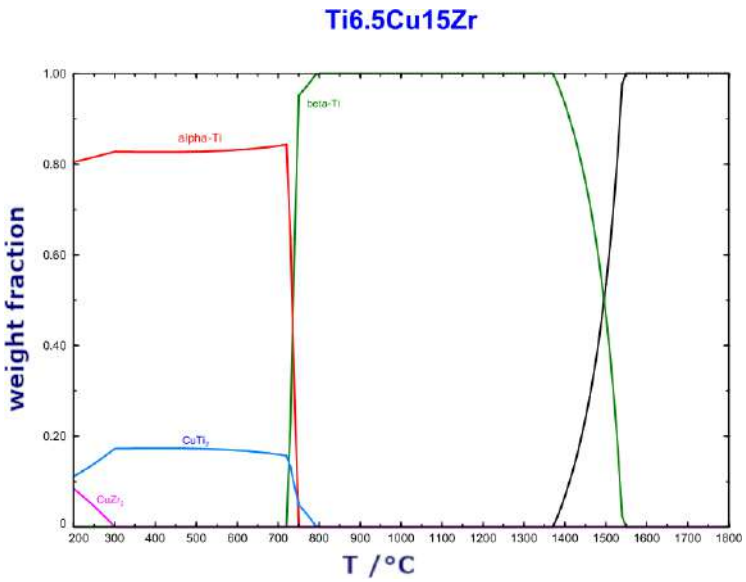

(b) Equilibrium phase diagram of Ti6.5Cu15Zr

Figure 15: Phase diagrams of Ti6.5Cu - Zr (a) and the equilibrium phase diagram of Ti6.5Cu15Zr (b).

The addition of 6.5 wt% results in a coarse microstructure in sample Ti6.5Cu3Zr (Figure 16a), which vanishes almost completely with a Zr content above 5 wt% (Figure 16b - f). There are still coarse interim areas visible wherein they become finer with increasing zirconium content. To analyse the coarse phase, the samples were examined using microhardness and EDX analysis. The microhardness HV0.1 for the coarse phase is 313 ± 11, while the HV0.1 for the α/β microstructure is 292 ± 13. The observed difference in hardness, with a large standard deviation, is not significant. EDX point analysis were conducted on several samples, exemplary the results of the sample Ti6.5Cu12Zr (Figure 17e) are shown. In all samples a higher copper content was detected in the interim areas. Point 1, in the interim area, has a copper content of 8.9 wt%, whereas the content decreases to the desired content of 6.5 wt% at point 2 in α/β microstructure. Therefore, it is suspected that the interim areas are retained β phase. With increasing zirconium content a refinement in the microstructure is observed, which is consistent with the literature [17].

Because of the rapid cooling in the arc furnace the eutectoid microstructure is only slightly visible in sample Ti6.5Cu3Zr, as seen in Figure 17a. With increasing Zr content a triangular structure of needle-like laths were be observed (Figure 17b - f). This indicates that Zr inhibits the eutectoid transformation.

The observed needle-like laths could be identified as very fine α/β microstructure or martensite. The calculated M_s temperature, using the $Mo_{eq.}^{W}$ equation, as discussed in Section 4.5, ranges from 862 °C for Ti6.5Cu3Zr to 778 °C for Ti6.5Cu15Zr. The exceeding temperature in the arc furnace and the rapid cooling would promote the forming of martensite. To confirm this, further investigations in TEM would be necessary.

The heat treatment at 1000 °C for 30 h resulted in a significant coarsening of the microstructure, especially in samples with 3 and 5 wt% Zr (Figure 18a, b). Simultaneously, the presence of interim regions is substantially diminished with higher zirconium content. In samples with a Zr content of 8 to 12 wt% no coarse interim regions could be found (Figure 18c - e). In Figure 18f residual interim region in sample Ti6.5Cu15Zr are shown, however these are coarser and no longer as numerous as before the heat treatment. Furthermore, a Widmanstätten structure can be observed, which is enhanced by the slow cooling.

The heat treatment also resulted in the formation of an eutectoid which can be observed throughout the sample series (Figures 19). The formation of the eutectoid is enhanced due to the slow furnace cooling.

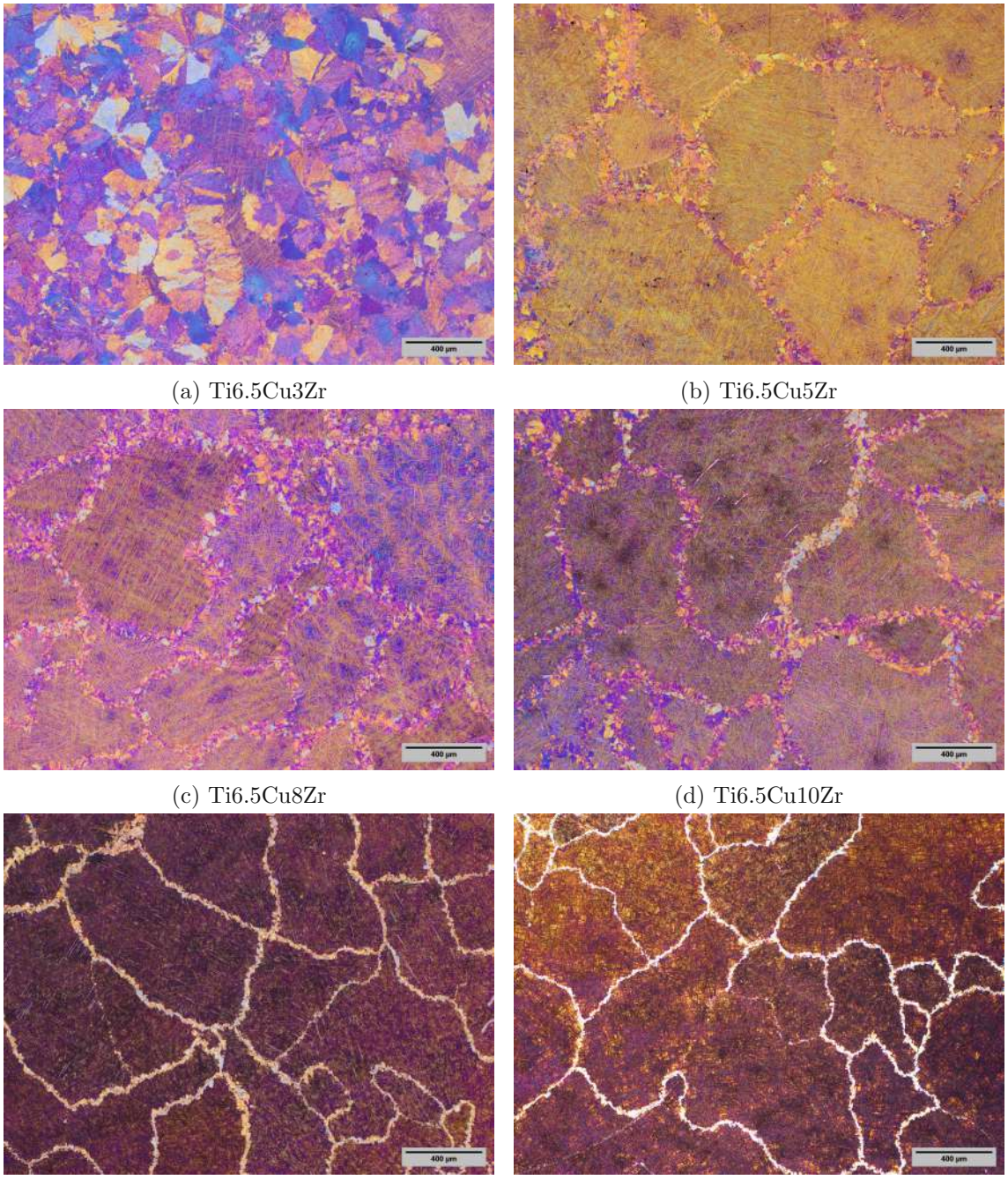

(a) Ti6.5Cu3Zr (b) Ti6.5Cu5Zr

(c) Ti6.5Cu8Zr (d) Ti6.5Cu10Zr

(e) Ti6.5Cu12Zr (f) Ti6.5Cu15Zr

Figure 16: LOM images of the as-cast sample series Ti6.5CuxZr (x = 3, 5, 8, 10, 12, 15 wt%)

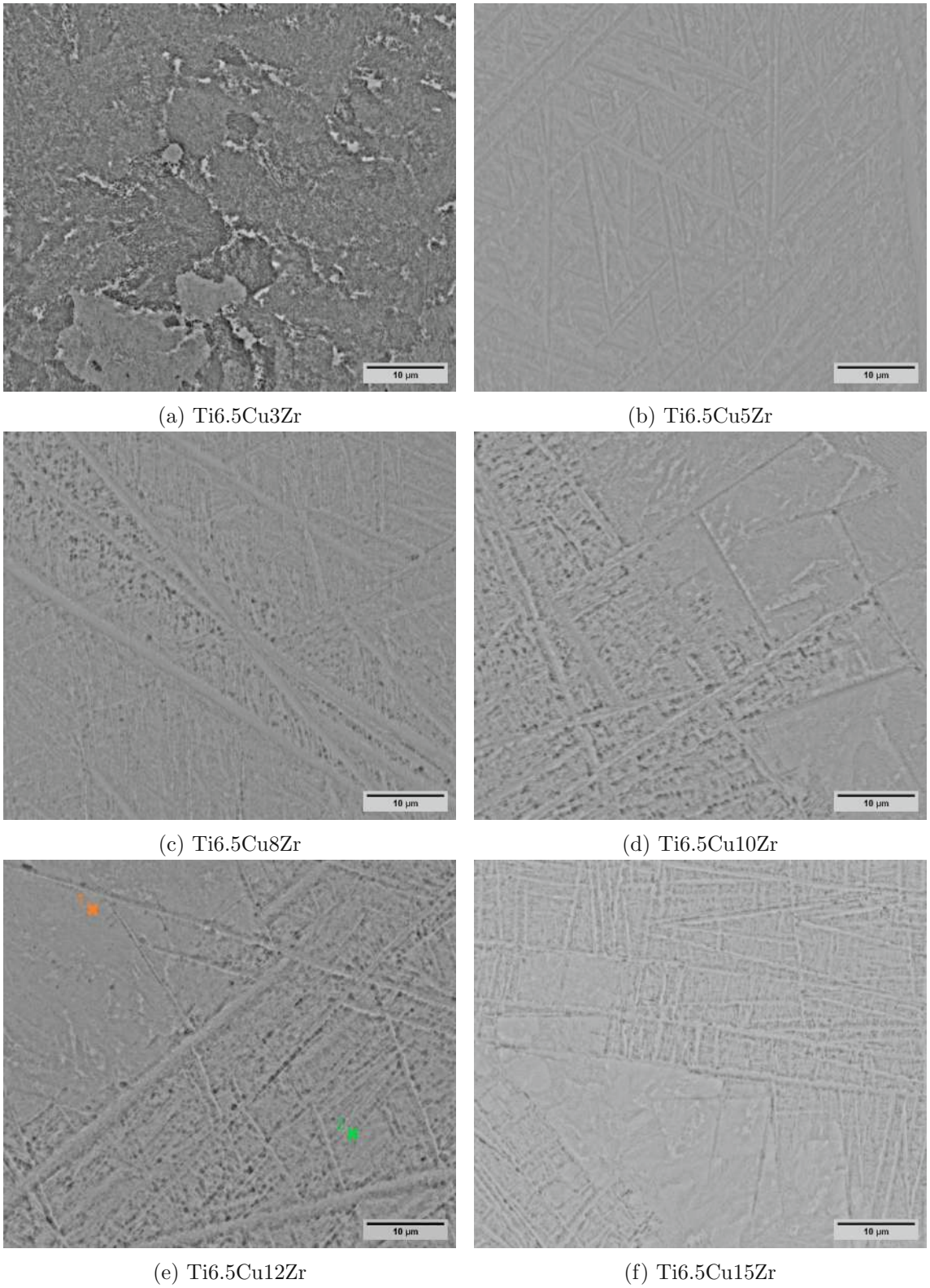

(a) Ti6.5Cu3Zr (b) Ti6.5Cu5Zr

(c) Ti6.5Cu8Zr (d) Ti6.5Cu10Zr

(e) Ti6.5Cu12Zr (f) Ti6.5Cu15Zr

Figure 17: SEM images of the as-cast sample series Ti6.5CuxZr (x = 3, 5, 8, 10, 12, 15 wt%). The measured points via EDX point analysis are marked in Figure e.

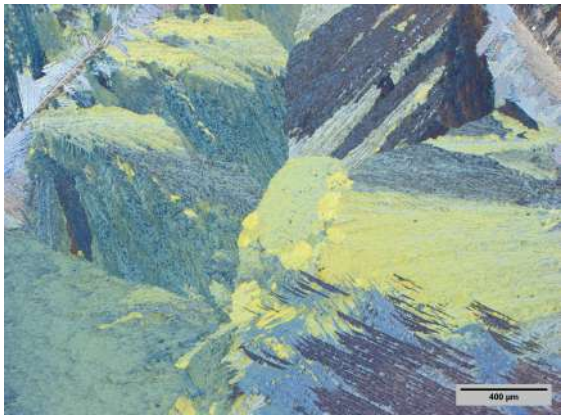

(a) Ti6.5Cu3Zr 1000 °C/30 h

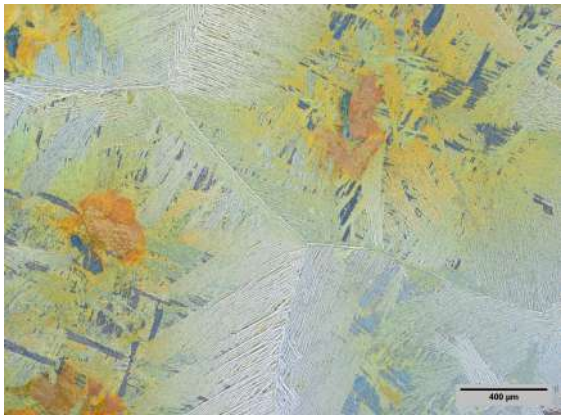

(b) Ti6.5Cu5Zr 1000 °C/30 h

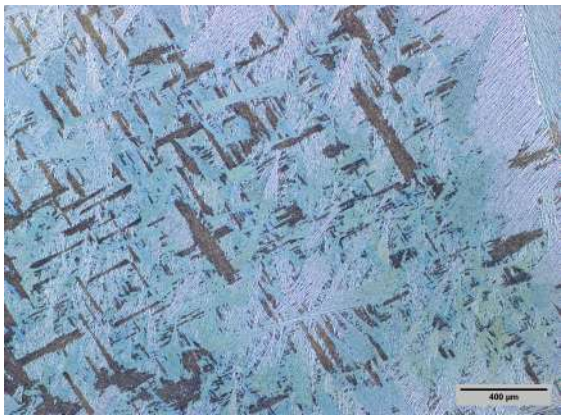

(c) Ti6.5Cu8Zr 1000 °C/30 h

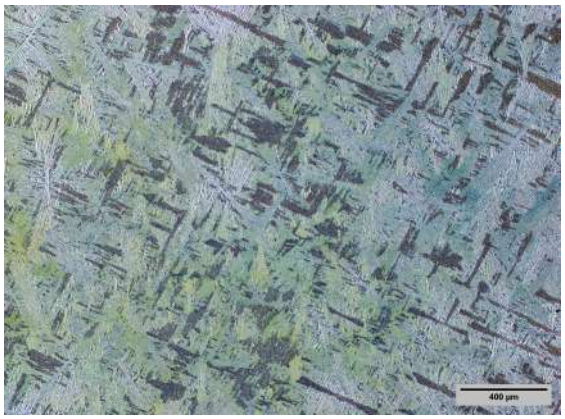

(d) Ti6.5Cu10Zr 1000 °C/30 h

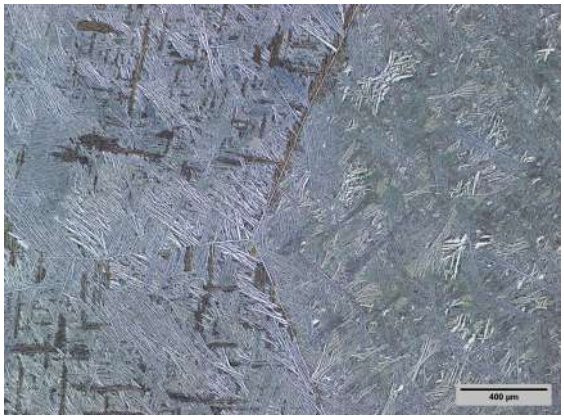

(e) Ti6.5Cu12Zr 1000 °C/30 h

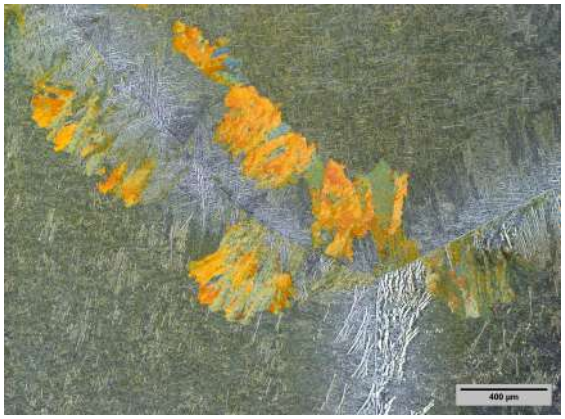

(f) Ti6.5Cu15Zr 1000 °C/30 h

Figure 18: LOM images of the heat-treated (1000 °C for 30 h) sample series Ti6.5CuxZr (x = 3, 5, 8, 10, 12, 15 wt%)

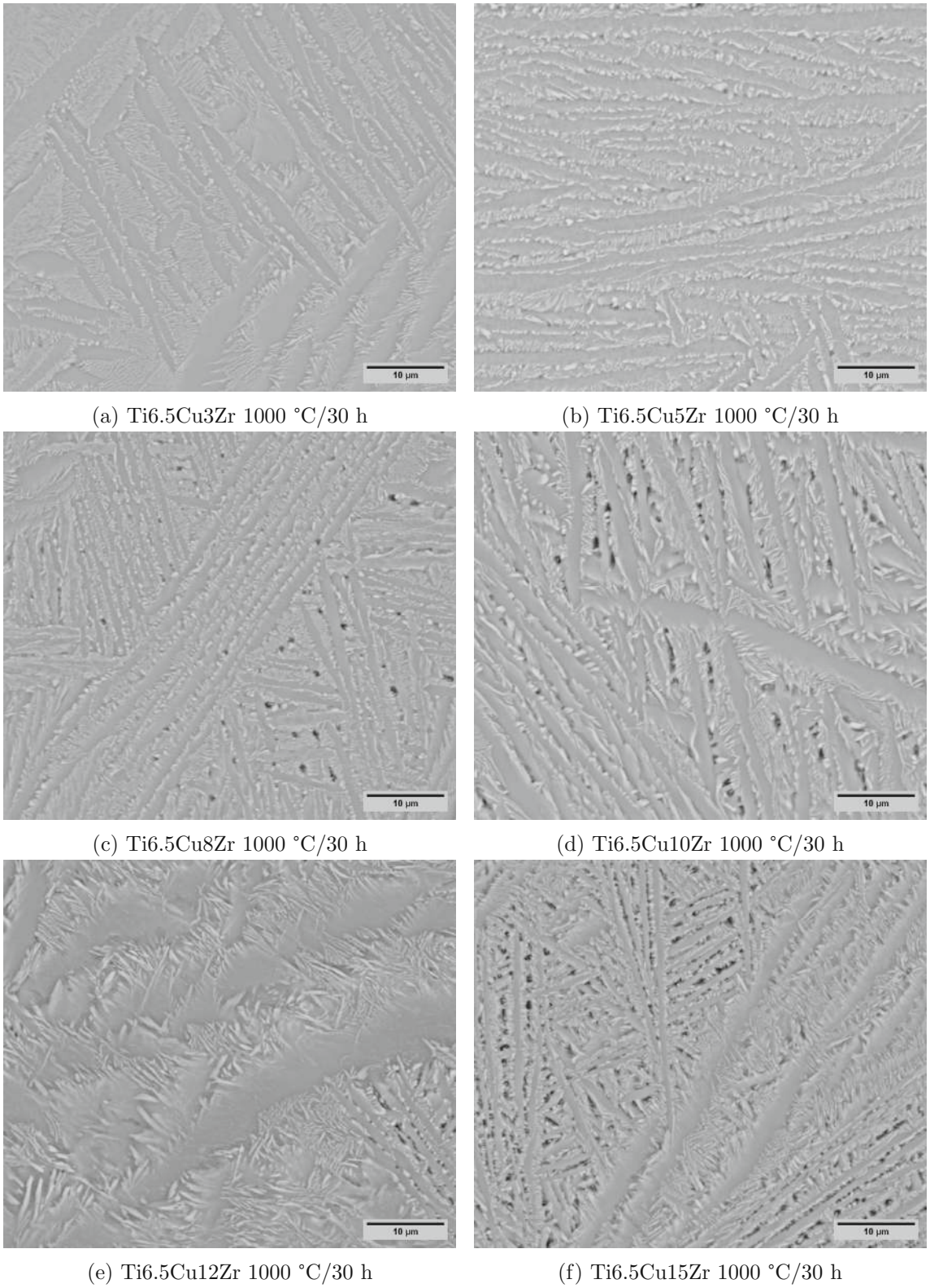

(a) Ti6.5Cu3Zr 1000 °C/30 h

(b) Ti6.5Cu5Zr 1000 °C/30 h

(c) Ti6.5Cu8Zr 1000 °C/30 h

(d) Ti6.5Cu10Zr 1000 °C/30 h

(e) Ti6.5Cu12Zr 1000 °C/30 h

(f) Ti6.5Cu15Zr 1000 °C/30 h

Figure 19: SEM images of the heat-treated (1000 °C for 30 h) sample series Ti6.5CuxZr (x = 3, 5, 8, 10, 12, 15 wt%)

The HV10 measurements of all previously mentioned samples as well as a reference sample Ti6.5Cu produced via arc furnace, provided by supervisor Dipl.-Ing. Ella Staufer, are shown in Figure 20. Since the reference sample was not heat-treated, only the hardness value of the as-cast condition is available. The sample series TixZr shows significantly lower hardness of approximately 150 up to 200 HV10 compared to Ti6.5CuxZr samples with a hardness of up to 322 HV. The addition of 3 wt% Zr to the Ti6.5Cu matrix results in an initial hardness decrease of about 20 HV10, indicating an improvement in ductility due to Zr [16]. Nevertheless, it can be observed that with increasing zirconium content, there is a rise in hardness in both sample series. This can be attributed to the increasing grain refinement with increasing Zr content. The heat treatment results in a reduction in hardness of approximately 20 HV10 because of the coarser microstructure.

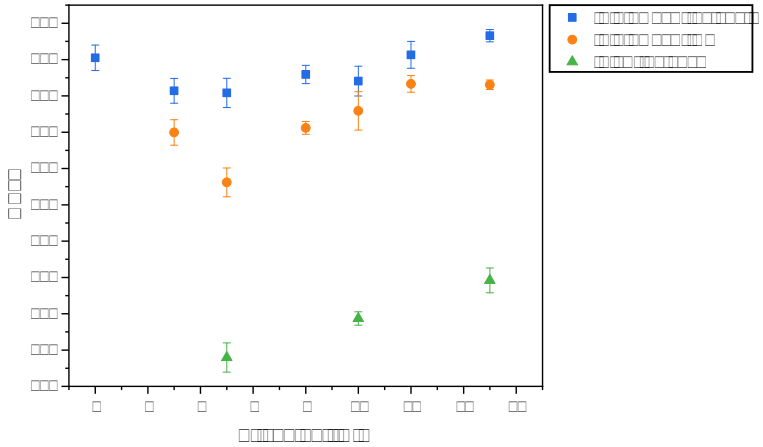

Figure 20: Results of the hardness measurements HV10 of the sample series TixZr and Ti6.5CuxZr. For reference the hardness result of Ti6.5Cu was added.

Figure 21 depicts the XRD measurements of the as-cast samples. In addition to α and β-titanium, the intermetallic phase Ti_2Cu was detected in all samples. This result is not surprising, even though the eutectoid phase could only be observed in the SEM in the Ti6.5Cu3Zr sample (Figure 16a). The eutectoid transformation in Ti-Cu alloys is an active transformation, meaning it is not suppressed by fast quenching [11]. Therefore, the rapid cooling in the arc furnace should not hinder the eutectoid transformation. However, it likely restricted the growth of the eutectoid phase, resulting in a size that is not resolvable under SEM.

With increasing zirconium content, the peaks shift to the left due to a higher concentration of zirconium being incorporated into the crystal lattice, resulting in deformation of the lattice. This can be observed in the increase of lattice parameter a and c of the hexagonal crystal structure of α-Ti with increasing Zr content (Figure 23). The c/a ratio remains approximately at 1.58, with a slight increase with the addition of 15 wt% Zr, which may be caused by inaccuracies of the method.

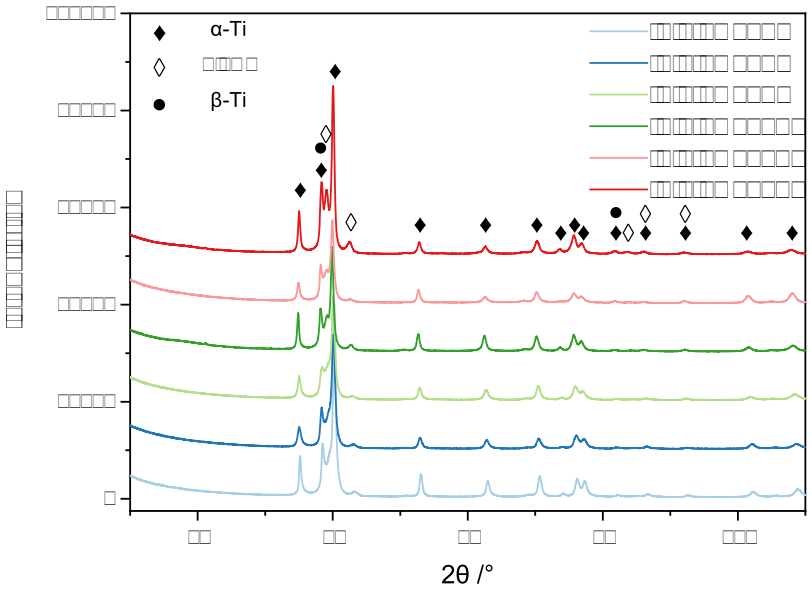

Figure 21: XRD measurements of the samples series Ti6.5CuxZr in the as-cast state (x = 3, 5, 8, 10, 12, 15 wt%)

To better visualize the XRD measurements of the heat-treated samples, detailed insets with a logarithmic scale were added to Figure 22, in addition to the overview. The three phase (α, β and Ti_2Cu), which were detected in the as-cast samples, were also measured after the heat treatment. The intensities of the peaks vary throughout the sample series, which was not observed in the as-cast samples. It is noteworthy that Ti_2Cu is more pronounced. This observation aligns with the SEM results, where an eutectoid microstructure was resolved. In the detailed insets an unidentified peak at 87.8° for the samples with 3, 5 and 8 wt% is visible. This peak could be attributed to the hexagonal intermetallic phase $Cu_{1.35}Zr_{0.825}Ti_{0.825}$, which overlaps oftentimes with α-titanium.

Similar to the as-cast samples, a leftward shift of the peaks can be observed with increasing zirconium concentration. Lattice parameter a increases with increasing Zr content, whereas the lattice parameter c decreases above a Zr concentration of 8 wt% (Figure 23). Nevertheless, the parameter c is higher than that of pure Ti at 4.67 Å. The c/a ratio decreases as well due to the reduction in the parameter c. In general, the lattice parameter a and c are higher in the heat-treated condition compared to the as-cast samples.

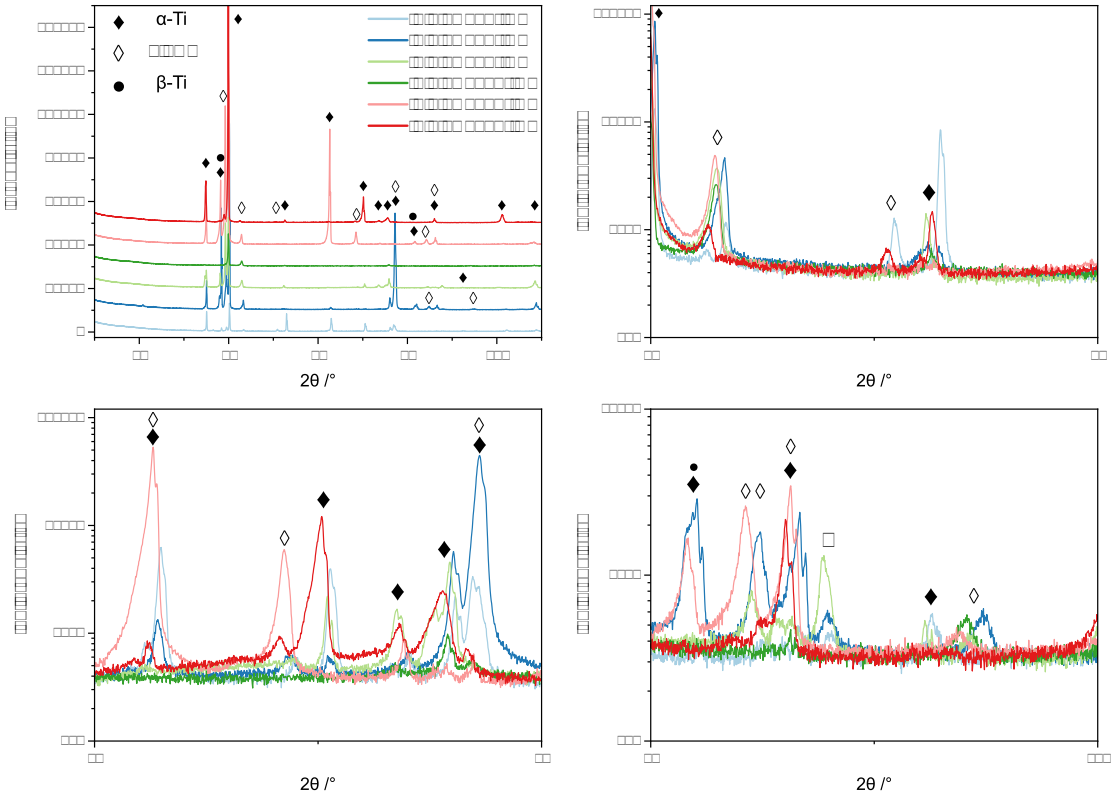

Figure 22: XRD measurements of the samples series Ti6.5CuxZr (x = 3, 5, 8, 10, 12, 15 wt%) after the heat treatment (1000 °C for 30 h). In addition to the overview, also detailed insets with a logarithmic scale are added.

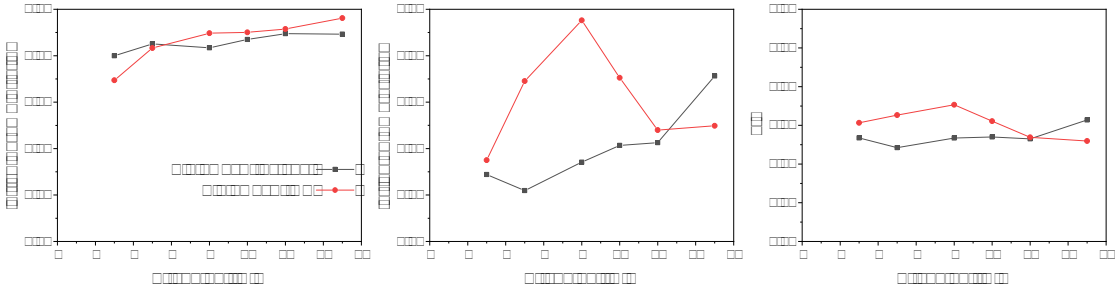

Figure 23: Lattice parameter a and c and the c/a ratio of the Ti6.5CuxZr sample series in the as-cast and heat-treated condition depending on Zr content.

4.2 Sintering - TixZrH$_2$

Figures 24 and 25 show the microstructure of TixZrH$_2$ samples (x = 3, 5 and 10 wt%; nominal Zr contents: 2.94, 4.89, 9.79 wt%) after vacuum sintering, whose powder mixture was mixed in the Turbula for 1 h. Hence, this sample series will be referred to as 'mixed'. The powder mixture Ti5ZrH$_2$ could be successfully pressed in contrast to Ti3ZrH$_2$ and Ti10ZrH$_2$. The inability to press the powder mixture can be attributed to the globular titanium powder (Figure 7a). Therefore, they were sintered as powder fillings, which explains the high porosity. Table 8 summarizes the densities of the mixed samples before and after the heat treatment of 1000 °C for 1 h. Ti5ZrH$_2$, as the only pressed sample, reaches a density up to 93 % of the theoretical density, which is still lower than the densities achieved by the other manufacturing methods discussed in this thesis. After the heat treatment the percentage of the theoretical density increases by approximately 2%.

Table 8: Density of mixed TixZrH$_2$ samples in as-sintered and heat-treated condition; standard deviation of balance assumed to be 0.1 mg due to single weighing of entire sample.

	as-sintered		heat-treated	
sample	density g/cm^3	% theoretical density	density g/cm^3	% theoretical density
Ti3ZrH$_2$	4.120	91.01	4.201	92.81
Ti5ZrH$_2$	4.218	92.81	4.357	95.88
Ti10ZrH$_2$	4.114	89.63	4.142	90.23

Vacuum sintering led to equiaxed grains (Figure 24a, c, e) and a α/β matrix (Figure 25a, c, e), which became finer with increasing zirconium content. It is important to note that an inhomogeneous distribution of Zr is observed. Therefore, the nominal zirconium content was not ensured consistently in the sample, resulting in an inconsistent microstructure.

To gain an initial understanding of the Zr distribution, point analyses were conducted. Point analyses of the mixed Ti10ZrH$_2$ sample in the as-sintered and heat-treated conditions are shown as examples to illustrate the variation in Zr content. The sample with the highest Zr concentration was chosen to demonstrate the results, as the measurement error rate is the lowest for this sample. A detailed investigation of the Zr distribution is discussed further below based on elemental mapping.

The measured points are marked in Figure 25e and f and the results are summarized in Table 9. It is to be noted that Figure 25e depicts a lower magnification. Point 1 in the as-sintered sample analyses an agglomeration of Zr. Therefore, a Zr content of 11.90 wt% is measured. The other two points measured in the equiaxed grains show a Zr content of approximately 4 wt%, which is significantly lower than the desired Zr content of 9.79 wt% (Table 5). In this instance, the low Zr content could be attributed to the inhomogeneous distribution and agglomeration of Zr. The inhomogeneous microstructure is visible near the former ZrH$_2$ particles. The zirconium content around the pores results in a lamellar structure, as seen in Figure

24c (it is to be noted that the magnification is lower than in the other figures to better visualize the pores).

A subsequent heat treatment was applied to promote the dissolution of the zirconium particles. After the heat treatment at 1000 °C for 1 h, the subsequent water quenching restrained the potential separation of zirconium at the grain boundaries, as discussed in Chapter 2.3.2. The heat treatment resulted in a more homogeneous Zr content, which can also be observed in the EDX point analysis (Table 9). The Zr content ranges from 4.52 to 5.46 wt%, exceeding that of the as-sintered sample. The higher Zr content can be explained by the more homogeneous distribution and break-up of the Zr agglomerates, which were observed in the as-sintered samples. Nevertheless, the Zr content is lower than the desired nominal Zr content of 9.79 wt% (Table 5).

Several factors could contribute to this discrepancy, including an incomplete reaction of ZrH_2. However, the absence of a ZrH_2 phase in the XRD analysis, as shown below in Figure 26, suggest that Zr has been incorporated into the lattice rather than remaining in its initial hydride form, as ZrH_2 begins to decompose at around 780 °C [23]. Due to the extremely low vapour pressure of metallic Zr of only $6.51 \cdot 10^{-13}$ Pa at 1000 °C [47], its evaporation is considered unlikely. Therefore, the apparent loss of Zr cannot be clearly attributed at this stage and may be related to redistribution, incorporation into other phases, or limitations in the analytical methods used. Further investigations, such as TGA, ICP and XRF, are required to better understand the transformation and behaviour of Zr during processing.

The more homogenous Zr distribution due to heat treatment led to a change in the microstructure to lamellar α laths (Figure 24b, d, f). Despite the heat treatment, the expected grain growth is not visible as the more homogenous Zr content led to an overall grain refinement. It would be expected to see a grain refinement with increasing zirconium content as was seen in the as-sintered samples, but it cannot be observed in the heat-treated condition.

Table 9: Zirconium content in mixed sample Ti10ZrH_2 in as-sintered and heat-treated condition measured via EDX point analysis. The points are marked in Figure 25e and f.

	Zr content (wt%)	
Point	as-sintered	heat-treated
1	11.90	4.56
2	4.01	4.52
3	4.05	4.81
4		5.46

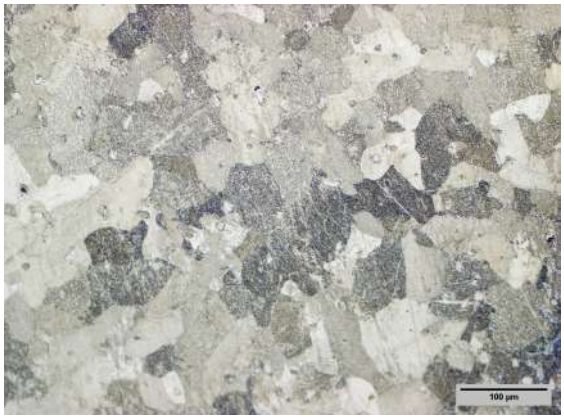

(a) $Ti3ZrH_2$ as-sintered

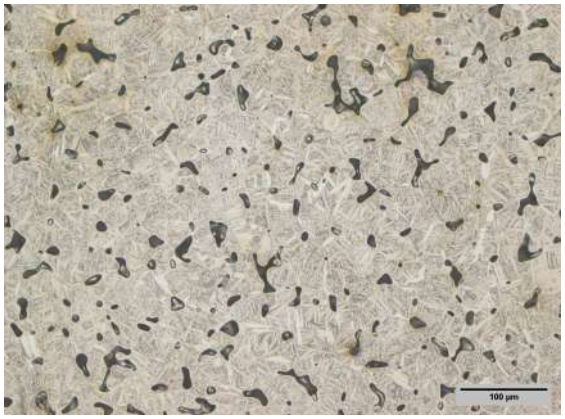

(b) $Ti3ZrH_2$ 1000 °C/1 h

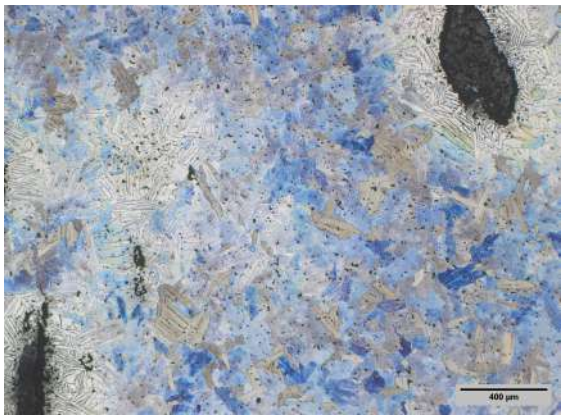

(c) $Ti5ZrH_2$ as-sintered with inhomogeneous Zr

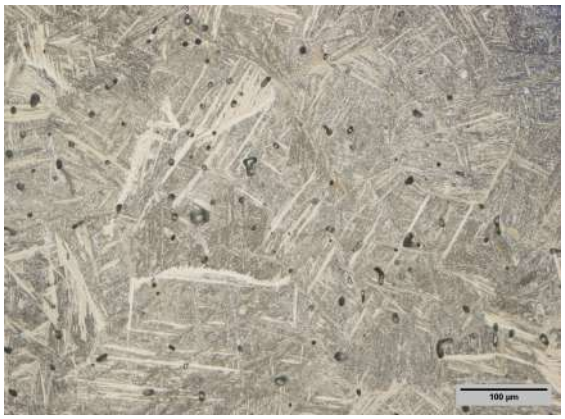

(d) $Ti5ZrH_2$ 1000 °C/1 h

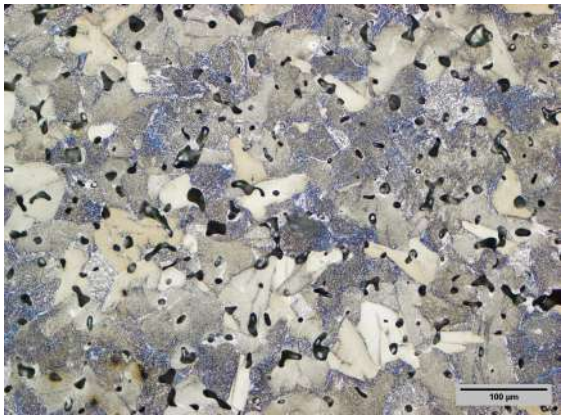

(e) $Ti10ZrH_2$ as-sintered

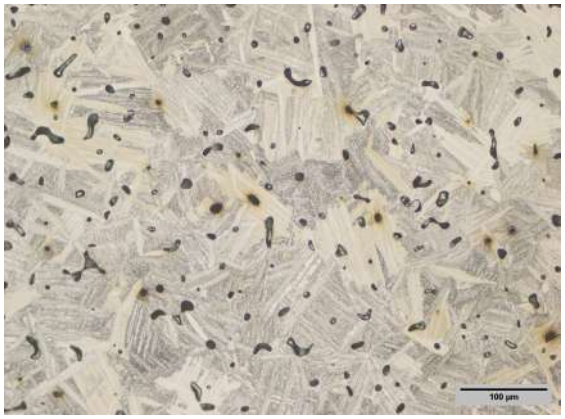

(f) $Ti10ZrH_2$ 1000 °C/1 h

Figure 24: LOM images of the mixed sample series $TixZrH_2$ in the as-sintered (a, c, e) and heat-treated (1000 °C for 1 h and water quenched) (b, d, f) state.

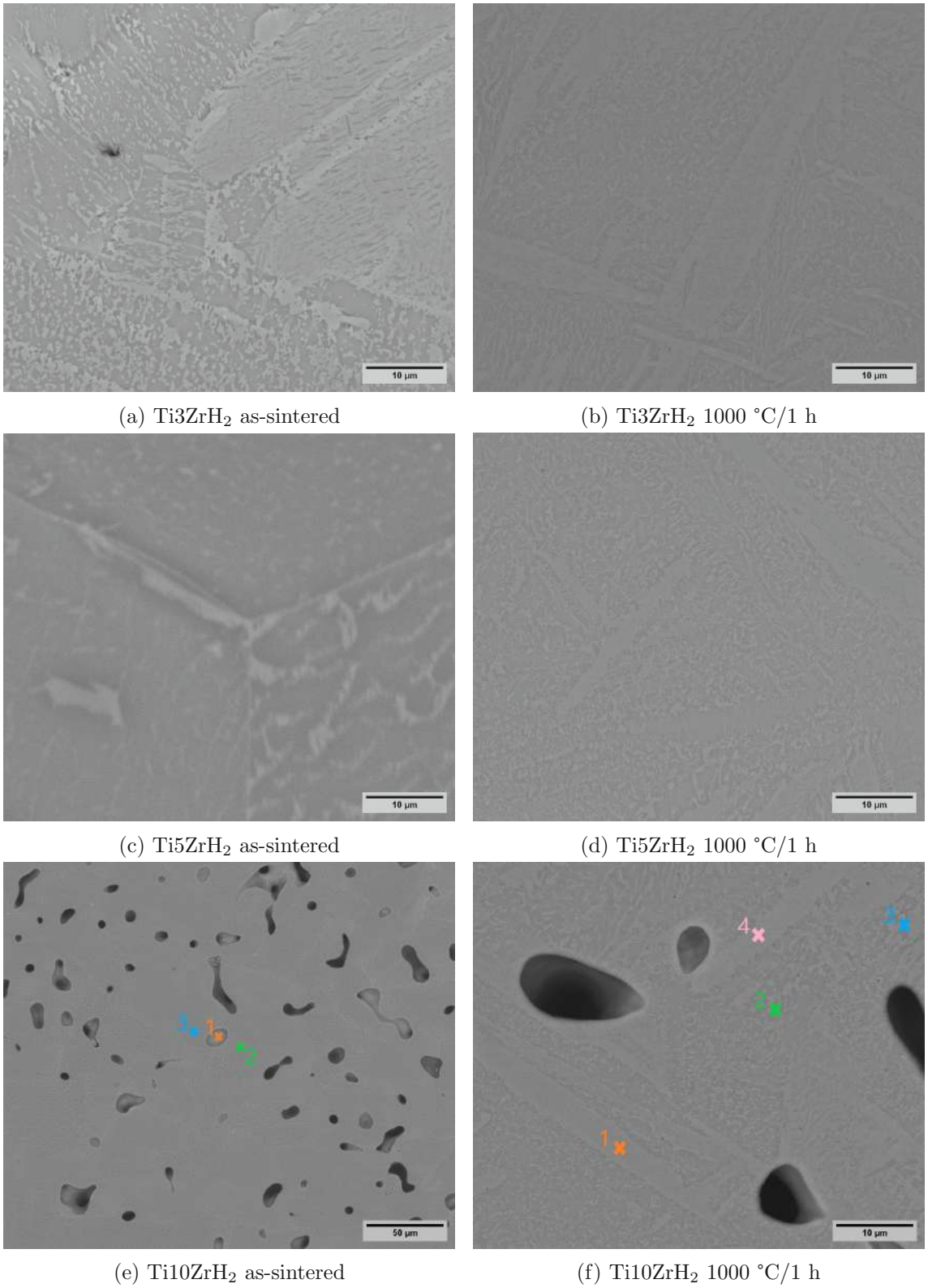

(a) $Ti3ZrH_2$ as-sintered

(b) $Ti3ZrH_2$ 1000 °C/1 h

(c) $Ti5ZrH_2$ as-sintered

(d) $Ti5ZrH_2$ 1000 °C/1 h

(e) $Ti10ZrH_2$ as-sintered

(f) $Ti10ZrH_2$ 1000 °C/1 h

Figure 25: SEM images of the mixed sample series $TixZrH_2$ in the as-sintered (a, c, e) and heat-treated (1000 °C for 1 h and water quenched) (b, d, f) state. The measured points via EDX point analysis are marked in Figure (f).

Figures 26a and b show XRD measurements of the mixed sample Ti10ZrH_2 during the three stages of production (powder form, as-sintered and lastly after heat treatment and water quenching). The α-titanium peaks shift to the left after the sintering, because of substitutional solid solution of Zr into α-Ti lattice. With each step the peaks shift more to the left, which indicates the increasing dissolution of zirconium in the titanium lattice. The prominent β-titanium peak at 38.8° after the sintering is also noticeable. The peak at 32.5° is the most prominent signal for zirconium hydride, which was only detectable in the powder stage. In the detailed inset of the diffractogram, the peaks for zirconium hydride at 52° and 55.5° are also exclusively visible in the powder form and completely diminish in the sintered and heat treatment state. Furthermore, the peak at 59°, which represents titanium hydride, cannot be seen for any sample. This indicates the successful release of hydride, due to the low solid solubility (as discussed in Chapter 2.3.3).

Figures 26c and d show the XRD measurements of the three mixed samples in the as-sintered and heat-treated state. No major differences are noticeable between the two states. As previously discussed, no ZrH_2 or TiH_2 peaks were detectable. Consequently, only α and β-titanium phases were identified. With an increasing zirconium content, the peaks shift towards lower angles due to the higher concentration of incorporated zirconium. Figure 27 depicts the lattice parameter a and c as well as the c/a ratio of the mixed sample series. The mixed Ti10ZrH_2 powder depicts lower lattice parameters, because Zr is not yet incorporated into the lattice of Ti. Therefore, the parameters are approximately identical to the parameters of pure Ti (a = 2.95 Å , c = 4.68 Å [6]). The as-sintered samples exhibit a clear increase in lattice parameters with increasing Zr content. The lattice parameters values of samples with 3 and 5 wt% Zr are higher after the heat treatment, as a more homogeneous Zr content is guaranteed. The Ti10ZrH_2 sample, however, shows a decrease in both lattice parameters, which does not align with the SEM and EDX mapping results. This discrepancy may be due to methodological error, as the Rietveld refinement used to obtain these values is highly sensitive to errors. The c/a ratio remains for all three sample stages (powder, as-sintered, heat-treated) the same at approximately 1.58, which aligns with the literature [44–46].

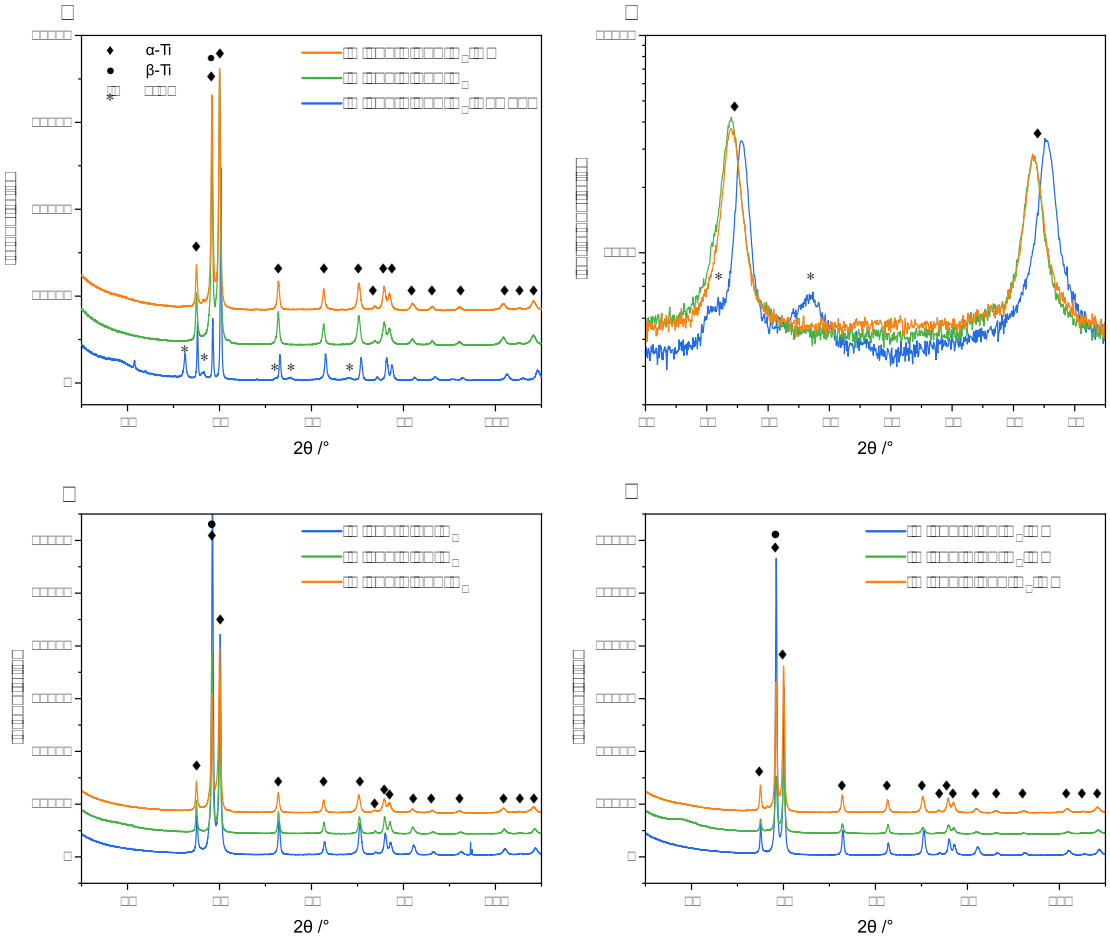

Figure 26: XRD measurements of the mixed sample Ti10ZrH$_2$ in powder, as-sintered and heat-treated state (overview and inset) (a, b) as well as of as-cast (c) and heat-treated (c) TixZrH$_2$ samples (x = 3, 5, 10 wt%; nominal Zr contents: 2.94, 4.89, 9.79 wt%).

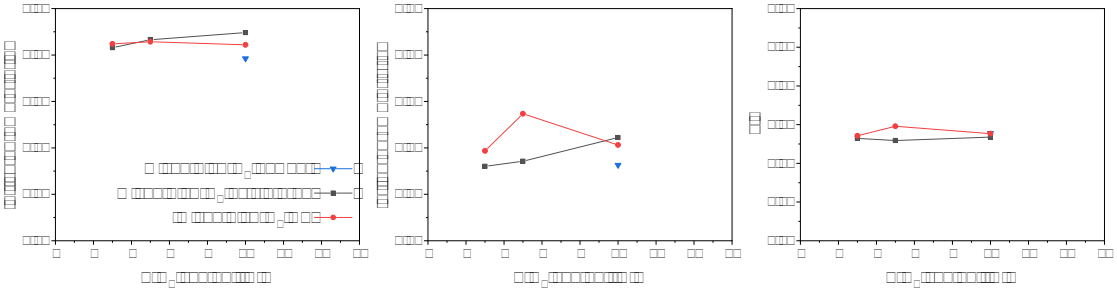

Figure 27: Lattice parameter a and c as well as the c/a ratio of the mixed TixZrH$_2$ samples in the as-sintered and heat-treated state as a function of ZrH$_2$ concentration. For reference, the parameters of the mixed Ti10ZrH$_2$ powder sample is also depicted.

To ensure the breaking up of the ZrH_2 particles, a 17 h milling process was initiated before sintering, therefore these samples are referred to as 'milled'. It is evident that the milling was successful as no ZrH_2 particles or big pores from former particles could be found in any sample, compared to the mixed samples. The high porosity is a result of insufficient pressing, as the green body did not stay compact. The density of the as-sintered and heat-treated samples is summarized in Table 10. The density of the milled sample series, which was insufficiently pressed, is slightly lower than that of the mixed sample series. This is despite the fact that the latter was sintered as a powder compact in a crucible. The heat-treated mixed $Ti5ZrH_2$ sample is an exception as it was more efficiently pressed compared to the milled sample series, hence exhibits a higher density. The lower density of the milled sample series can also be observed in Figure 28, where the porosity is more prominent compared to the mixed sample series shown in Figure 24. Nevertheless, the density in both sample series is not satisfactory. The heat treatment results in compaction and an increase in density, similar to the mixed sample series. Due to the high porosity, HV10 measurements of the mixed and milled sample series were not conducted, as the results would not be reliable.

Table 10: Density of milled $TixZrH_2$ samples in as-sintered and heat-treated condition; standard deviation of balance assumed to be 0.1 mg due to single weighing of entire sample.

	as-sintered		heat-treated	
sample	density g/cm^3	% theoretical density	density g/cm^3	% theoretical density
$Ti3ZrH_2$ milled	4.065	89.79	4.138	91.41
$Ti5ZrH_2$ milled	3.619	79.64	4.181	91.99
$Ti10ZrH_2$ milled	4.042	88.06	4.283	93.32

The microstructure after sintering consists of equiaxed α grains (Figure 28a, c, e), which are more refined compared to the mixed sample series (Figure 24a, c, e). This is due to the more uniform distribution of Zr, caused by the prior milling process. However, a grain refinement cannot be observed with increasing Zr content as would be expected. Nevertheless, because of the slow cooling after the sintering zirconium segregated at the grain boundaries of the equiaxed α grains (as discussed in Chapter 2.3.2). The Zr enrichment is visible under the SEM in Figure 29a, c and e. To gain an initial understanding of Zr distribution, the Zr content and distribution was be analysed via EDX point analysis. The results of the measurement of the milled sample $Ti10ZrH_2$ are summarized in Table 11 and the selected points are marked in Figure 29e and f. The as-sintered sample shows in point 1 a Zr enrichment at a grain boundary, therefore the Zr content is measured to be 16.38 wt%. The content decreases in the equiaxed grain to approximately 4.8 wt%, exceeding the 4 wt% in the mixed as-sintered sample. Nevertheless, the measured Zr content is well below the desired nominal Zr of 9.79 wt% (Table 5). As previously discussed, the behavior of Zr during processing and its loss require further investigation.

Table 11: Zirconium content in milled sample Ti10ZrH_2 in as-sintered and heat-treated condition measured via EDX point analysis. The points are marked in Figure 29e, f.

	Zr content (wt%)	
Point	as-sintered	heat-treated
1	16.38	4.23
2	4.96	5.99
3	4.74	5.78
4		7.33

In contrast to the lamellar microstructure in the mixed sample series, the formation of a bi-modal microstructure is observed after the heat treatment and water quenching. The formation of a bi-modal microstructure could be achieved by a heat treatment below the α/β transus temperature, whereas a fully lamellar microstructure by heat treatment above the α/β transus temperature [6]. As both sample series were sintered and heat-treated at the same temperatures (1100 and 1000 °C respectively), the change in microstructure cannot be explained by the production parameters. The different microstructures could be attributed to the higher Zr content in the milled sample series (comparison of Table 9 and 11). Generally, it can be stated that the yield stress and ductility of samples with a bi-modal microstructure enhance compared to a fully lamellar microstructure as the α colony size is typically more refined than the lamellar structure [6].

The bi-modal microstructure consists of equiaxed primary α grains and fine lamellar α/β colonies. With increasing Zr content, the equiaxed grains become more refined and the laths more pronounced (Figure 28b, d, f). The secondary α and β lamellae are visible in Figure 29b, d, f. The Zr content in the equiaxed grain was measured via EDX point analysis to be 4.23 wt% (Table 11). In the α and β colonies, the Zr content ranges from 5.99 to 7.33 wt%, exceeding the highest measured content of 5.26 wt% in the mixed heat-treated sample. Therefore, it can be concluded that the milling process ensured a higher overall Zr content in the samples, and the heat treatment followed by water quenching resulted in a more homogeneous Zr distribution.

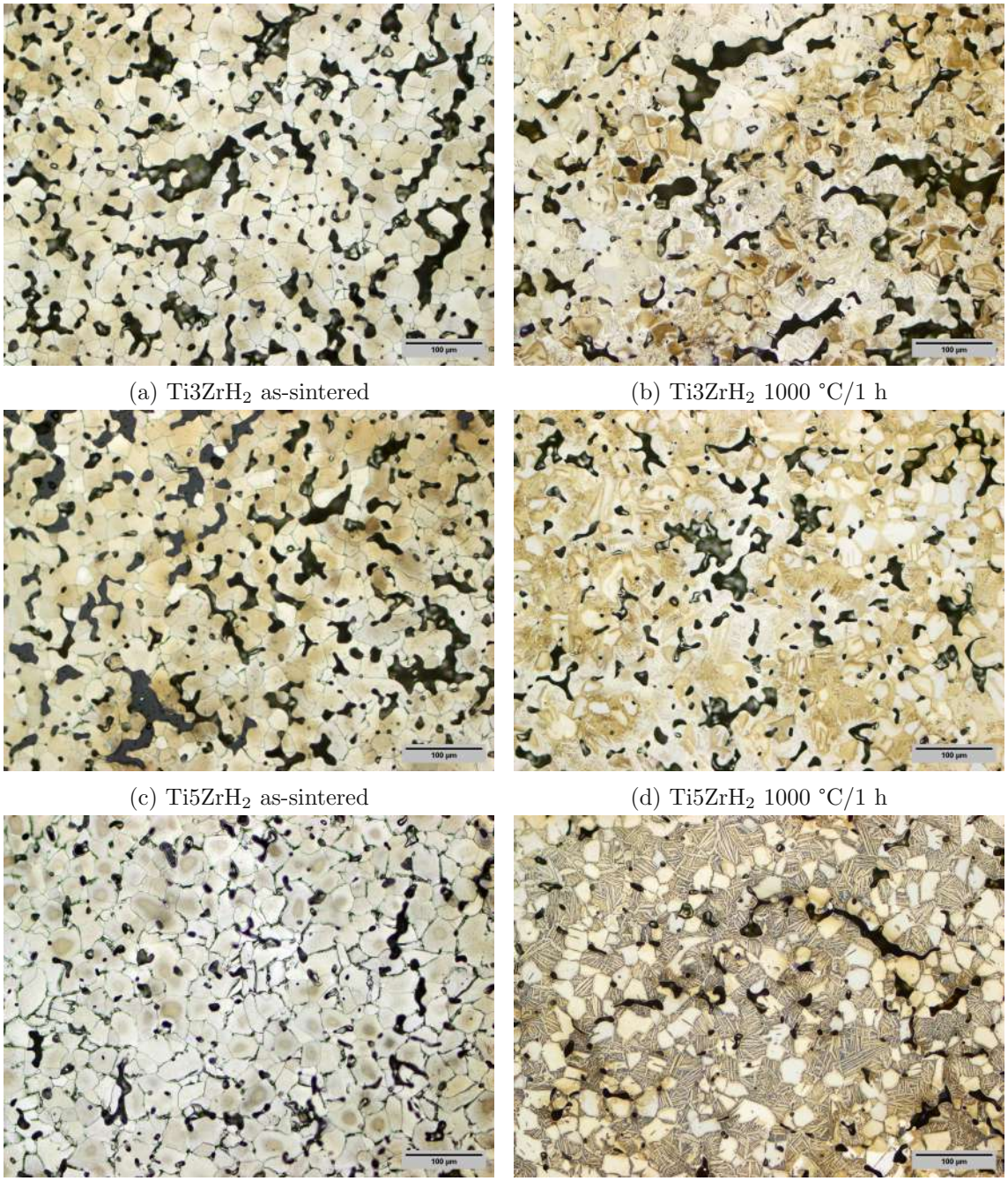

(a) $Ti3ZrH_2$ as-sintered (b) $Ti3ZrH_2$ 1000 °C/1 h

(c) $Ti5ZrH_2$ as-sintered (d) $Ti5ZrH_2$ 1000 °C/1 h

(e) $Ti10ZrH_2$ as-sintered (f) $Ti10ZrH_2$ 1000 °C/1 h

Figure 28: LOM images of the milled sample series $TixZrH_2$ in the as-sintered (a, c, e) and heat-treated (1000 °C for 1 h and water quenched) (b, d, f) state.

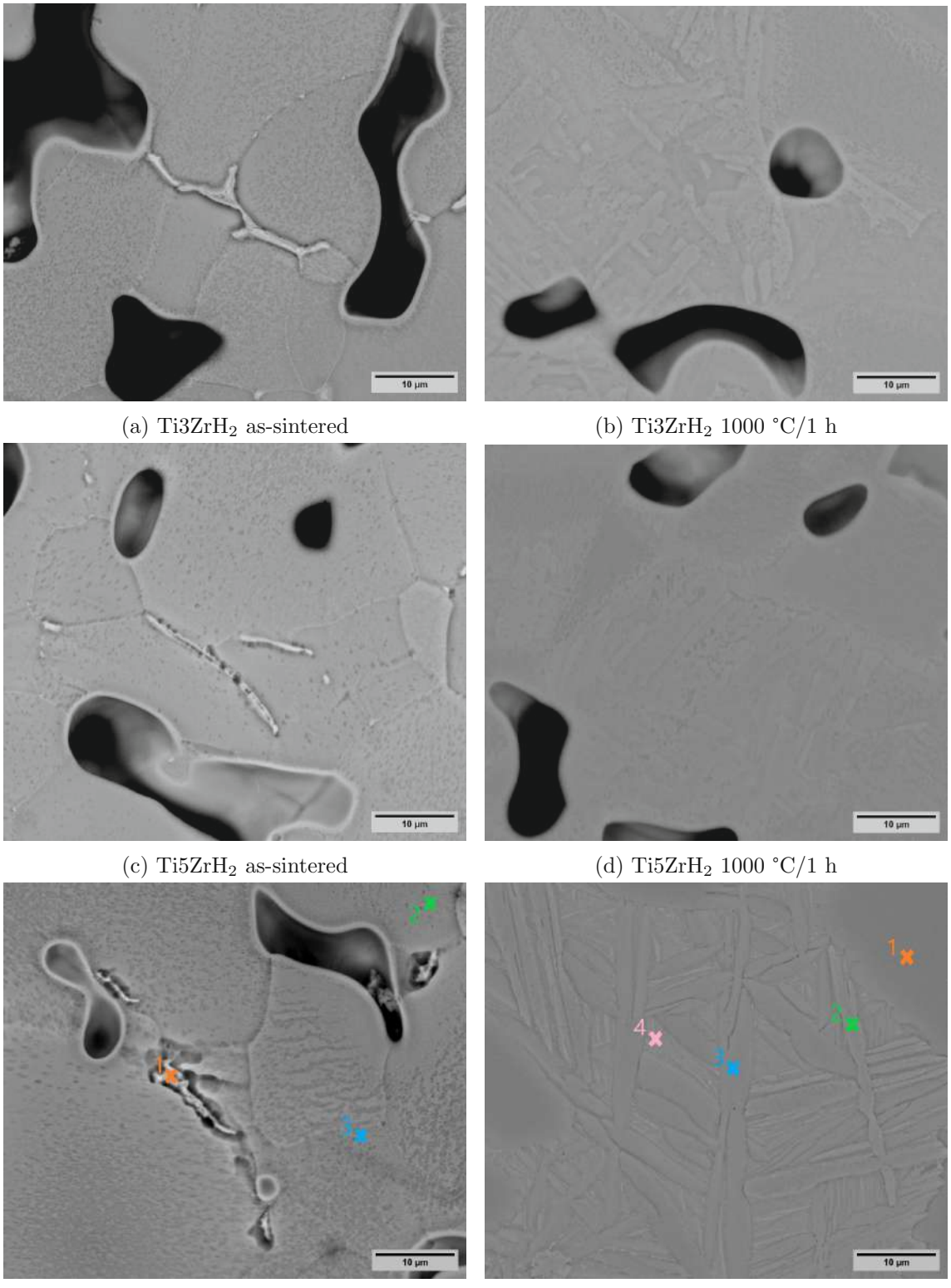

(a) $Ti3ZrH_2$ as-sintered

(b) $Ti3ZrH_2$ 1000 °C/1 h

(c) $Ti5ZrH_2$ as-sintered

(d) $Ti5ZrH_2$ 1000 °C/1 h

(e) $Ti10ZrH_2$ as-sintered

(f) $Ti10ZrH_2$ 1000 °C/1 h

Figure 29: SEM images of the milled sample series $TixZrH_2$ in the as-sintered (a, c, e) and heat-treated (1000 °C for 1 h and water quenched) (b, d, f) state. The measured points via EDX point analysis are marked in Figure e and f.

To better visualize the dispersion of Zr in the matrix, mappings of the milled sample Ti10ZrH_2 were conducted. Figure 30a and c depict the milled sample Ti10ZrH_2 in the as-sintered state with zirconium visualized in red. It is evident that Zr segregated at the grain boundaries of the equiaxed α grains, resulting in a low zirconium content in the grains, which is consistent with the point analysis. The subsequent heat treatment and water quenching resulted in a bi-modal microstructure with a more uniform dispersion of Zr in the matrix (Figures 30b and d). However, an element partitioning effect can be observed, as the equiaxed α grains contain less zirconium, than in regions with lamellar α colonies. As Zr is typically classified as a neutral element regarding Ti, a partitioning effect that generally affects strong stabilizers, would not be expected [6]. Nevertheless, Zr partitions into the colonies that form from prior β grains. This observation suggests that zirconium exhibits weak β-stabilizing properties, as also noted in [48]. Huang et al. [49] detected that the partitioning effect of Ti6Al4V does not depend on the solution time. However, a decreasing vanadium content, a β stabilizer, in the β phase was observed with increasing temperature. Therefore, it could be investigated whether a higher temperature would minimize the partitioning effect of Zr in the TixZrH_2 samples.

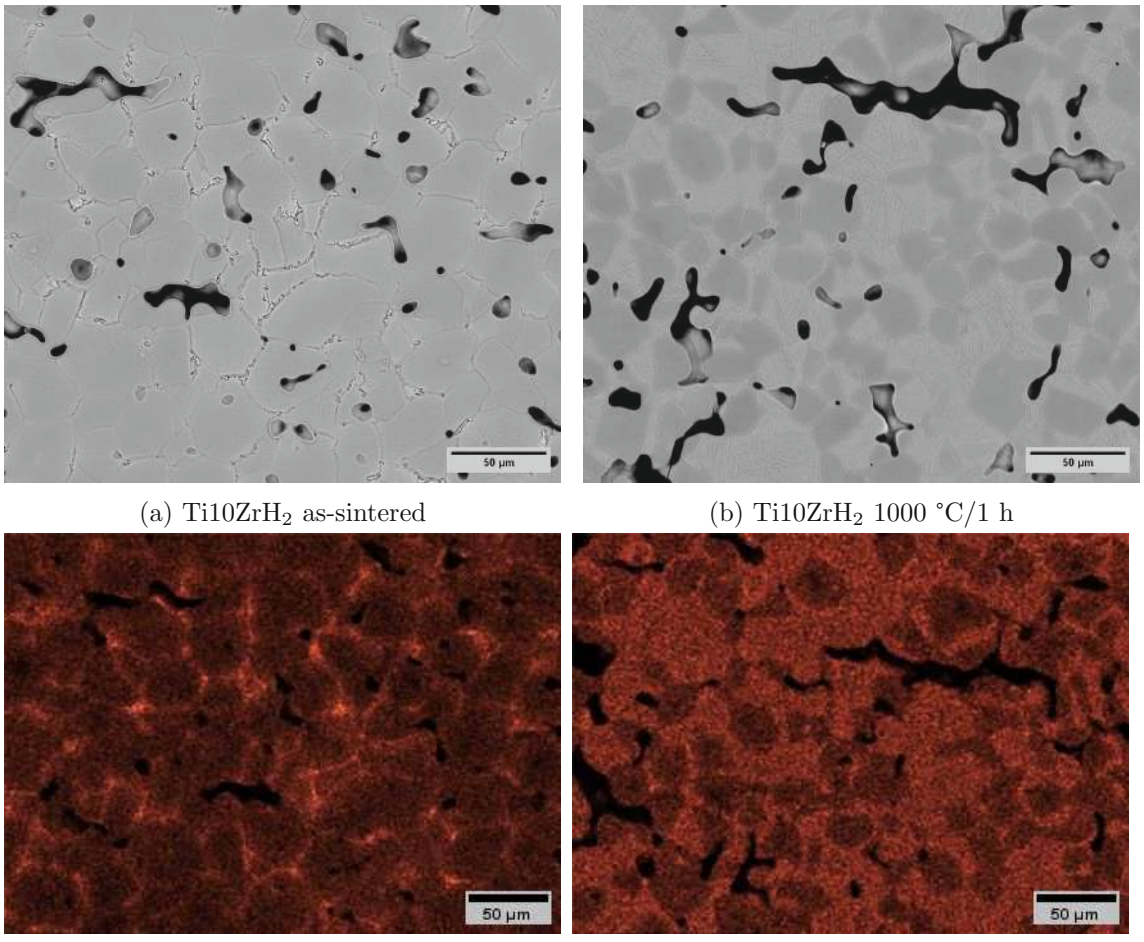

(a) Ti10ZrH_2 as-sintered

(b) Ti10ZrH_2 1000 °C/1 h

(c) Mapping of Ti10ZrH_2 as-sintered

(d) Mapping of Ti10ZrH_2 1000 °C/1 h

Figure 30: SEM images of milled sample Ti10ZrH_2 in the as-sintered (a, c) and heat-treated state (b, d) and the corresponding mapping images.

The XRD measurements of the milled sample series in the as-sintered and heat-treated condition are summarized in Figure 31. Similar to mixed samples, α and β-Ti could be detected with a leftward shift with increasing Zr content. Both lattice parameters a and c increase, indicating that a higher Zr content is being substitutionally incorporated into the α-Ti lattice (Figure 32). The c/a ratio remains constant at approximately 1.58, similar to the mixed sample series. Compared to the mixed samples, titaniumoxides were detected in samples as-sintered Ti5ZrH_2 and heat-treated Ti3ZrH_2. Different titaniumoxides could be identified like $TiO_{0.48}$, TiO and $Ti_2O_{0.59}$. Due to the high affinity of titanium for oxygen, the formation of titanium oxides at the edge of the sample is likely attributed to production errors.The observed coloration of the samples suggests oxidation, which is consistent with the XRD results. Nevertheless further analysis like an oxygen quantification would be required to verify the XRD results. Unfortunately, such analyses fall outside the scope of this thesis.

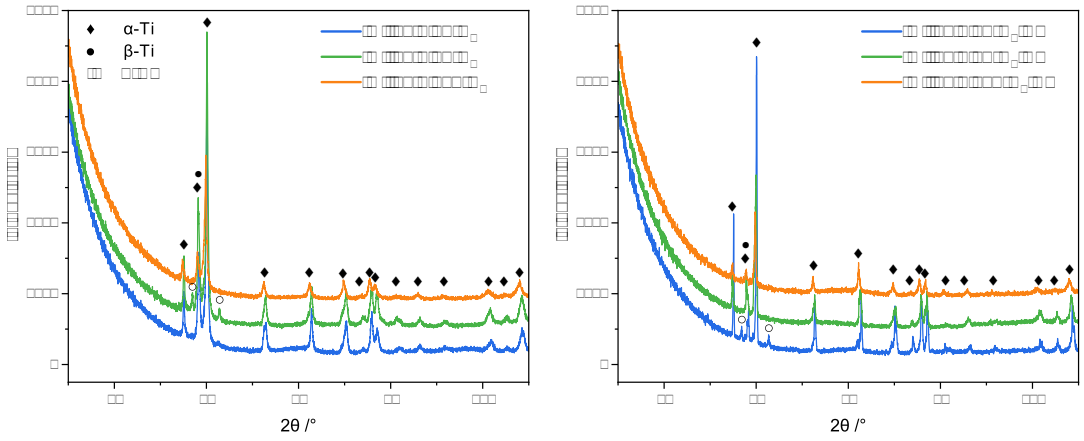

Figure 31: XRD measurements of the milled TixZrH_2 sample series in the as-sintered and heat-treated state.

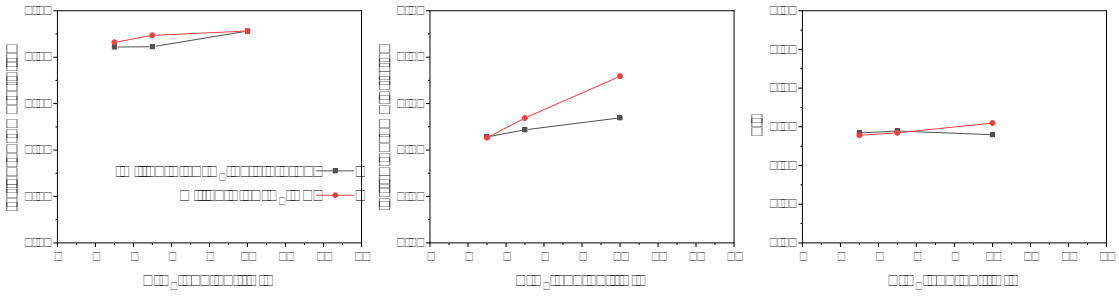

Figure 32: Lattice parameter a and c as well as the c/a ratio of the milled TixZrH_2 samples in the as-sintered and heat-treated state as a function of ZrH_2 concentration.

4.3 Hot Extrusion - TixZrO$_2$

The preparation of large amounts of Ti-Zr samples appears to be especially feasible when using ZrO_2. This approach was therefore applied for the hot extrusion process. To analyse the deformation effect, the hot-extruded samples with various ZrO_2 content (0.5, 1 and 2 wt%; nominal Zr contents: 0.37, 0.74 and 1.48 wt%) were examined in the extrusion direction (longitudinal) and perpendicular to it. The samples are optically dense and reach a density above 99.5 % of the theoretical density, as seen in Table 8.

Table 12: Density of TixZrO$_2$ samples in as-extruded and heat-treated condition; standard deviation of balance assumed to be 0.1 mg due to single weighing of sample.

	as-extruded		heat-treated	
sample	density g/cm^3	% theoretical density	density g/cm^3	% theoretical density
Ti0.5ZrO$_2$	4.528	100.52	4.497	99.83
Ti1ZrO$_2$	4.498	99.75	4.486	99.49
Ti2ZrO$_2$	4.530	100.24	4.494	99.45

After the hot extrusion, a columnar grain structure forms, which is identical in both examined directions (Figure 33). With increasing ZrO_2 content, a refinement of the laths can be observed, which is attributed to the zirconium. During the hot extrusion, the coarse ZrO_2 particles did not fully dissolve. The inhomogeneous particle size of the used ZrO_2 powder can be seen in Figure 7c. The undissolved particles are elongated in the extrusion direction, as seen in Figure 33c. The ZrO_2 particles, or the residue of these particles, are indicated by an arrow in the following figures. In Figure 33f, undissolved ZrO_2 particles in the perpendicular direction can be observed. The elongation of ZrO_2 particles is visible in Figure 35a and e.

EDX point analyses of the sample Ti0.5ZrO$_2$ were conducted in the as-extruded and heat-treated state. The measured points are marked in Figure 35a and b. The measured Zr content is summarized in Table 13. It is to be noted that oxygen was detected, but not quantified, as the result would not be reliable. The as-extruded Ti0.5ZrO$_2$ sample is depicted in a lower magnification to better demonstrate the decreasing Zr content with increasing distance to the ZrO_2 particle. The lowest measured Zr content of 0.22 wt% is slightly under the desired nominal Zr content of 0.37 wt% (Table 5), which is expected due to the undissolved ZrO_2 particles.

Table 13: Zirconium content in sample Ti0.5ZrO_2 in as-extruded and heat-treated condition measured via EDX point analysis. The points are marked in Figure 35a and b.

	Zr content (wt%)	
Point	as-extruded	heat-treated
1	48.27	71.76
2	2.24	2.14
3	0.22	0.50

The subsequent heat treatment at 1000 °C for 24 hours resulted in the dissolution of the majority of ZrO_2 particles, leading to a significant improvement in the materials microstructure. The decomposition temperature of ZrO_2 was determined by Thermogravimetric Differential Thermal Analysis (TG-DTA) at approximately 780 °C by Kondoh et al. [23], so the heat treatment temperature exceeded the decomposition temperature. Nevertheless, the complete dissolution of all ZrO_2 particles was not achieved, as visible in Figure 35b. The EDX point analyses confirm the presence of an undissolved ZrO_2 particle, with the Zr content decreasing as the distance from the particle increases. However, the Zr content remains at 0.5 wt%, which is higher than the expected 0.37 wt%, suggesting that the measurements are likely still too close to the particle to reliably represent the overall Zr content in the sample. EDX area analysis on sample Ti1ZrO_2 show an increase of Zr content from 0.34% (as-extruded) to 0.59 wt% due to the heat treatment. Therefore, it can be concluded that the incorporation of Zr into the Ti matrix was successful due to the heat treatment. The α and β microstructure did not change after the heat treatment (Figure 35). The heat treatment resulted in coarsening of the columnar grains. Similar to the as-extruded samples, there is no difference in the microstructure between the longitudinal and perpendicular directions relative to the extrusion direction. However, in contrast to the as-extruded samples, only a slight refinement with increasing zirconium content can be observed (Figure 34).

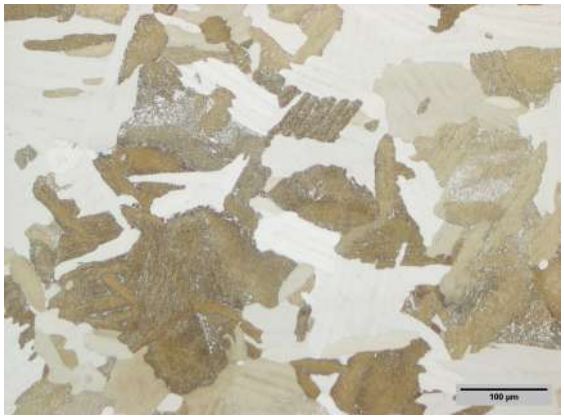

(a) $Ti0.5ZrO_2$ longitudinal

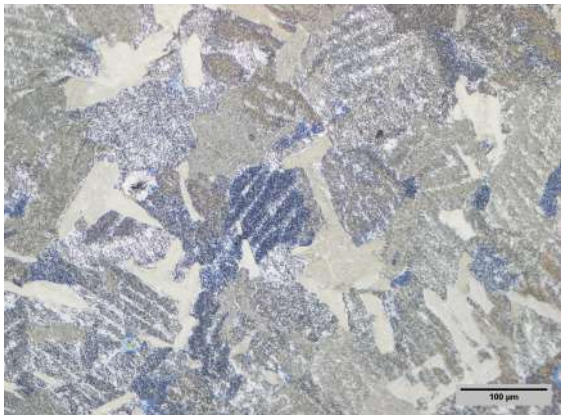

(b) $Ti0.5ZrO_2$ perpendicular

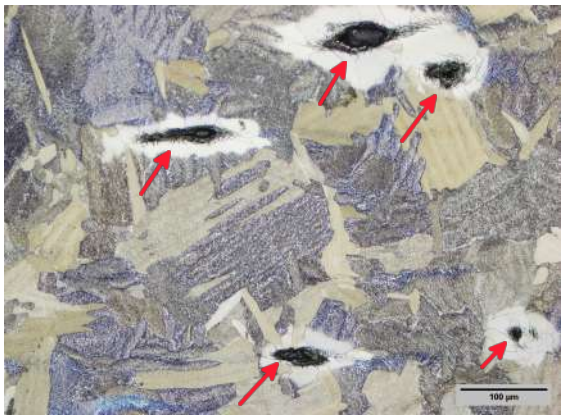

(c) $Ti1ZrO_2$ longitudinal

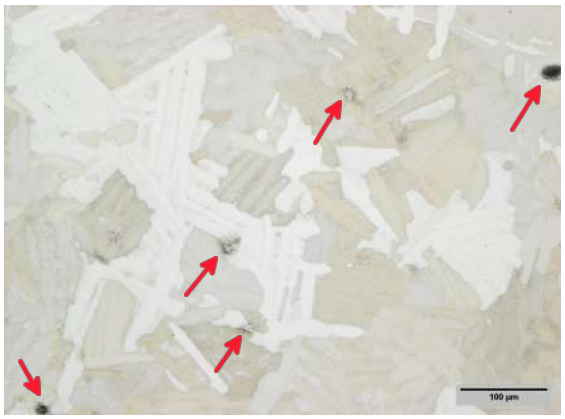

(d) $Ti1ZrO_2$ perpendicular

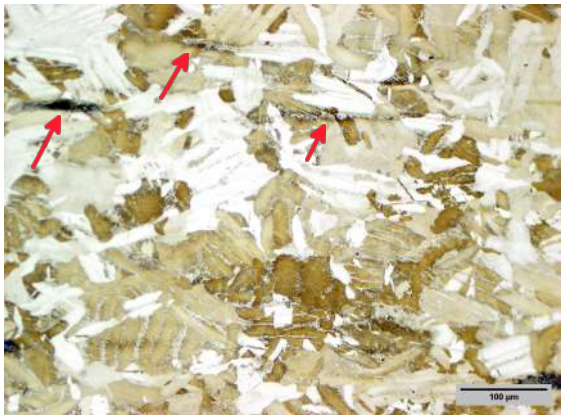

(e) $Ti2ZrO_2$ longitudinal

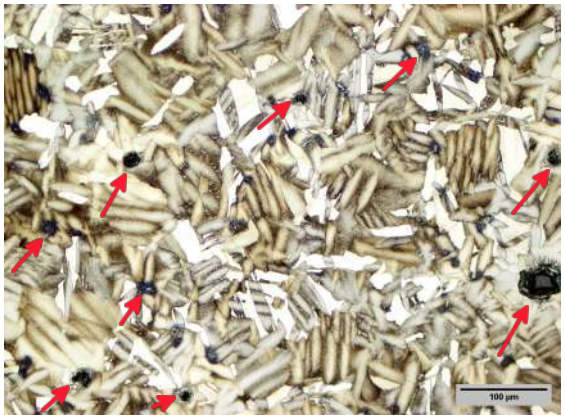

(f) $Ti2ZrO_2$ perpendicular

Figure 33: LOM images of the as-extruded $TixZrO_2$ (x = 0.5, 1, 2 wt%) sample series in extrusion direction (longitudinal) (a, c, e) and perpendicular to it (b, d, f).

(a) Ti0.5ZrO_2 1000 °C/24 h longitudinal

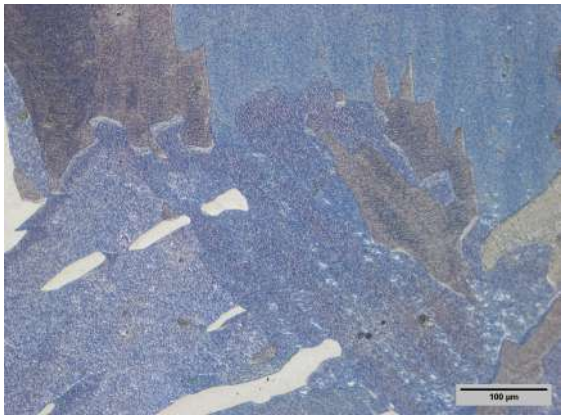

(b) Ti0.5ZrO_2 1000 °C/24 h perpendicular

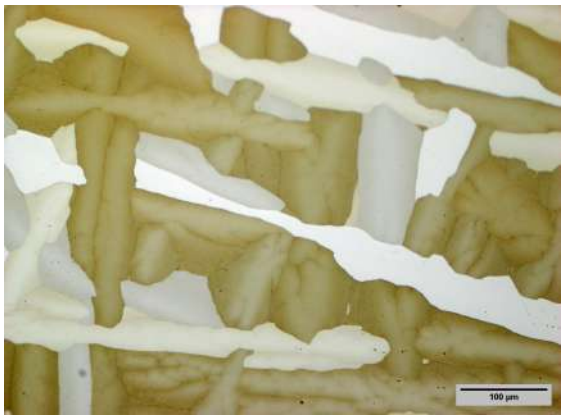

(c) Ti1ZrO_2 1000 °C/24 h longitudinal

(d) Ti1ZrO_2 1000 °C/24 h perpendicular

(e) Ti2ZrO_2 1000 °C/24 h longitudinal

(f) Ti2ZrO_2 1000 °C/24 h perpendicular

Figure 34: LOM images of the Ti$xZrO_2$ (x = 0.5, 1, 2 wt%) sample series after heat treatment (1000 °C for 24 h) in extrusion direction (longitudinal) (a, c, e) and perpendicular to it (b, d, f).

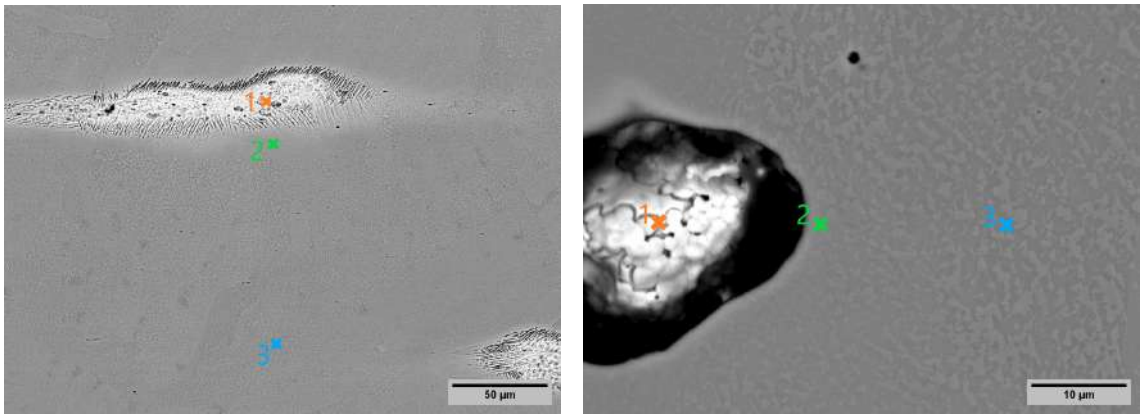

(a) Ti0.5ZrO_2 longitudinal

(b) Ti0.5ZrO_2 1000 °C/24 h longitudinal

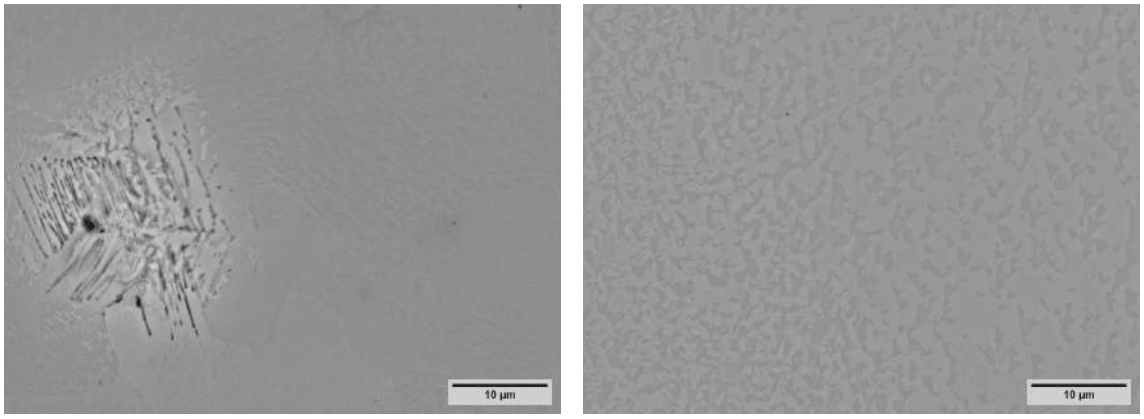

(c) Ti1ZrO_2 perpendicular

(d) Ti1ZrO_2 1000 °C/24 h perpendicular

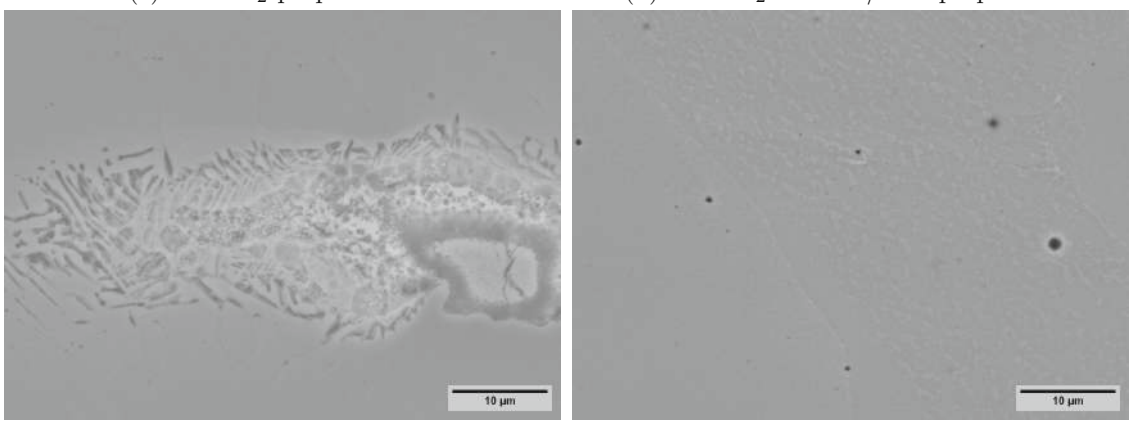

(e) Ti2ZrO_2 longitudinal

(f) Ti2ZrO_2 1000 °C/24 h perpendicular

Figure 35: SEM images of the as-extruded TixZrO_2 (x = 0.5, 1, 2 wt%) sample (a, c, e) and the heat-treated (1000 °C for 24 h) samples (b, d, f). The respective direction is specified at the sub-figure description. The measured points via EDX point analysis are marked in Figure a and b.

Figure 36 depicts the hardness HV10 results of the as-extruded and heat-treated samples. For reference an as-extruded pure Ti sample, provided by DI. Nico Moser [50], is added. The addition of 0.5 wt% ZrO_2 resulted in slight increase in hardness from 190 to 200 HV10. With increasing ZrO_2 content the hardness increases up to 283 HV10 in the as-extruded state. A heat treatment leads to an increase in hardness of about 10 HV10, despite the coarsening of the microstructure. This can be attributed to the higher ZrO_2 content homogeneously dissolved in the sample. Compared to the TixZr (x = 5, 10, 15 wt%) in Figure 20, the addition of 0.5 wt% ZrO_2, corresponding to a nominal Zr content of 0.37 wt%, results in the same hardness as the addition of 15 wt% Zr to Ti (Figure 20). Therefore, the increase in hardness in $TixZrO_2$ is additionally attributed to the effect of oxygen. The solid solution strengthening properties of oxygen are discussed in Chapter 2.3.4. The achieved results, regarding the addition of oxygen and the resulting hardness increase, are comparable to the literature [34].

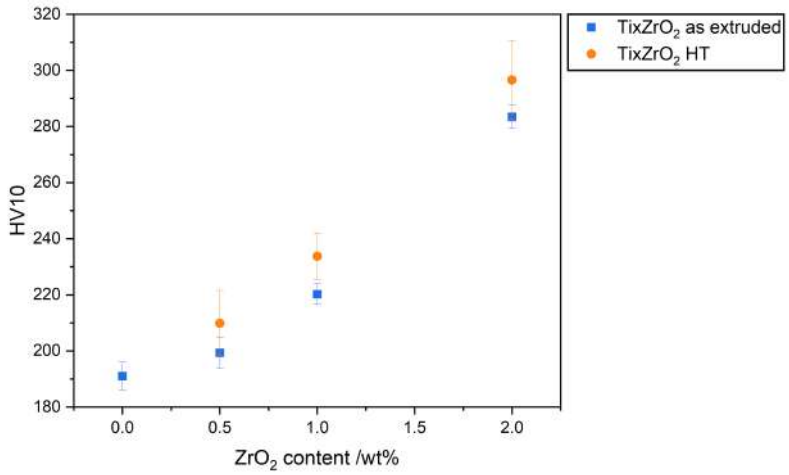

Figure 36: Hardness measurements HV10 of $TixZrO_2$ in the as-extruded and heat-treated (1000 °C for 24 h) state. For reference a pure Ti sample is added.

The XRD measurements of the $TixZrO_2$ sample series in the as-extruded and heat-treated state are shown in Figure 37. As observed under the SEM, α and β-titanium could be detected. Even though ZrO_2 particles were undissolved in the sample, no corresponding peaks could be detected. As the undissolved ZrO_2 particles are very localized, it is possible that there were no detectable ZrO_2 particles in the analysed region. Apart from α and β-titanium, no other phases or oxides could be detected, which indicates the successful incorporation of Zr and O in the titanium lattice due to their total solubility in Ti (Chapter 2.3.2, 2.3.4). Oh et al. [34] reported that increasing oxygen content leads to a slight decrease in the intensity of major peaks. This effect is attributed to the interstitial incorporation of oxygen in the Ti lattice, which causes a relaxation of the crystalline Ti alloys. This general trend can also be observed in the $TixZrO_2$ samples. The increasing Zr and O content in Ti matrix results in a slight leftward shift of the peaks.

The role of Zr as a substitutional element regarding the lattice parameter change was already discussed in Chapter 4.1. As oxygen functions as an interstitial element

an increase of the lattice parameter c should be observed. The increase in c/a ratio is attributed mainly to the solid solution of O [16]. An increase of the lattice parameter c with increasing ZrO_2 content can be observed, whereas the c/a ratio decreases slightly (Figure 38), contrary to the statements in the literature [12, 16]. It should also be noted that the values for parameter a in the heat-treated state are lower than those of the as-extruded samples. Higher values would be expected, as more ZrO_2 particles dissolved during the heat treatment. However, the observed lattice parameters a are lower than the value of pure Ti of 2.95 Å, making the results not credible.

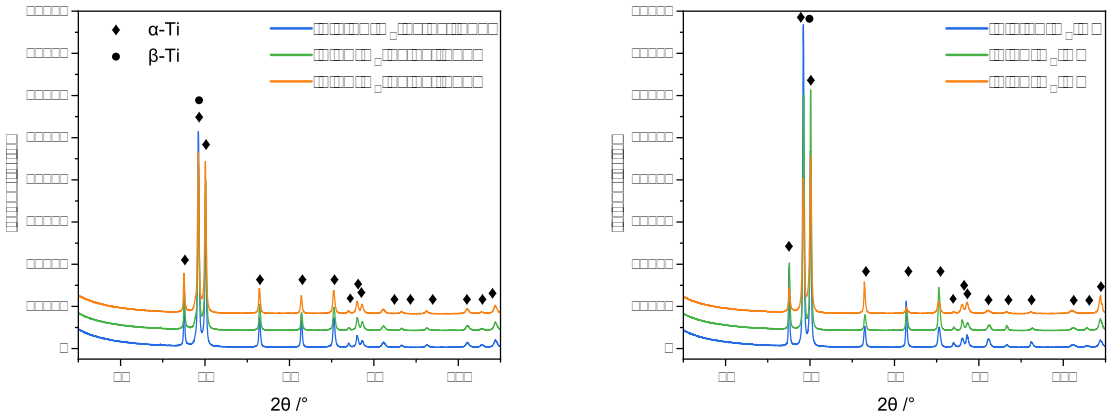

Figure 37: XRD measurements of the as-extruded and heat-treated $TixZrO_2$ sample series

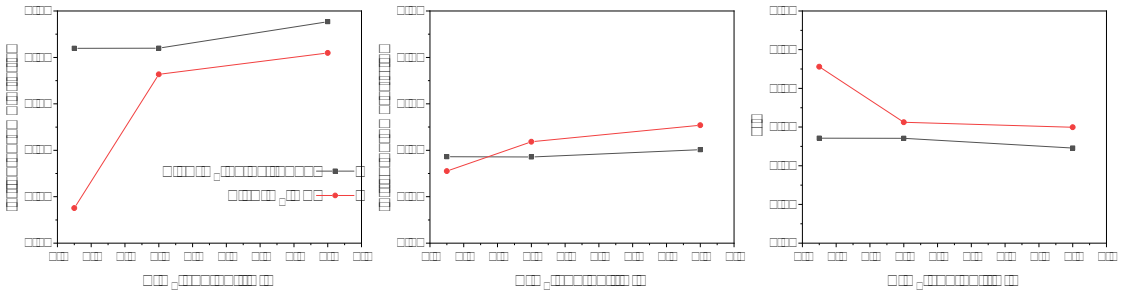

Figure 38: Lattice parameter a and c as well as the c/a ratio of the $TixZrO_2$ samples in the as-sintered and heat-treated state as a function of ZrO_2concentration.

4.4 Overview and Comparison of Ti-Zr Samples

In this chapter, the produced Ti-Zr samples are summarised and compared in terms of composition and manufacturing process to provide a good overview.

4.4.1 Density

The density values of the Ti-Zr alloys are summarized in Table 14. For a clearer overview, the manufacturing method and the calculated nominal Zr content, previously mentioned in Table 5, are also presented in the following table. It is to be noted that the TixZr sample series was not heat-treated as the microstructure was homogeneous after the production via arc furnace.

Sample, produced using the arc furnace (TixZr and Ti6.5CuxZr) or hot extrusion ($TixZrO_2$) show a high density above 99.2 % of theoretical density, except the heat-treated, optically dense sample Ti6.5Cu12Zr. These two manufacturing methods are suitable for sample production. The choice of manufacturing method depends on several considerations. The electric arc furnace is well-suited for small sample quantities, whereas hot extrusion can produce large sample rods. Another consideration is the starting material. Metal pellets are used in the electric arc furnace, while powders are used in hot extrusion.

The sintered sample series $TixZrH_2$ (both mixed and milled) exhibit lower densities in both the as-sintered and heat-treated states, achieving approximately 85% and 92% of the theoretical density, respectively. The low density is due to non-pressing in the mixed samples ($TixZrH_2$ with x = 3, 10 wt%) and insufficient pressing in the milled samples ($TixZrH_2$ with x = 3, 5, 10 wt%). The mixed $Ti5ZrH_2$ sample, which is the only successfully pressed sample, has a density of 95.88% of theoretical density after the heat treatment. However, this density is still lower than that of samples prepared by other methods. The pressing difficulties lie in the globular Ti powder, as seen in Figure 7a. The density in the mixed and milled $TixZrH_2$ sample series increased after the heat treatment due to the reduction of pores. To ensure a higher density in the sintered samples, a better pressing Ti powder can be used or pressing additives can be considered, however its easy removal has to be guaranteed.

Table 14: Overview of density results of produced Ti-Zr alloys, standard deviation of balance assumed to be 0.1 mg due to single weighing of entire sample. For summary the manufacturing process as well as the nominal Zr content is given.

			as-cast/sintered/extruded		heat-treated	
sample	manufacturing process	nominal Zr wt%	density g/cm^3	% theoretical density	density g/cm^3	% theoretical density
Ti5Zr	arc furnace		4.551	99.57	-	-
Ti10Zr			4.631	99.75	-	-
Ti15Zr			4.716	99.95	-	-
Ti6.5Cu3Zr	arc furnace		4.698	100.05	4.703	100.17
Ti6.5Cu5Zr			4.743	100.37	4.721	99.91
Ti6.5Cu8Zr			4.789	100.35	4.778	100.13
Ti6.5Cu10Zr			4.801	99.95	4.779	99.50
Ti6.5Cu12Zr			4.816	99.60	4.761	98.48
Ti6.5Cu15Zr			4.882	99.97	4.845	99.21
Ti3ZrH_2 mixed	vacuum sintering	2.94	4.120	91.01	4.201	92.81
Ti5ZrH_2 mixed		4.89	4.218	92.81	4.357	95.88
Ti10ZrH_2 mixed		9.79	4.114	89.63	4.142	90.23
Ti3ZrH_2 milled	vacuum sintering	2.94	4.065	89.79	4.138	91.41
Ti5ZrH_2 milled		4.89	3.619	79.64	4.181	91.99
Ti10ZrH_2 milled		9.79	4.042	88.06	4.283	93.32
Ti0.5ZrO_2	extrusion	0.37	4.528	100.52	4.497	99.83
Ti1ZrO_2		0.74	4.498	99.75	4.486	99.49
Ti2ZrO_2		1.48	4.530	100.24	4.494	99.45

4.4.2 Microstructure

The microstructure differs depending on the composition and the production method, as well as the subsequent heat treatment.

The α/β microstructure of the TixZr samples changes with the addition of 6.5 wt% Cu to a triangular structure of needle-like α/β laths, which could potentially be identified as martensite. The fast cooling rate in the arc furnace is beneficial for the formation of very fine α/β laths or martensite. The eutectoid transformation of α-Ti and Ti_2Cu can mainly be observed after the heat treatment due to the slow furnace cooling.

The use of ZrH_2 as the zirconium source and the production using sintering results in a equiaxed microstructure After heat treatment and water quenching into laths with inhomogeneous Zr content (mixed sample series) or a bi-modal microstructure with equiaxed α grains and α/β lath colonies, when a higher Zr concentration is guaranteed (milled sample series). Water quenching ensures a more homogeneous distribution of Zr and prevents its agglomeration at grain boundaries, which occurred after sintering and the subsequent slow furnace cooling. An element partitioning effect could be observed in the bi-modal microstructure. Zr partitioned into the lath colonies, formed from prior β grains, indicating a weak β stabilizing effect of Zr.

The microstructure of the hot extruded TixZrO_2 samples consists of laths, which

coarsen after the heat treatment. The deformation direction (longitudinal or perpendicular to the extrusion direction) does not influence the microstructure. The ZrO_2 particles did not dissolve completely and homogeneously after the hot extrusion, hence a heat treatment was necessary. The heat treatment at 1000 °C for 24 h was insufficient to dissolve all particles, nevertheless an increase in Zr content was observed. Longer heat treatments would be necessary to dissolve the ZrO_2 particles completely.

In general, grain refinement can be observed with increasing Zr content throughout a sample series. As the $TixZrO_2$ samples have the lowest Zr content, the laths are noticeably coarser in both as-extruded and heat-treated state (Figure 33 and 34), compared to the other samples with the lowest Zr content like Ti5Zr (Figure 14a) and $Ti3ZrH_2$ (Figure 24a and 28a).

Slow cooling rates result in a fully equiaxed or coarse lamellar microstructure, whereas fast cooling rates achieved in the arc furnace or with water quenching produce a very fine α/β martensite-like or bi-modal microstructure.

4.4.3 Hardness

For a better comparison, all results of the HV10 hardness measurements are presented as a function of Zr content in Figure 39. It is to be noted that the Zr content of the $TixZrO_2$ sample series is given as the nominal Zr value (Table 5, 14), whereas in Figure 36 the results were presented based on ZrO_2 content.

The analysed samples series were TixZr, Ti6.5CuxZr and $TixZrO_2$, the latter two also in the heat-treated state. $TixZrH_2$ could not be measured, as the high porosity would lead to implausible results. The hardness values of the samples as-cast Ti6.5Cu and as-extruded Ti were provided by my colleagues, Dipl.-Ing. Ella Staufer and Dipl.-Ing. Nico Moser, respectively.

Compared to the hardness of as-extruded Ti of 191 HV10, the addition of 5 wt% Zr leads to an initial decrease in hardness to 156 HV10 as seen as-cast sample Ti5Zr. To achieve the hardness of pure Ti, an addition of 15 wt% Zr is required. It is important to note that the two samples were produced using different processes, namely extrusion and arc melting. Nevertheless, an interesting comparison can be observed, as similar results are found in the Ti6.5Cu sample series. A reduction in hardness with the addition of Zr is also noted in the Ti6.5Cu series. In this case, a Zr content of 12 wt% is necessary to reach the hardness of Ti6.5Cu (320 HV10). The initial decrease in hardness after the addition of Zr indicates higher ductility.

The hardness increase with higher Zr content is steeper for the $TixZrO_2$ sample series compared to the other sample series. This is attributed to the more pronounced hardening effect of oxygen, as compared to zirconium.

The hardness of the sample series Ti6.5CuxZr decreases after the heat treatment due to grain coarsening. In the sample series $TixZrO_2$ the opposite effect can be observed. In the as-cast samples undissolved ZrO_2 particles are visible, resulting in lower and inhomogeneous Zr and O concentration in the sample. Due to the heat treatment, the particles dissolved, leading to a higher Zr content in the matrix. An increase in O content is also expected; however, this remains to be confirmed by

further measurements. Consequently, higher HV10 results were measured, despite the grain coarsening during heat treatment.

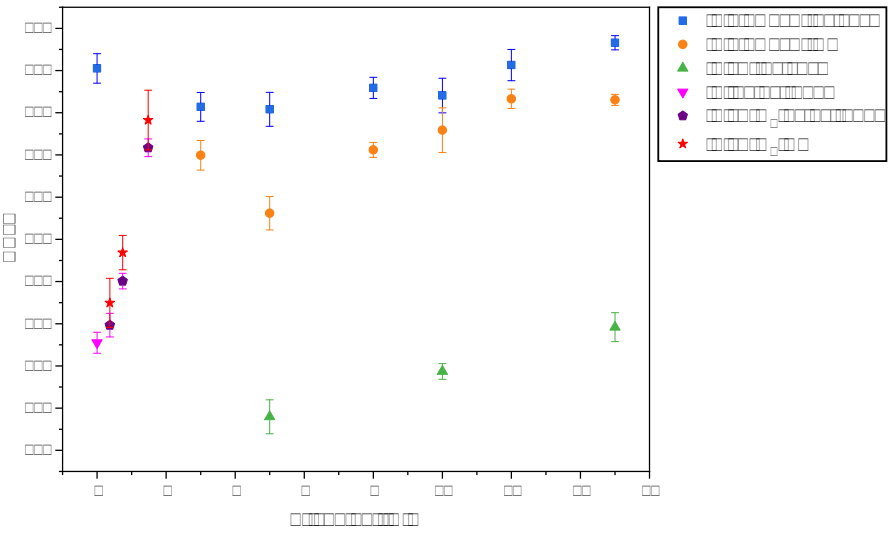

Figure 39: Overview of hardness measurements HV10 of TixZr (as-cast), Ti6.5CuxZr (as-cast and heat-treated) and $TixZrO_2$ (as-extruded and heat-treated). For reference the hardness HV10 of as-cast Ti6.5Cu and as-extruded Ti are added, provided by my colleagues, Dipl.-Ing. Ella Staufer and Dipl.-Ing. Nico Moser, respectively.

4.4.4 X-Ray diffractometry

The XRD measurements detected α and β-Ti, as well as Ti_2Cu in the sample series Ti6.5CuxZr. These results align with the SEM analysis. It should be noted that the eutectoid phase Ti_2Cu was detected via XRD in the as-cast samples, even though its size was not resolvable with SEM.

In the $TixZrH_2$ sample series, no ZrH_2 or TiH_2 was detected after sintering, indicating successful dehydration of the samples.

Figure 40 summarizes the lattice parameter a and c as well as the c/a ratio of all produced Ti-Zr alloys. The sample series $TixZrH_2$ and $TixZrO_2$ are depicted as a function of nominal Zr content rather than ZrH_2/ ZrO_2 content for better comparison.

The substitutionally incorporation of Zr in the Ti lattice leads to an increase in the lattice parameter a and c of the α-Ti, which results in a leftward shift of the peaks in XRD measurements. The expansion of the α-Ti lattice increases with increasing Zr content. This effect can be observed in all sample series. The c/a ratio remains nearly constant at 1.58. The lattice parameter c of the sample series $TixZrO_2$ exhibits a steeper increase due to additional incorporation of oxygen as an interstitial element. As already mentioned, the values for lattice parameter a of the heat-treated samples is lower than than the 2.95 Å value of pure Ti, making the results not credible. Therefore, the decrease of c/a ratio, which is contrary to the literature [16], is not necessarily correct.

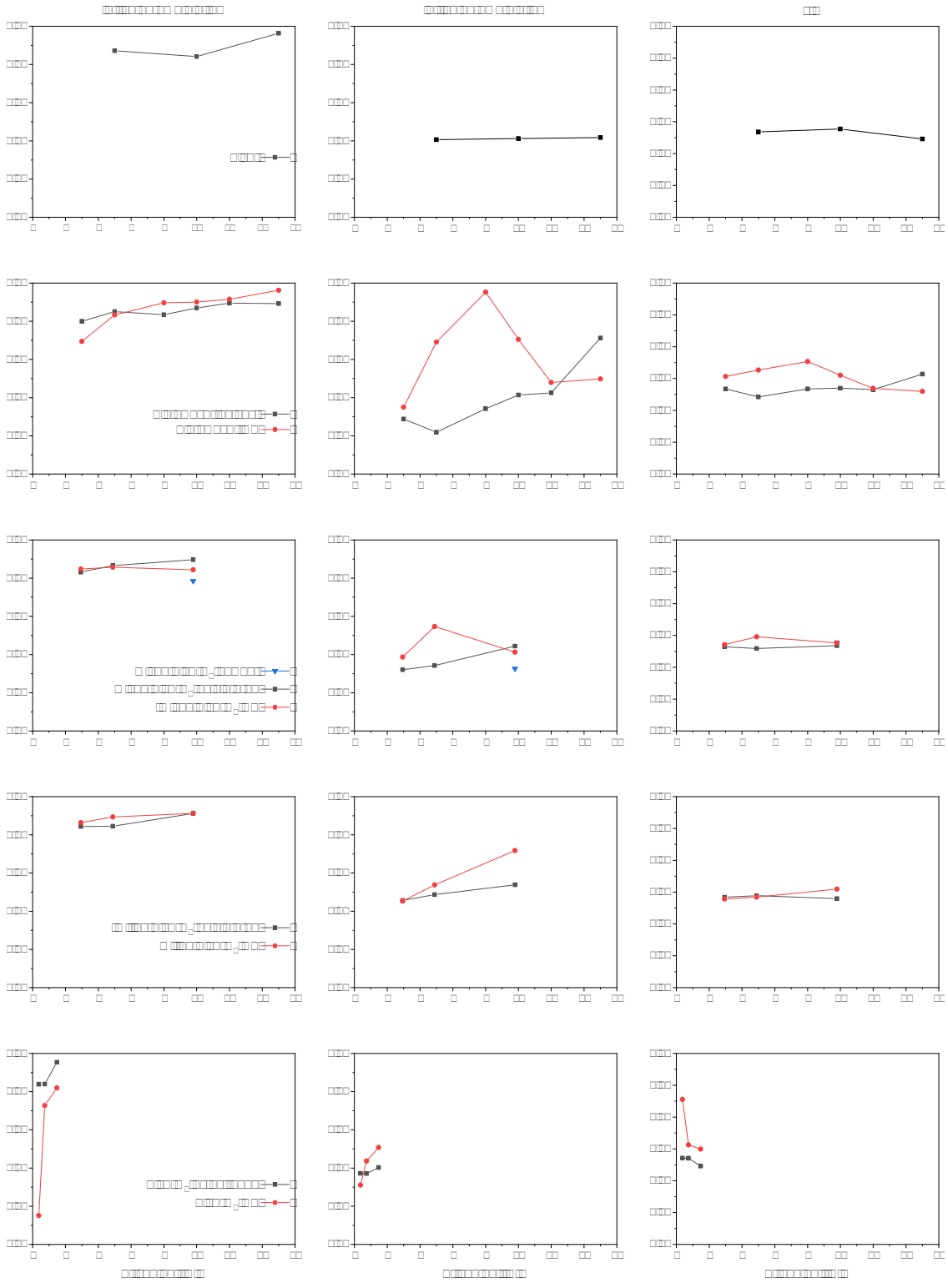

Figure 40: Lattice parameters a and c as well as the c/a ratio of all Ti-Zr samples. The nominal Zr content of $TixZrH_2$ and $TixZrO_2$ samples is used too ensure a better comparability. The scaling of the graphs is uniform also for better comparability.

4.5 Ti5.9Cu2Fe2Al

4.5.1 Cast material

The expected phases in the cast material Ti5.9Cu2Fe2Al were calculated using ThermoCalc and are depicted in Figure 41. In addition to the α and β phases, the eutectoid phase Ti_2Cu forms at temperatures below 800 °C. The Ti_3Cu phase is stable only at low temperatures below approximately 280 °C.

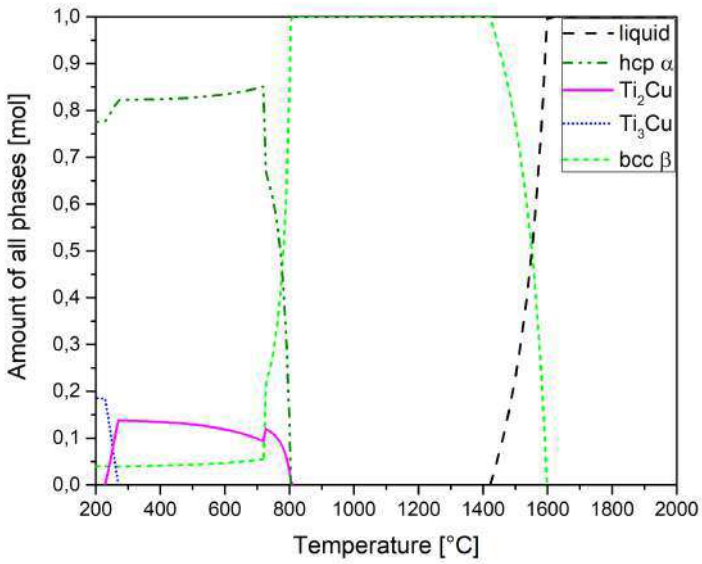

Figure 41: Calculated phase diagram for Ti5.9Cu2Fe2Al by Martin Klein from LKR (ThermoCalc)

Since the cast material was produced by an external company (GfE) and the exact production conditions are unknown, the analysis of microstructure, phase composition, and homogeneity was especially important.

The microstructure of the cast material shows equiaxed grains with Widmanstätten laths (Figure 42a and b). The α/β microstructure remains constant throughout the cross section, except for a few inhomogeneous regions, as seen in Figure 42c. EDX point analysis shows that the brighter phase at points 1 and 2 exhibits a copper content of up to 37 wt% and an iron content of only 1 wt%. At point 3, a copper content of 10 wt% was measured. This indicates copper enrichment both within the phase and its surroundings. As the cast material was produced by an external company, the specifics of the process and potential errors in the homogenization process could not be identified. Due to this uncertainty, other inhomogeneous areas may also be expected.

(a) Ti5.9Cu2Fe2Al

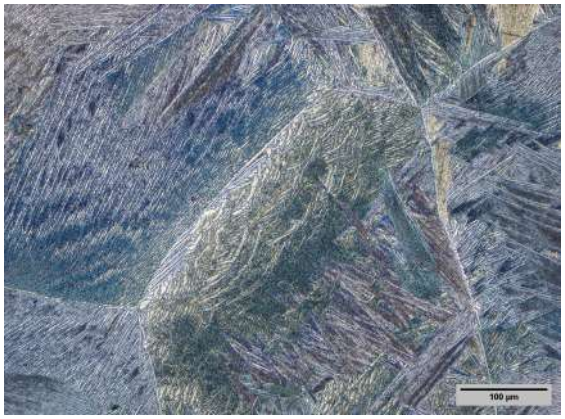

(b) Ti5.9Cu2Fe2Al - detail

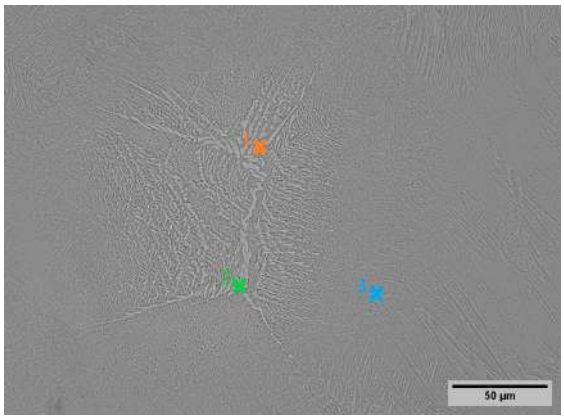

(c) Ti5.9Cu2Fe2Al - enrichment of copper

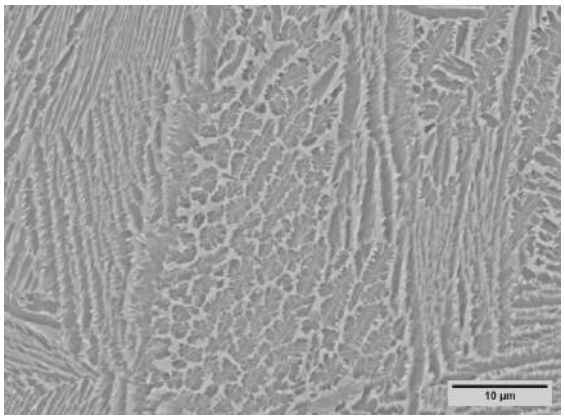

(d) Ti5.9Cu2Fe2Al - detail

Figure 42: LOM (a, b) and SEM (c, d) images of the cast material Ti5.9Cu2Fe2Al in as-cast state. The measured points via EDX point analysis are marked in Figure c.

Figure 43 illustrates the XRD measurement of the casting material. In addition to the anticipated α-Ti, β-Ti, and the eutectoid phase Ti_2Cu, CuO could also be identified. Despite the unusual nature of this phase, its occurrence is consistent with the presence of other observed inhomogeneities. A peak at 57° could not be identified clearly. A possible identification could be an intermetallic β-titanium. In this region, two β-titanium phases, $Ti_{0.97}Fe_{0.36}Al_{2.67}$ and $Cu_{0.5}TiAl_{2.5}$, display a peak. Their most significant peak aligns with the Ti_2Cu peak at 39.5°.

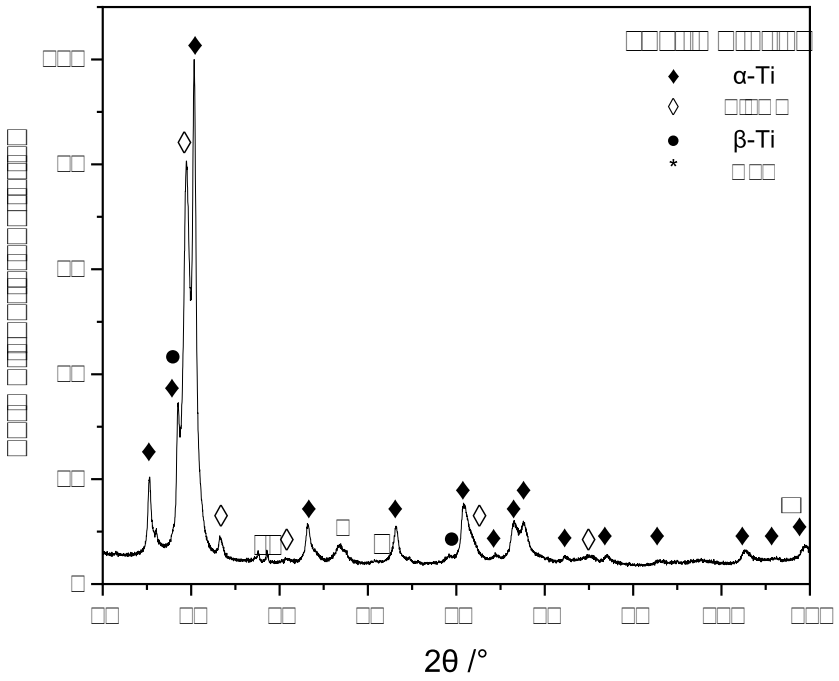

Figure 43: XRD measurement of the casting material Ti5.9Cu2Fe2Al in as-cast state

4.5.2 Hot Extrusion

The cast material Ti5.9Cu2Fe2Al underwent hot extrusion twice, producing rods of varying diameters. The rod with a diameter of 8 mm was preheated at 1100 °C, while the rod with a diameter of 4 mm was preheated at 1200 °C. To analyse the homogeneity of the hot-extruded rod regarding the composition and the microstructure, three samples were taken from the rear, middle and front of the rod, as indicated in Figure 9. These three sections were analysed in the extrusion direction (longitudinal) and also perpendicular to it.

Figure 44 depicts the LOM images of the as-extruded rod with a diameter of 8 mm. The microstructure contains equiaxed grains with fine laths. The α/β laths form a triangular structure which may indicate the presence of martensite (Figure 46a, c and e).

For the alloy Ti5.9Cu2Fe2Al a M_s temperature of 536 °C (using $Mo^B_{eq.}$) or 601 °C (using $Mo^B_{eq.}$) was calculated (Equation 1). In both cases, the temperature during extrusion should have exceeded the M_s temperature, allowing martensite to form. However, the slow cooling after extrusion would not promote the formation of this

phase. To determine the formation of martensite for certain, further analysis via TEM would be necessary.

Coarse inclusions and inhomogeneities can also be observed (Figure 44a, d and c). Figure 44a and d depict an enrichment of titanium, which can also be identified under the SEM. EDX point analysis of points 1 and 2, as marked in Figure 46c, measured a composition of 1.7 wt% aluminium and less than 1 wt% of iron and copper. Therefore, the titanium content is approximately 97 wt%.

Besides the regions depleted of alloying elements, another coarser phase is also present, extending in the extrusion direction, as seen in Figure 44e and 46e.EDX point analysis at locations 1 and 2, as indicated in Figure 46e, reveals that the phase contains an elevated copper concentration of up to 10 wt%, with other alloying elements present at approximately 2 wt%. The copper concentration decreases at point 3 to 7.2 wt%.

To ensure a more homogeneous composition in the samples, a heat treatment at 1000 °C for 24 h was conducted. While the majority of inclusions and copper-rich phases dissolved, a few could still be observed. For example, Figure 45c depicts regions depleted of alloying elements. As in the as-extruded state, the microstructure remains the same regardless of the position in the rod and the direction.

After slow cooling from the β-region, the microstructure exhibited a coarser basketweave structure of Widmanstätten plates (Figure 45). Compared to the as-extruded samples, equiaxed grains are not observed. During the heat treatment, the microstructure coarsens and develops a α/β structure with precipitations of intermetallic particles at the α/β interface, such as the eutectoid phase Ti_2Cu (Figure 46b, d and f). The eutectoid transformation is favoured by the slow furnace cooling.

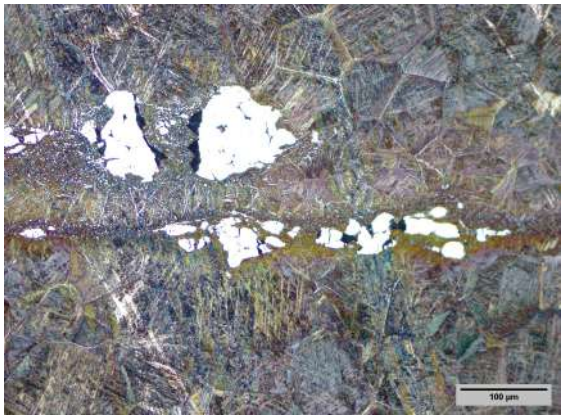

(a) rear longitudinal - 8 mm rod

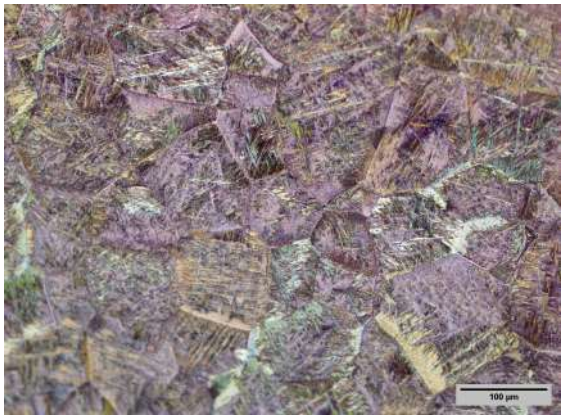

(b) rear perpendicular - 8 mm rod

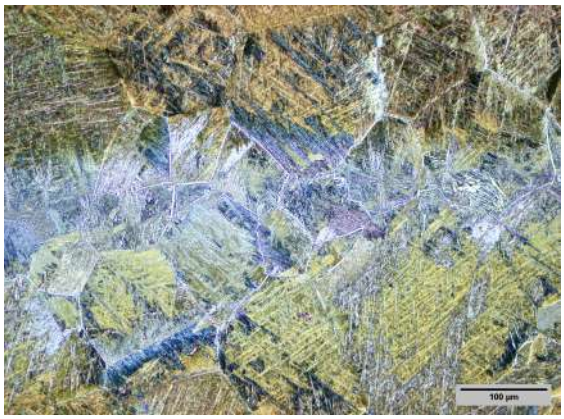

(c) middle longitudinal - 8 mm rod

(d) middle perpendicular - 8 mm rod

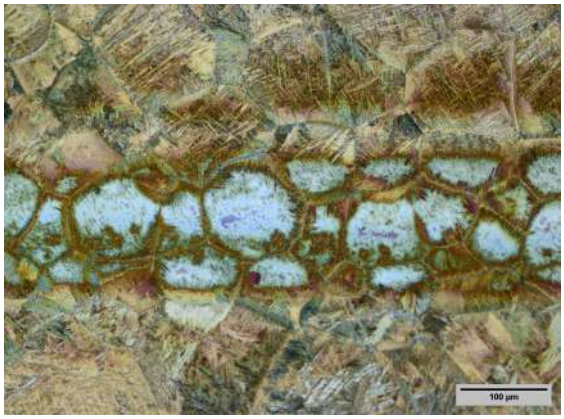

(e) front longitudinal - 8 mm rod

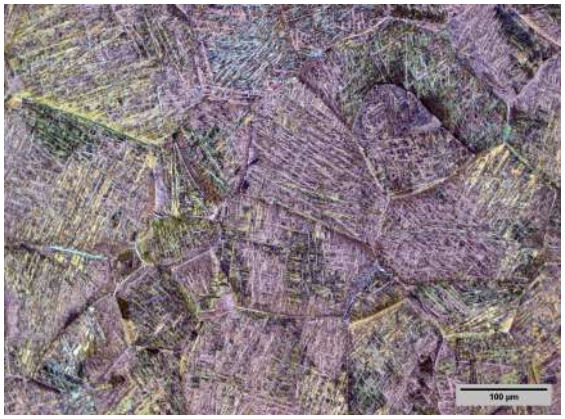

(f) front perpendicular - 8 mm rod

Figure 44: LOM images of the hot-extruded Ti5.9Cu2Fe2Al rod with 8 mm diameter

(a) rear longitudinal - 8 mm rod - HT

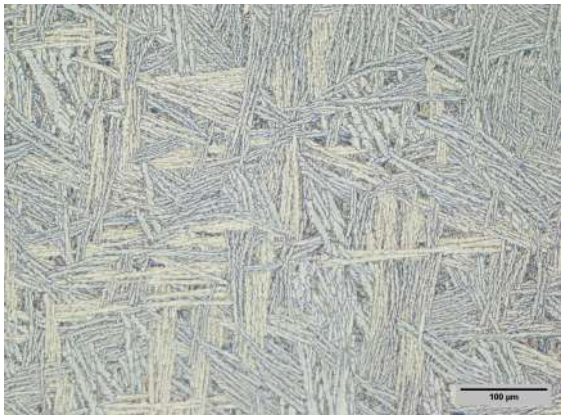

(b) rear perpendicular - 8 mm rod - HT

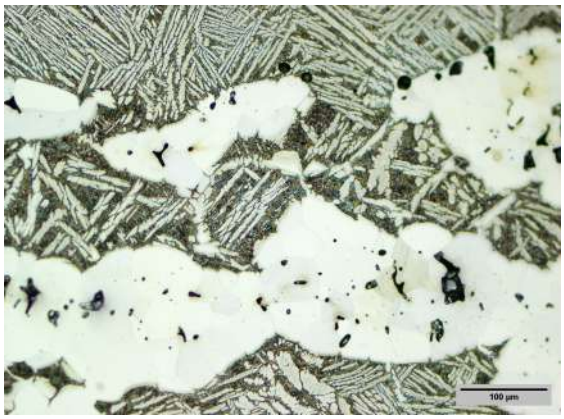

(c) middle longitudinal - 8 mm rod - HT

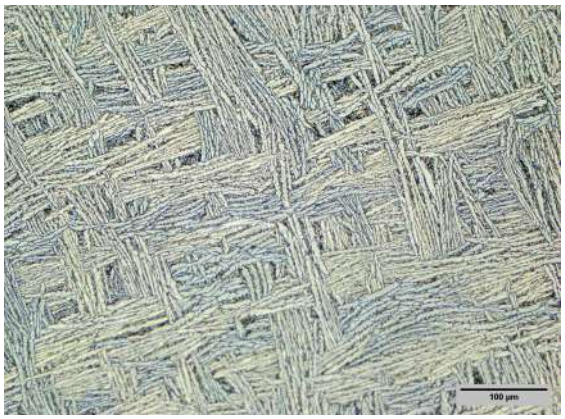

(d) middle perpendicular - 8 mm rod - HT

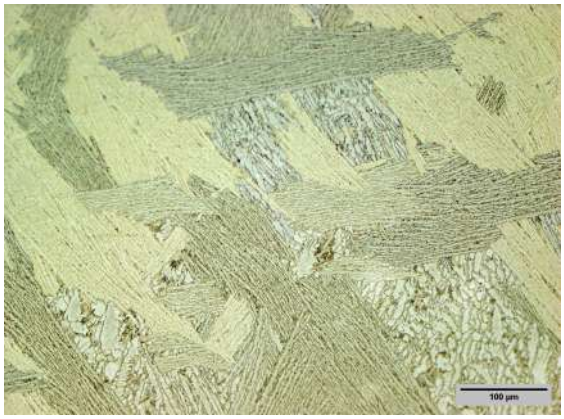

(e) front longitudinal - 8 mm rod - HT

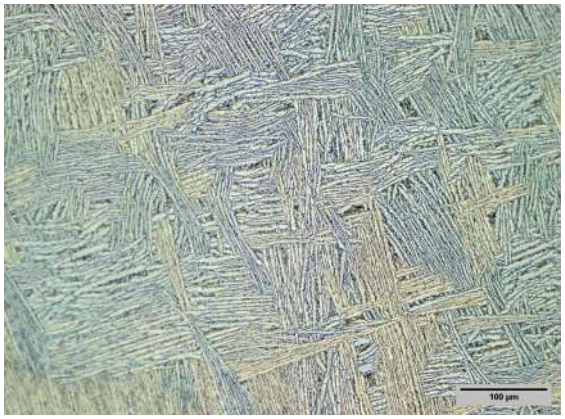

(f) front perpendicular - 8 mm rod - HT

Figure 45: LOM images of heat-treated (1000 °C for 24 h) Ti5.9Cu2Fe2Al samples after hot extrusion resulting in 8 mm diameter rods

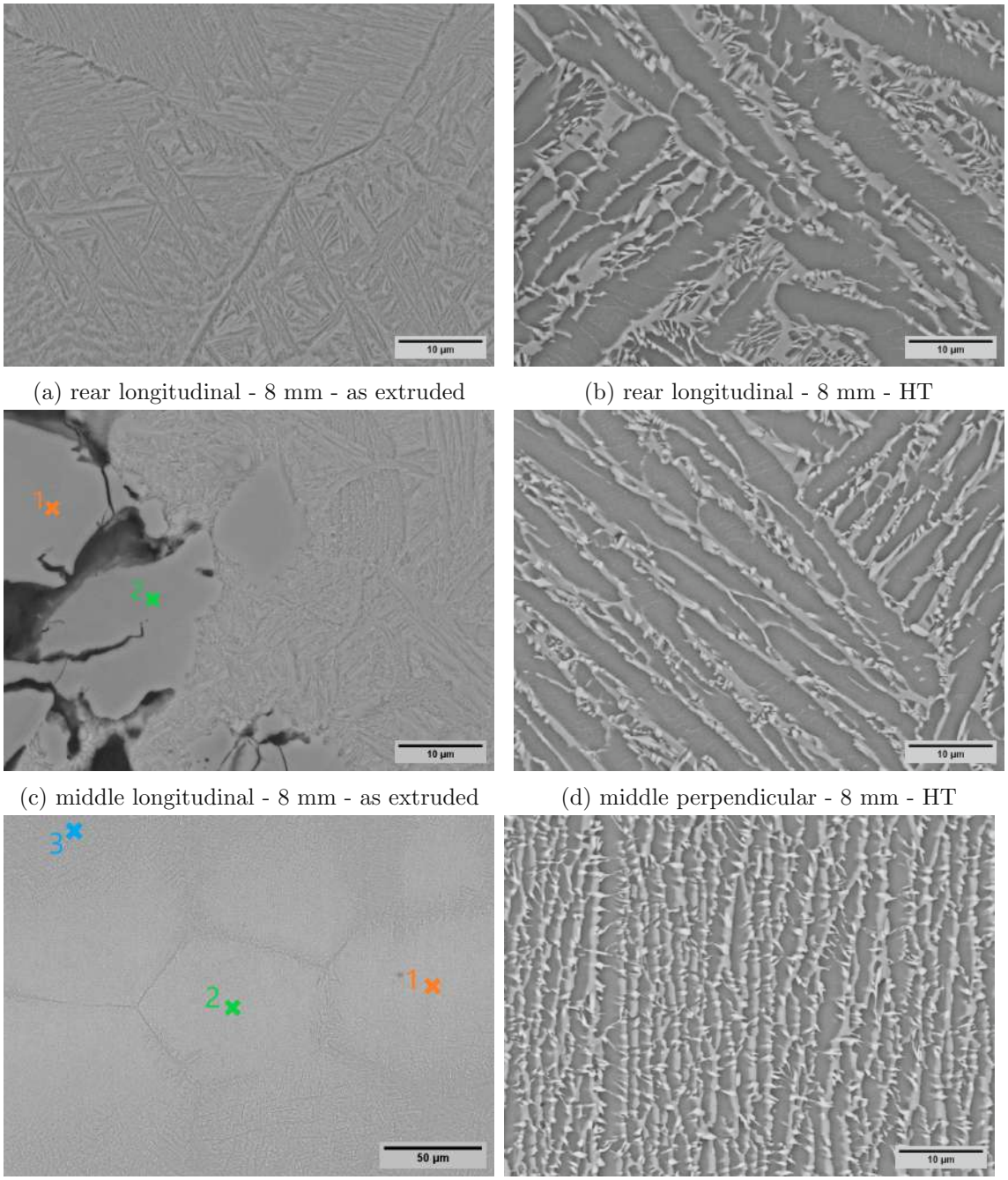

(a) rear longitudinal - 8 mm - as extruded

(b) rear longitudinal - 8 mm - HT

(c) middle longitudinal - 8 mm - as extruded

(d) middle perpendicular - 8 mm - HT

(e) front longitudinal - 8 mm - as extruded

(f) front perpendicular - 8 mm - HT

Figure 46: SEM images of the sample series Ti5.9Cu2Fe2Al with a diameter of 8 mm in the as-extruded (a, c, e) and heat-treated (1000 °C for 24 h) state (b, d, f). Since the microstructure is independent of the direction, it is not differentiated in this summary and the corresponding direction is specified in the subfigure description.

Figure 47 depicts the hardness measurements HV10 of all samples taken from the 8 mm extrusion rod. It is evident that despite the slight differences in hardness, the direction (longitudinal or perpendicular) and position (rear, middle or front) of the sample do not have a significant influence on the hardness. This result corresponds to the observations under LOM and SEM, that the microstructure is independent of the direction and position. The average hardness of the as-extruded samples is 327 HV10. After heat treatment, the hardness decreases on average to 307 HV10. While the heat treatment homogenized the sample, it also caused microstructural coarsening, resulting in a slight decrease in hardness.

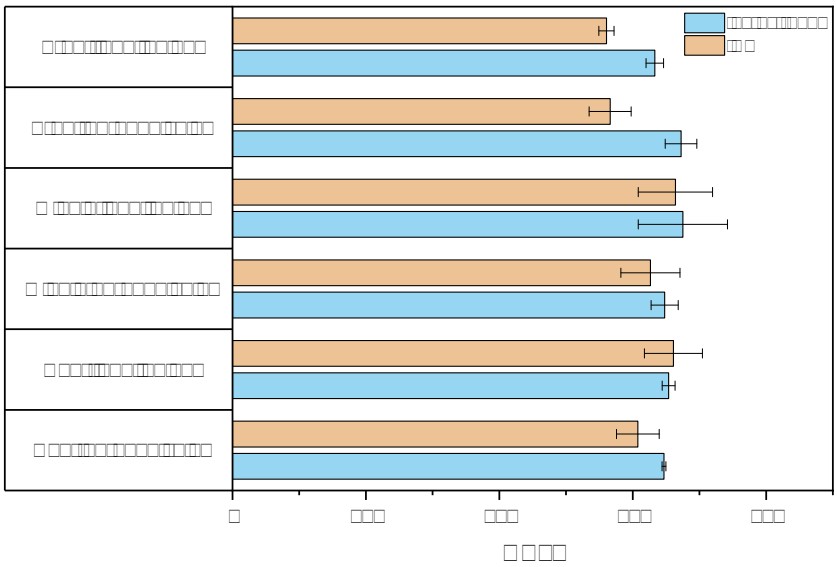

Figure 47: Hardness measurements HV10 of Ti5.9Cu2Fe2Al hot extruded rod with a diameter of 8 mm in the as-extruded and heat-treated (1000 °C for 24 h) state. Comparison of the results regarding the position and direction of the samples.

The hot extrusion samples with a resulting 4 mm diameter exhibits equiaxed grains with fine laths (Figure 48). The microstructure and grain size are similar to the 8 mm rod samples. The microstructure exhibits fine α laths with Widmanstätten features at grain boundaries (Figure 49). The fine α/β-laths form a triangular structure, as observed in the 8 mm rod (Figure 46a, c and e). As mentioned, the microstructure suggests the formation of martensite; however, further analysis is required to conclusively verify this.

There are defects, such as regions depleted of alloying elements (Figure 48b), similar to those found in the 8 mm rod (Figure 44a, d and Figure 45c). However, these samples exhibit fewer defects. This could be due to the higher force during the extrusion, which may lead to the dissolution of inclusions or better distribution of defects in the direction of extrusion. However, there are no reaction zones indicating dissolution. Alternatively, the sample of the cast material used for this extrusion experiment was more homogeneous. The improved homogeneity of the 4 mm diameter samples precluded the necessity for subsequent heat treatment as applied to the 8 mm rod.

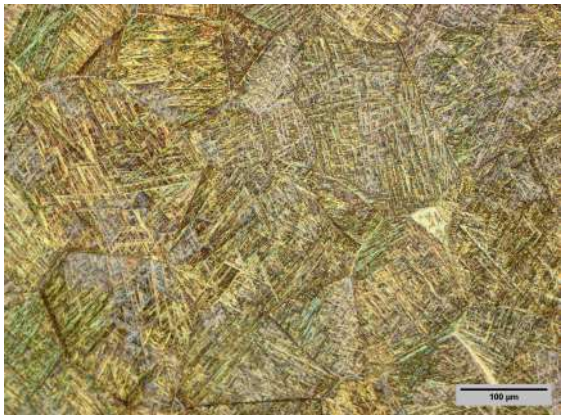

(a) rear longitudinal - 4 mm

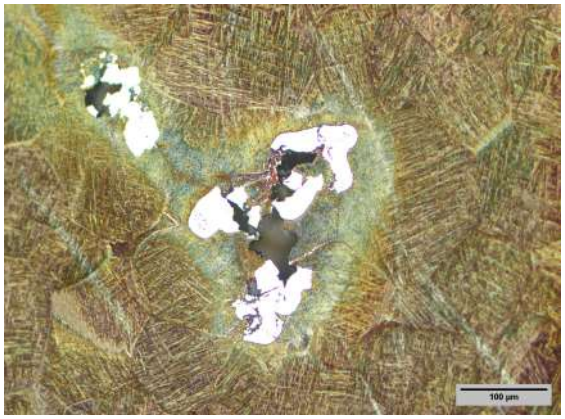

(b) rear perpendicular - 4 mm

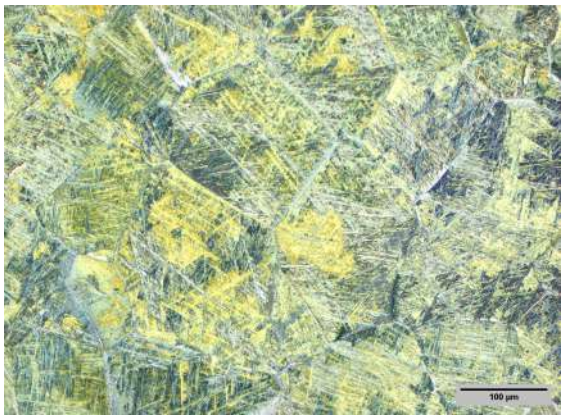

(c) middle longitudinal - 4 mm

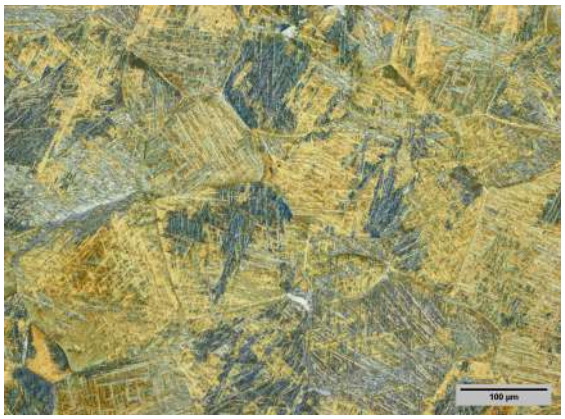

(d) middle perpendicular - 4 mm

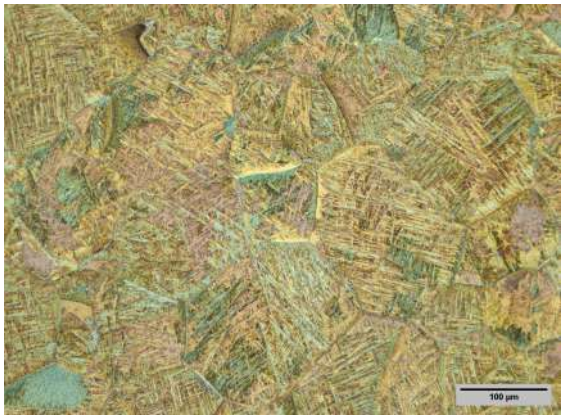

(e) front longitudinal - 4 mm

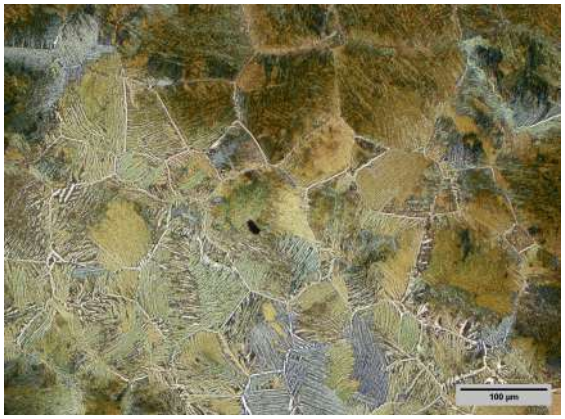

(f) front perpendicular - 4 mm

Figure 48: LOM images of the as-extruded Ti5.9Cu2Fe2Al rod with a 4 mm diameter

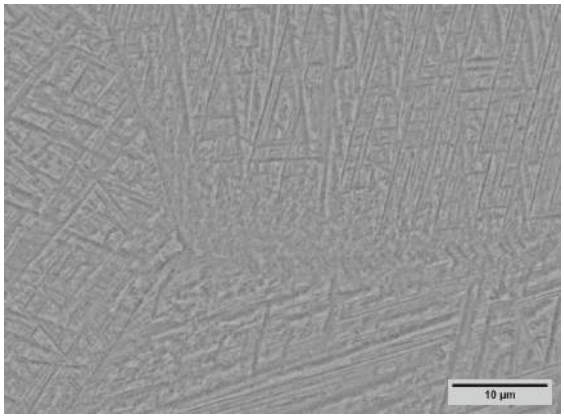

(a) rear longitudinal - 4 mm

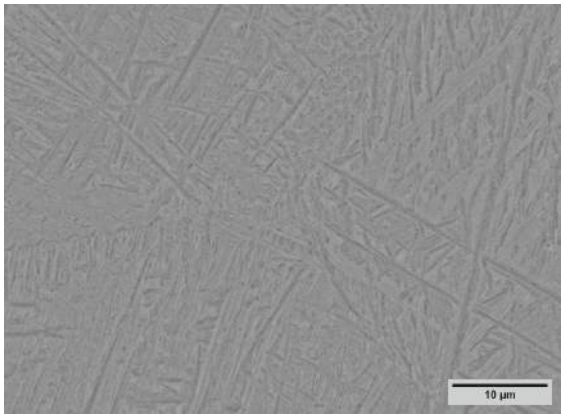

(b) middle longitudinal - 4 mm

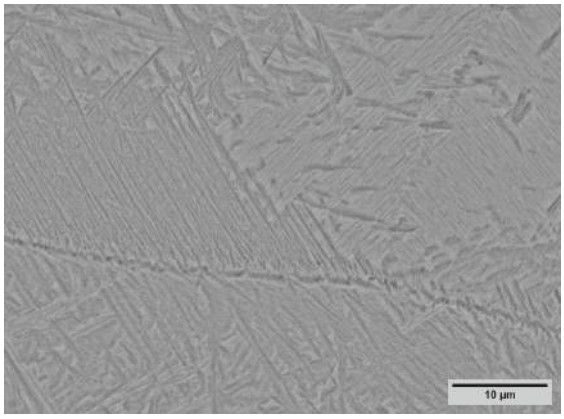

(c) front longitudinal - 4 mm

Figure 49: SEM images of the as-extruded Ti5.9Cu2Fe2Al rod with a 4 mm diameter. Since the microstructure is independent of the direction, it is not differentiated in this summary and the corresponding direction is specified in the subfigure description.

Figure 50 illustrates the hardness measurement results for the 4 mm samples, along with an overview of all hot extruded samples, including the cast material. The three samples taken from the extruded rod with a diameter of 4 mm exhibit the same properties regarding the hardness. Neither the direction nor the position of the sample significantly influence the hardness of HV10, as was also evident in the 8 mm samples (Figure 47). The average hardness is 344 HV10, thus slightly higher than that of the 8 mm samples (327 HV10). The homogeneity of the 4 mm samples may be the cause of this slight difference. The hardness of the original cast material is 300 HV10, similar to that of the heat-treated samples (307 HV10). After heat treatment, the microstructure coarsens and therefore the hardness decreases.

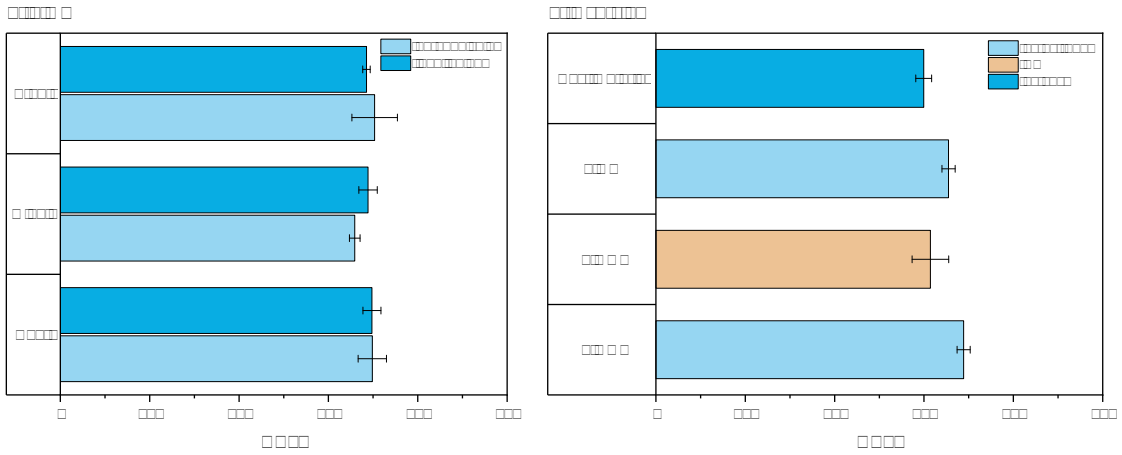

Figure 50: Hardness measurements of as-extruded Ti5.9Cu2Fe2Al samples with 4 mm diameter (a). Overview and comparison of the hardness measurements HV10 of all Ti5.9Cu2Fe2Al samples (b).

Figure 51 depicts the XRD measurements of all Ti5.9Cu2Fe2Al samples in as-extruded and heat-treated condition. In addition to α and β-Ti, an intermetallic phase Ti_2Cu was quantified. In the as-extruded samples, the eutectoid phase was detected despite its absence in SEM observations (Figure 46 and 49).This may be attributed to the intermetallic Ti_2Cu phase being below the resolution limit of SEM. Consequently, heat treatment followed by slow cooling is necessary to promote its growth to a resolvable size.

The XRD analysis of the 8 mm extrusion sample exhibits a minor peak at 47.9°, which can be explained with the presence of iron. It is possible that the sample edges are coated with iron due to wear of the die and punch, suggesting that this peak may be attributed to the coating. Except of this peak, the diffractograms of the as-extruded and heat-treated samples are identical.

The peak at 57.7°, previously noted in the context of the cast material in Figure 43, can be attributed to an intermetallic β-titanium phase, such as Ti0.97Fe0.36Al2.67 or $Cu0.5TiAl_{2.5}$. As their most significant peak aligns with the Ti_2Cu peak at 39.5° a clear identification is not possible.

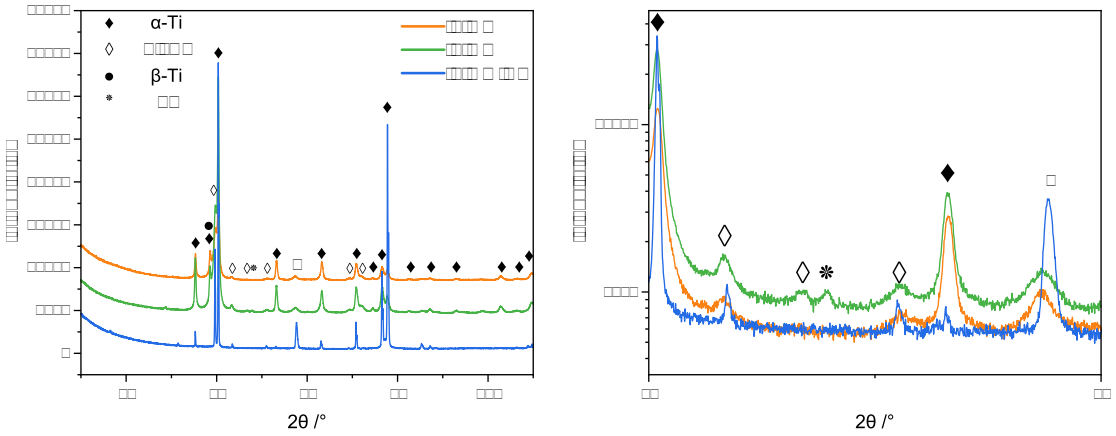

Figure 51: XRD measurements of the hot-extruded samples with a diameter of 8 mm and 4 mm. The 8 mm rod was measured in the as-extruded and heat-treated (1000 °C for 24 h) state. An overview as well as an inset is depicted.

4.5.3 Deformation behaviour by Caliber rolling

To determine the influence of caliber rolling on the microstructure, the samples were investigated in the rolling direction (longitudinal) as well as perpendicular to it. In Figures 52 - 59 two samples series with different preheating temperatures (800 °C and 1000 °C) are depicted in the respective direction.

The samples preheated at 800 °C, taken from the 2nd and 4th caliber, show a similar microstructure in the longitudinal and perpendicular direction (Figures 52a, b and 53a, b). This suggests that, up to this point, the rolling process has not significantly influenced the microstructure. Especially the microstructure of the sample after the second caliber, depicted in Figure 52a and 53a, exhibits a microstructure of equiaxed grains, similar to the cast material (Figure 42).

From the 6th caliber onwards, an elongation in the rolling direction is visible (Figure 52c). The elongation in the rolling direction is becoming increasingly prominent with each deformation step. It indicates that no dynamic recrystallisation took place.

The calculated phase diagram of Ti5.9Cu2Fe2Al shows a melting temperature of 1600 °C (Figure 41). According to the rule of thumb that the recrystallisation temperature is 40 to 50% of the melting temperature, the recrystallisation temperature of the material Ti5.9Cu2Fe2Al should be between 640 and 800 °C. Therefore, it is possible that the temperature of the sample dropped below the recrystallisation temperature before the caliber rolling, hindering recrystallization. This is especially likely in the later rolling steps, as the samples became progressively thinner, cooling more rapidly.

Figures 54 and 55 depict the α/β microstructure observed under the SEM. This microstructure forms in all samples, however after the 6th caliber intermetallic phases, most likely the eutectoid phase Ti_2Cu, precipitate. Due to the small size, no reliable point analysis could be conducted.

In comparison, the sample series at 1000 °C shows no indication of an elongation. The equiaxed microstructure appears identical in both the longitudinal and perpendicular directions (Figure 56 and 57). Furthermore, initial grain coarsening can be observed compared to the cast material and the samples preheated at 800 °C. During the rolling steps, the grain size remains approximately the same. The absence of elongation in the rolling direction and grain coarsening indicates dynamic recrystallisation. The preheating temperature of 1000 °C, which exceeds the α/β transus temperature, enables dynamic recrystallisation as discussed in Chapter 2.4.

Within a grain, bright areas without a visible microstructure can be observed. The bright areas progressively decrease with every rolling step until they are no longer observable. EDX point analyses show an increase of copper up to 9 wt% in these areas, indicating retained β phase, as the preheating temperature exceeds the α/β transus temperature. A slight difference in microhardness HV0.1 can also be observed. The bright copper-rich areas exhibit a microhardness of 448 ± 14 HV0.1, while the α/β microstructure has a hardness of 374 ± 19 HV0.1.

Needle-like laths can be observed extending into the bright areas from the grain boundaries, as exemplified in Figure 57a and b. The needle-like α-Ti laths can also be observed in Figure 58 and 59. The fine laths either extend into the structureless regions, as seen in Figure 56a, or form a triangular structure, as shown in Figure 56c. Even though the prior β grains undergo coarsening during rolling, the very fine α/β substructure becomes refined by each rolling step. In the last sample, which is depicted in Figure 56e and 57e, it is not possible to resolve the microstructure under the available SEM. Because of the needle-like and triangular structure, the microstructure could also be identified as martensite. The martensite starting temperature M_s of Ti5.9Cu2Fe2Al is 536 °C or 601 °C (Equation 1). However, determining the exact rolling temperature of the sample is challenging due to the uncertain cooling that occurred after preheating. It is also important to note that the cooling rate increases with the growing deformation, as the samples become thinner. The elevated cooling rate in the final samples and the deformation would favor the formation of martensite α''. Due to the high cooling rate and deformation, the β phase may undergo transformation into stress-induced martensite α''. The $Mo_{eq.}$ surpasses 8 wt%, providing support for martensite α'' formation. The formation of α'' provides a plausible explanation for the significant increase in hardness after the last deformation step (Figure 60). The identification of the orthorhombic phase is hindered by overlapping peaks. Contrary evidence arises from the microstructure, as existing literature describes fine laths within the prior β grain, whereas in our samples, the laths extend from the grain boundaries toward the center [51].

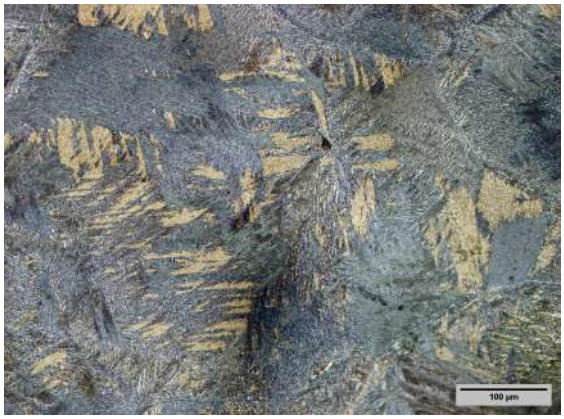

(a) 800 °C - 2nd caliber - longitudinal

(b) 800 °C - 4th caliber - longitudinal

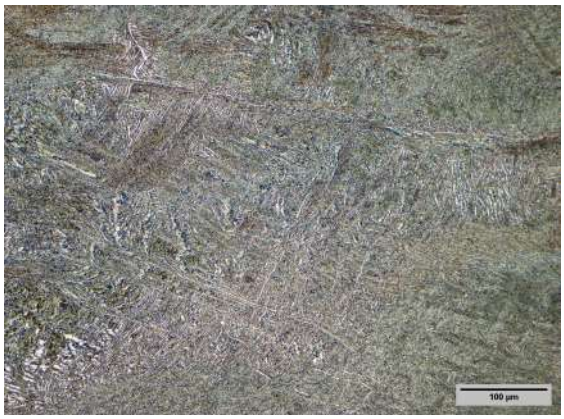

(c) 800 °C - 6th caliber - longitudinal

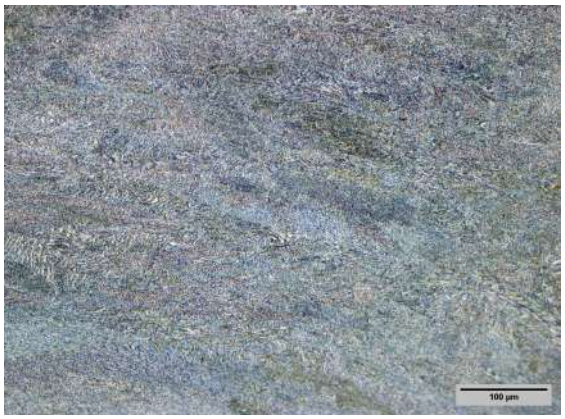

(d) 800 °C - 8th caliber - longitudinal

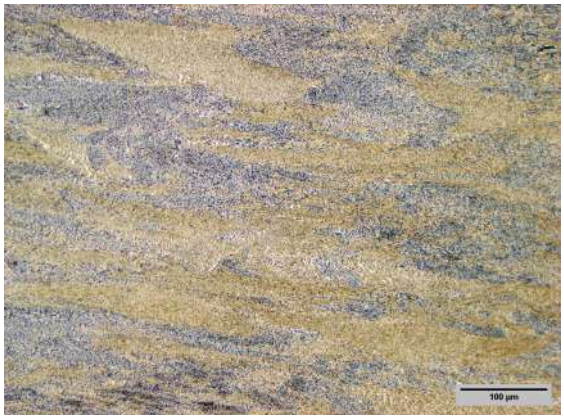

(e) 800 °C - 10th caliber - longitudinal

Figure 52: LOM images of the rolled Ti5.9Cu2Fe2Al samples with a preheating temperature of 800 °C in the longitudinal direction

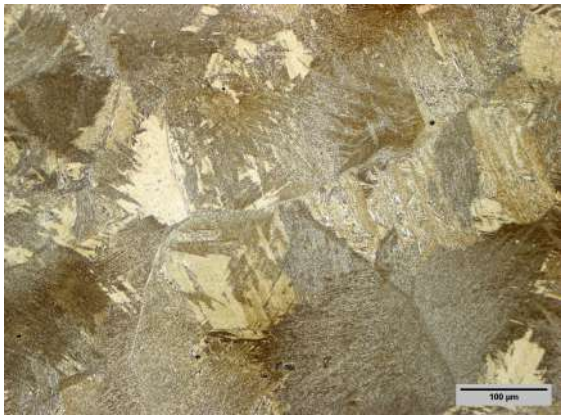

(a) 800 °C - 2nd caliber - perpendicular

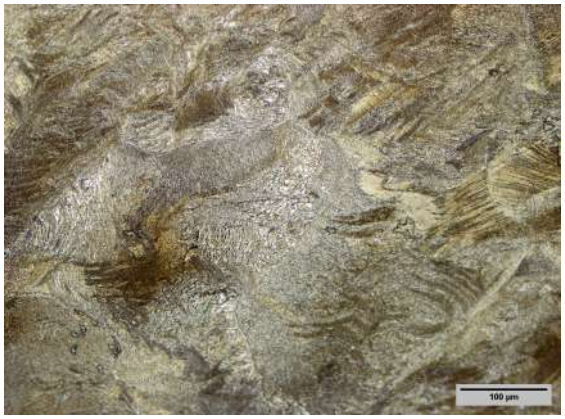

(b) 800 °C - 4th caliber - perpendicular

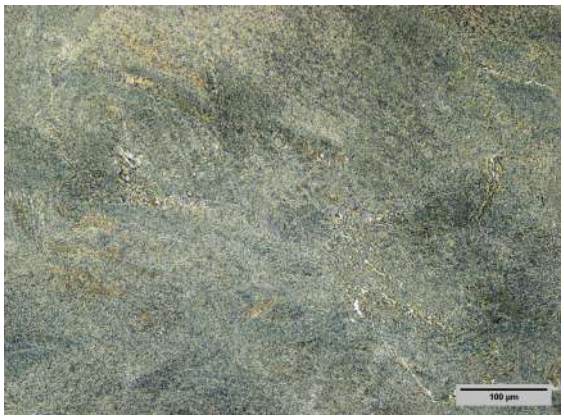

(c) 800 °C - 6th caliber - perpendicular

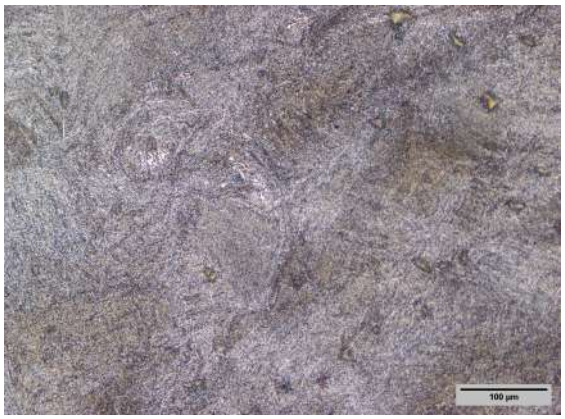

(d) 800 °C - 8th caliber - perpendicular

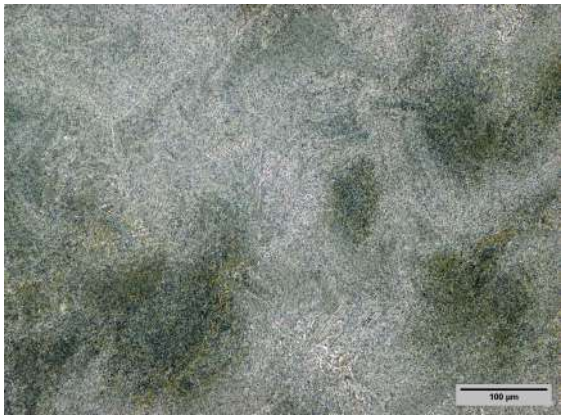

(e) 800 °C - 10th caliber - perpendicular

Figure 53: LOM images of the rolled Ti5.9Cu2Fe2Al samples with a preheating temperature of 800 °C in the perpendicular direction

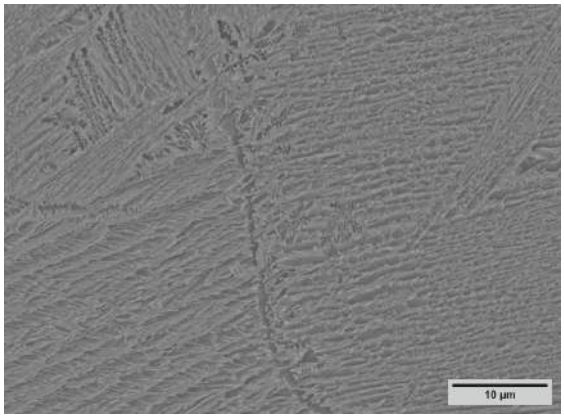

(a) 800 °C - 2nd caliber - longitudinal

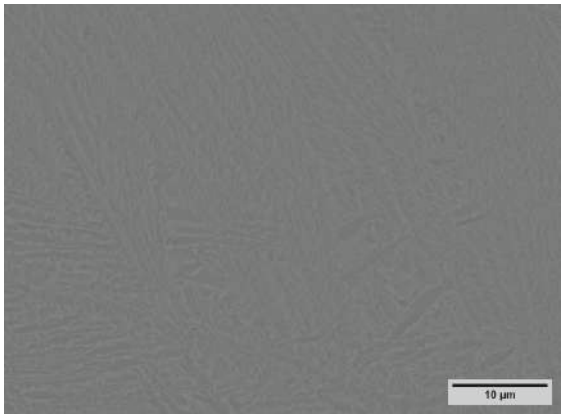

(b) 800 °C - 4th caliber - longitudinal

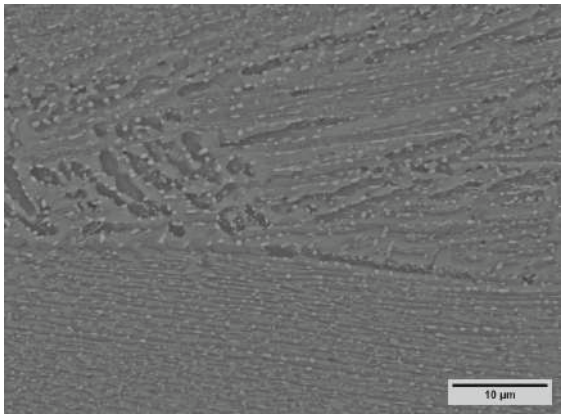

(c) 800 °C - 6th caliber - longitudinal

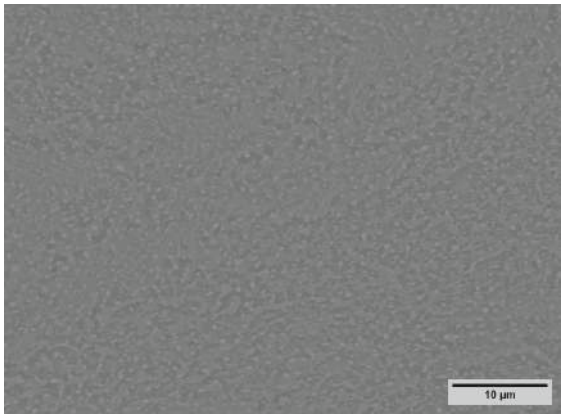

(d) 800 °C - 8th caliber - longitudinal

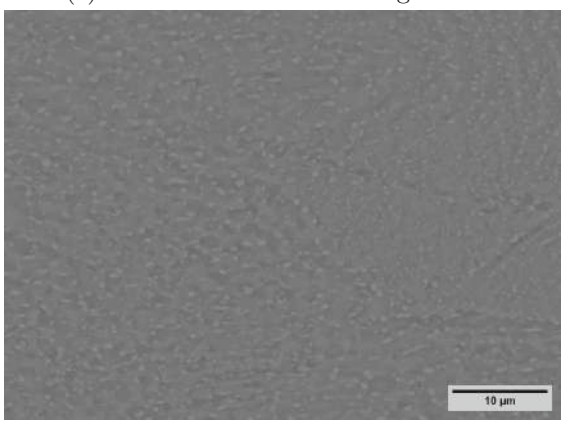

(e) 800 °C - 10th caliber - longitudinal

Figure 54: SEM images of the rolled Ti5.9Cu2Fe2Al samples with a preheating temperature of 800 °C in the longitudinal direction

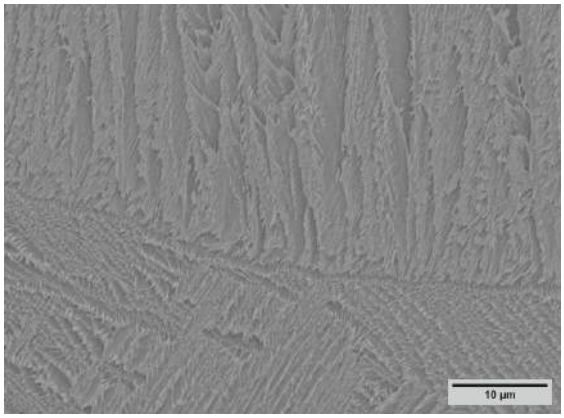

(a) 800 °C - 2nd caliber - perpendicular

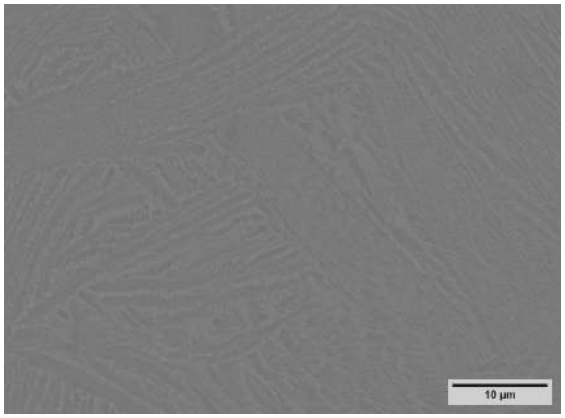

(b) 800 °C - 4th caliber - perpendicular

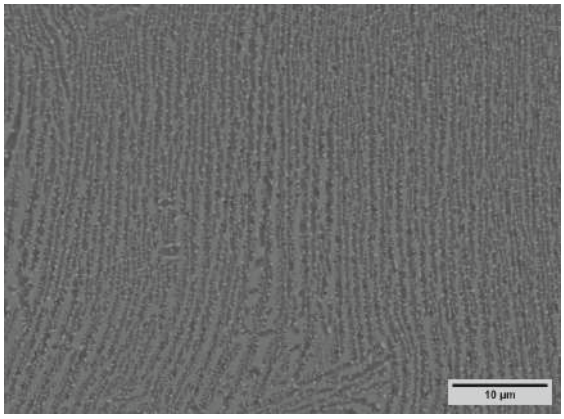

(c) 800 °C - 6th caliber - perpendicular

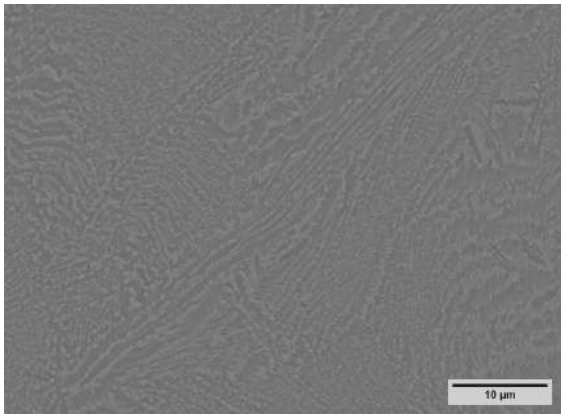

(d) 800 °C - 8th caliber - perpendicular

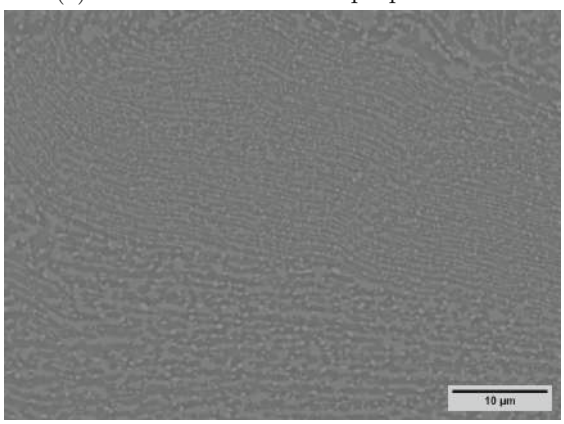

(e) 800 °C - 10th caliber - perpendicular

Figure 55: SEM images of the rolled Ti5.9Cu2Fe2Al samples with a preheating temperature of 800 °C in the perpendicular direction

(a) 1000 °C - 2nd caliber - longitudinal

(b) 1000 °C - 4th caliber - longitudinal

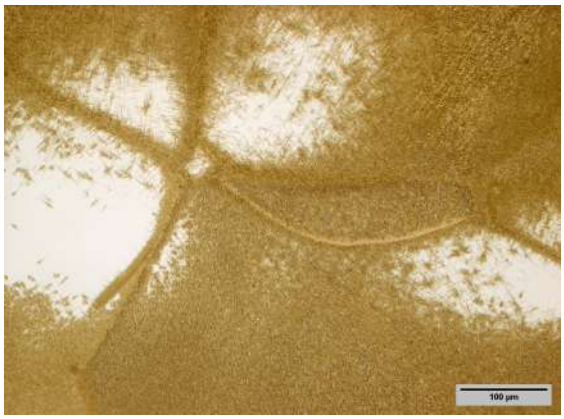

(c) 1000 °C - 6th caliber - longitudinal

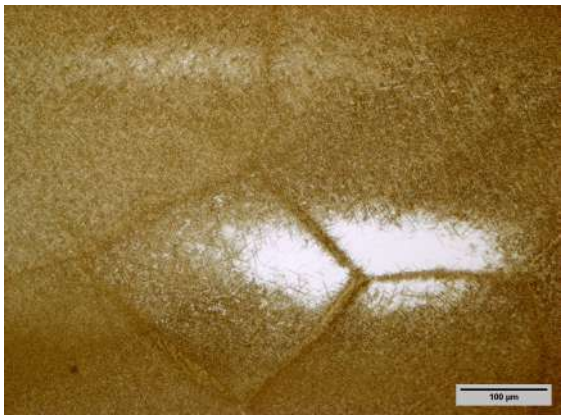

(d) 1000 °C - 8th caliber - longitudinal

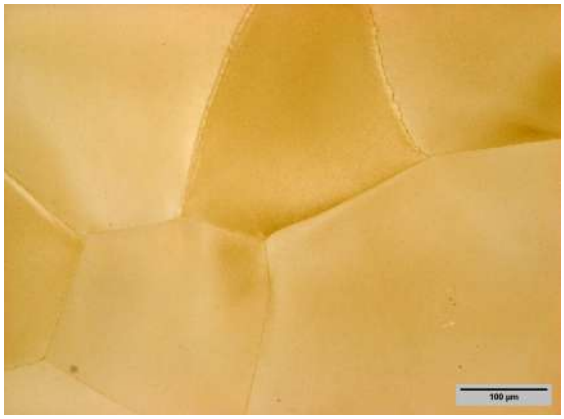

(e) 1000 °C - 10th caliber - longitudinal

Figure 56: LOM images of the rolled Ti5.9Cu2Fe2Al samples with a preheating temperature of 1000 °C in the longitudinal direction

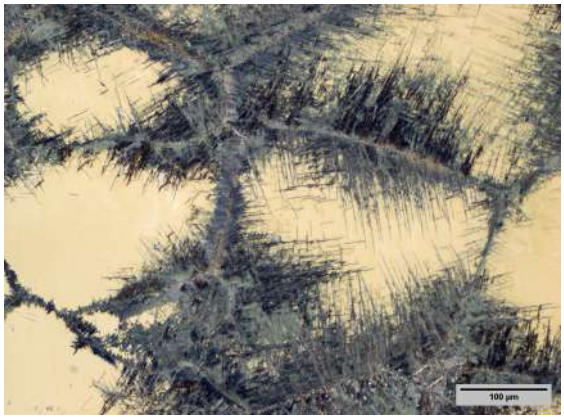

(a) 1000 °C - 2nd caliber - perpendicular

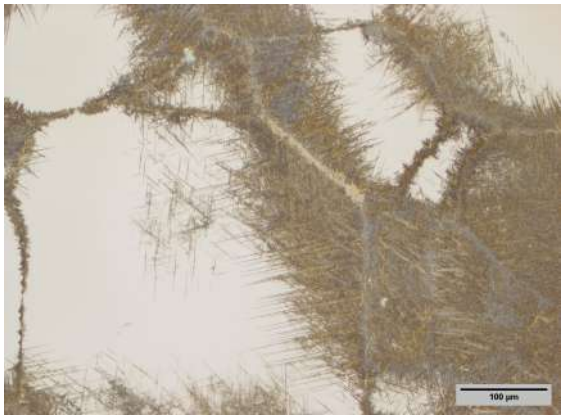

(b) 1000 °C - 4th caliber - perpendicular

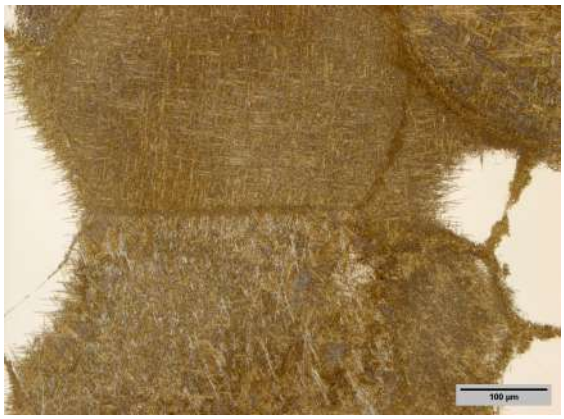

(c) 1000 °C - 6th caliber - perpendicular

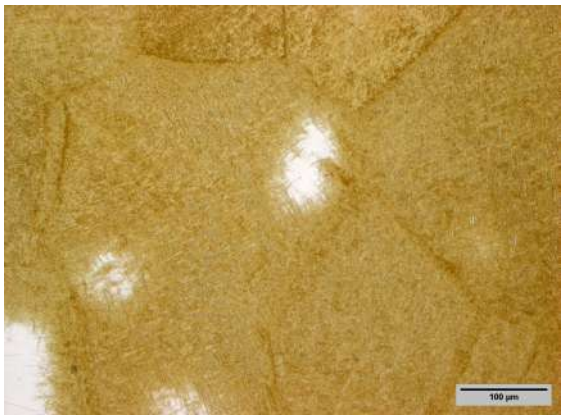

(d) 1000 °C - 8th caliber - perpendicular

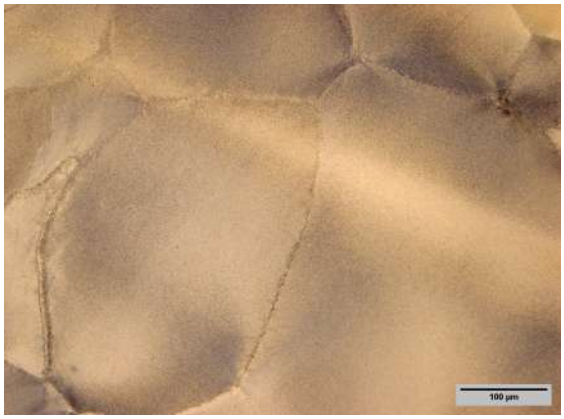

(e) 1000 °C - 10th caliber - perpendicular

Figure 57: LOM images of the rolled Ti5.9Cu2Fe2Al samples with a preheating temperature of 1000 °C in the perpendicular direction

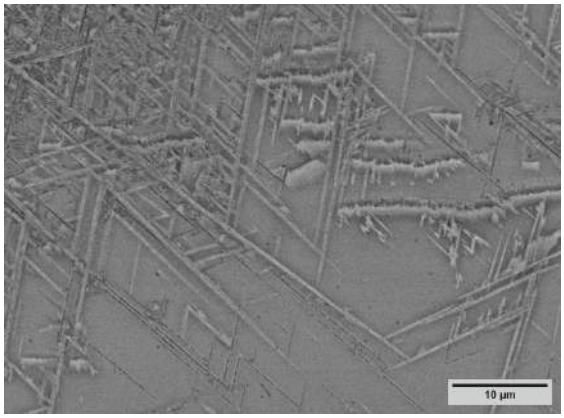

(a) 1000 °C - 2nd caliber - longitudinal

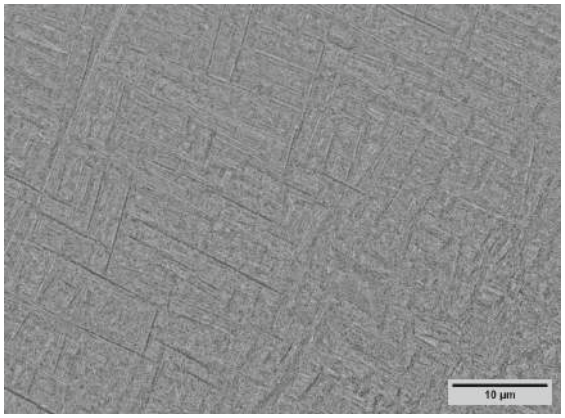

(b) 1000 °C - 4th caliber - longitudinal

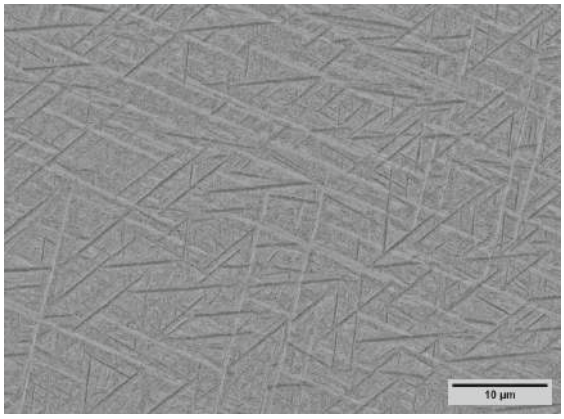

(c) 1000 °C - 6th caliber - longitudinal

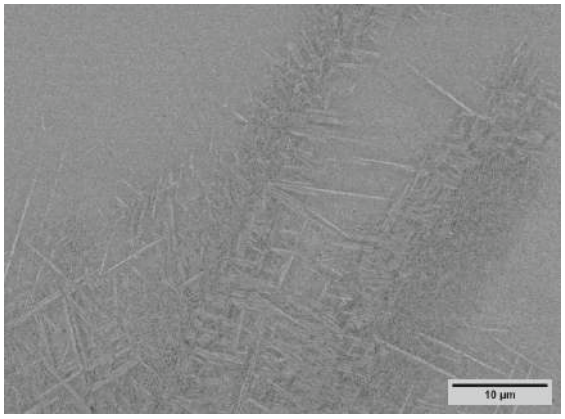

(d) 1000 °C - 8th caliber - longitudinal

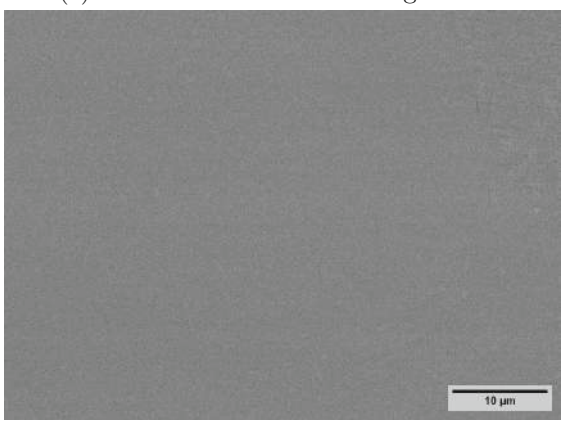

(e) 1000 °C - 10th caliber - longitudinal

Figure 58: SEM images of the rolled Ti5.9Cu2Fe2Al samples with a preheating temperature of 1000 °C in the longitudinal direction

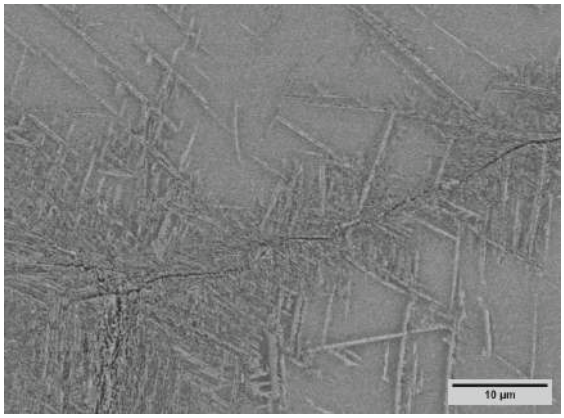

(a) 1000 °C - 2nd caliber - perpendicular

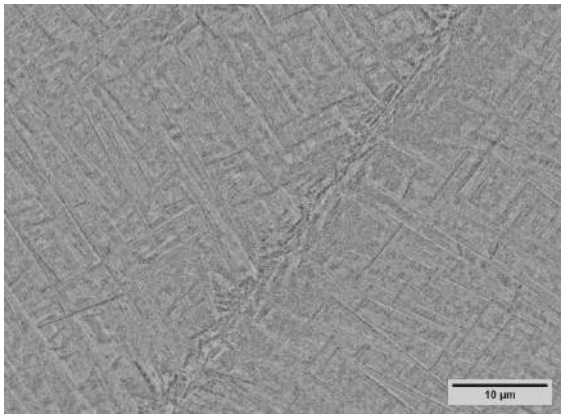

(b) 1000 °C - 4th caliber - perpendicular

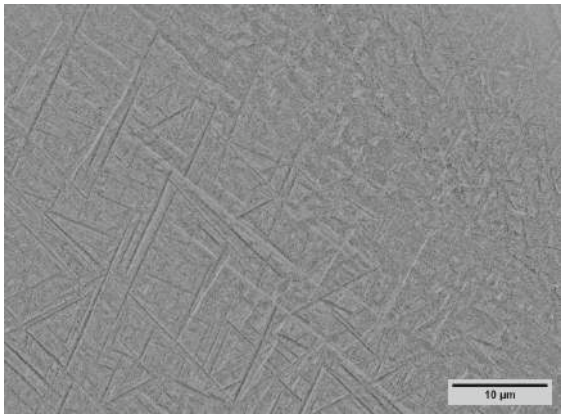

(c) 1000 °C - 6th caliber - perpendicular

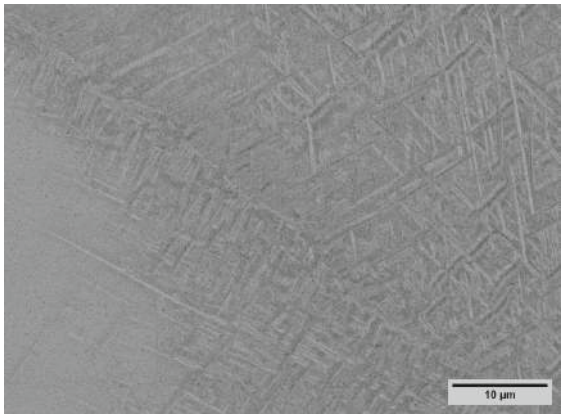

(d) 1000 °C - 8th caliber - perpendicular

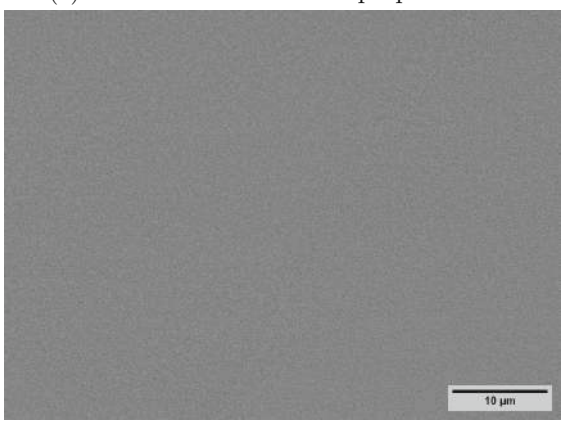

(e) 1000 °C - 10th caliber - perpendicular

Figure 59: SEM images of the rolled Ti5.9Cu2Fe2Al samples with a preheating temperature of 1000 °C in the perpendicular direction

The hardness values HV10 of the two sample series with different preheating temperatures (800 and 1000 °C) are summarized in Figure 60. It is to be noted that the sample at 800 °C from the 4th caliber in the longitudinal direction could not be measured due to its insufficient thickness.

The 800 °C sample series shows in general a slightly higher hardness compared to the starting material. The sample direction influences hardness, although a definitive trend cannot be identified. An increase in hardness during the rolling process could be expected because of the elongation and stress induced microstructural deformation.In contrast, a slight decrease in hardness is observed during the final two deformation steps, relative to the maximum hardness achieved at a deformation degree of 0.7. This may indicate the occurrence of a dynamic recovery process during the last two deformation steps.

The elevated preheating temperature of 1000 °C resulted in an increase in hardness of about 60 HV10 compared to the sample series preheated at 800 °C. This increase in hardness is attributed to the refinement of the microstructure, with the formation of very fine needle-like laths. The hardness reaches values up to 390 HV10, excluding the sample after the 10th caliber. Compared to the 800 °C sample series, the orientation of the samples influences the hardness less. This is consistent with the SEM observations, as the microstructure appears identical in both directions. At the final degree of deformation, the hardness increases to 540 HV10. The increase in hardness could be attributed to the potential formation of the hard but brittle martensitic phase α''. Another reason for the increase in hardness could be cold working, which would occur due to the rapid cooling of the thin sample during rolling. However, in this case, one would also expect an increase in hardness for the sample with a preheating temperature of 800 °C, contrary to the observed outcome.

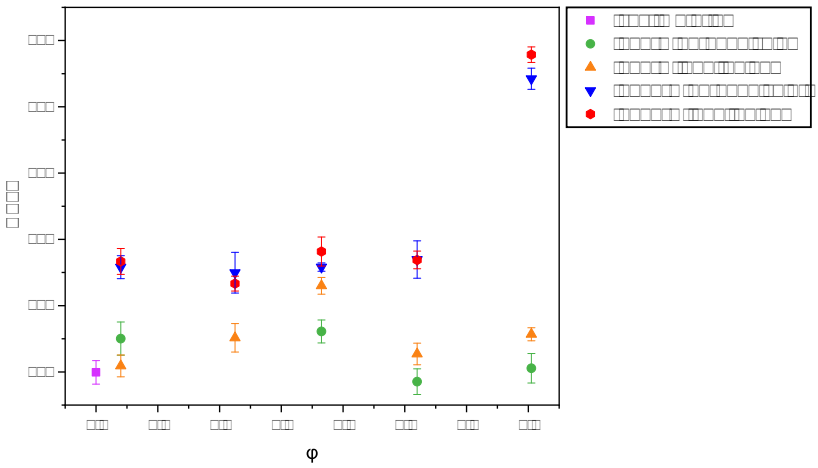

Figure 60: Hardness measurements HV10 of Ti5.9Cu2Fe2Al after caliber rolling with preheating temperatures of 800 °C and 1000 °C. The samples were analysed both in the rolling direction (longitudinal) and perpendicular to it. The hardness value of the cast material is included for reference. Note that the hardness of the Ti5.9Cu2Fe2Al-800 °C sample after the 4th caliber in the longitudinal direction could not be measured due to the insufficient thickness of the sample.

Figures 61 and 62 show the XRD measurements of the two sample series. In the 800 °C sample series α and β-titanium as well as Ti_2Cu could be found. The intermetallic phase was detected in each rolling step. The eutectoid could not be resolved under the SEM in the first two samples, which indicates a small size of the precipitations.

In the sample of the 8th caliber peaks at 47.5°, 48.5° and 60.8° could be detected. Compared to the XRD measurement of the casting material in Figure 43, the peaks were already detected in the original material. Therefore, inhomogeneities or oxides (i.e., CuO), which might have formed during the manufacturing of the material, could account for the presence of these peaks. The first two samples of the 1000 °C sample series show the same peaks, caused be CuO. Subsequently, these peaks disappear, potentially attributed to the dissolution of inhomogeneities or oxides during the rolling process. Another possibility is that the examined region of the material did not initially contain inhomogeneities or oxides.

As in the 800 °C sample series, mostly α, β-titanium and Ti_2Cu could be detected. SEM observations did not reveal any intermetallic phases, potentially due to their size being below the resolution limit (Figure 58 and 59). In the sample of the 6th caliber, small peaks could be attributed to TiO_2. Due to the high affinity of Ti to O and the high solid solubility of O in Ti, a titanium oxide layer can form rapidly. Nevertheless further analysis like an oxygen quantification would be required to verify the XRD results. Unfortunately, such analyses fall outside the scope of this thesis.

An unidentified peak at approximately 57° can be find in both samples series. This peak could not be clearly assigned, as previously discussed. Two β-titanium phases $Ti_{0.97}Fe_{0,36}Al_{2,67}$ or $Cu_{0.5}TiAl_{2.5}$ have a peak in this region and the most prominent peak overlaps with the Ti_2Cu peak at 39.5°. The intensity of the intermetallic β-Ti peak increases with increasing deformation degree at the 800 °C sample series. As the thickness of the samples decreases with each caliber, leading to higher cooling rates, this could explain the increased retention of β-titanium.

An opposite trend is seen at the 1000 °C sample series, except the sample at the 8th caliber. The decrease in the intensity could be attributed to the transformation of the retained β phase, which can be seen in the LOM pictures as the bright regions, in fine α laths or potentially α''. This process can be seen in the LOM pictures, as the bright regions completely disappear in the rolling process (Figure 56 and 57).

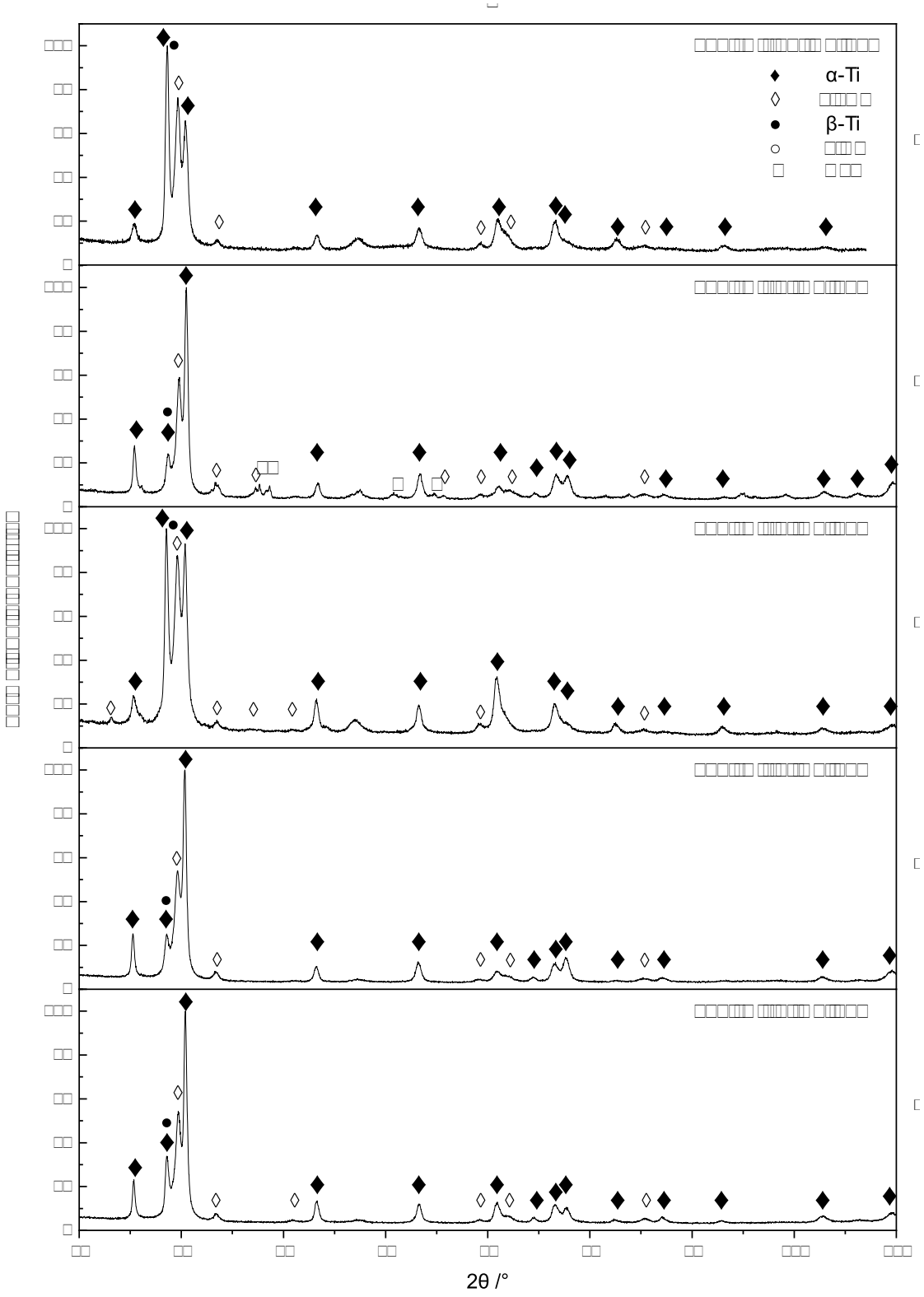

Figure 61: XRD measurements of the rolled Ti5.9Cu2Fe2Al samples with 800 °C preheating temperature

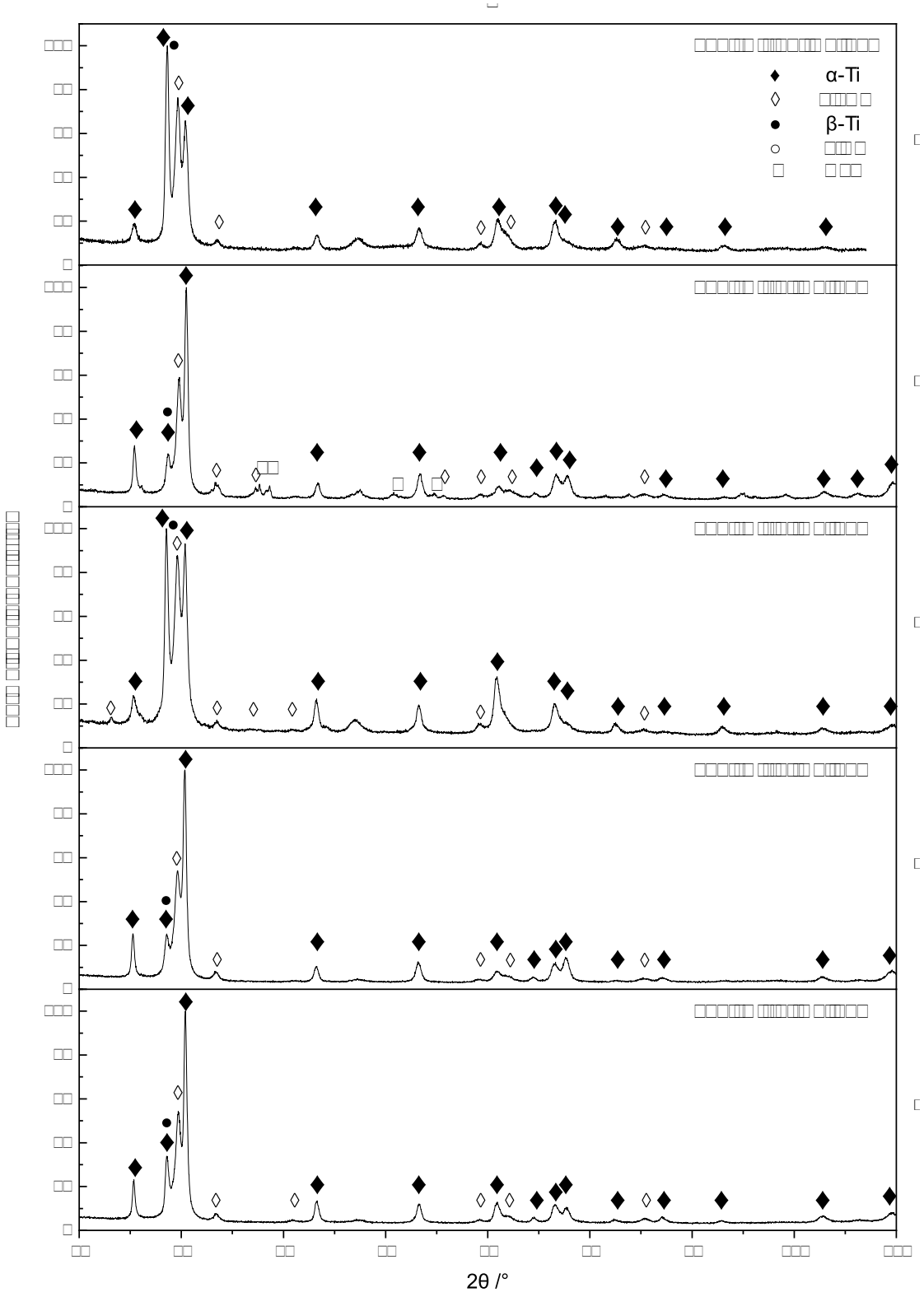

Figure 62: XRD measurements of the rolled Ti5.9Cu2Fe2Al samples with 1000 °C preheating temperature

To determine the evolution of the crystallite size, XRD measurements were analysed after the Rietveld refinement using the Scherrer calculation. The Scherrer equation refers to the indirect proportionality of the crystallite size to the Full Width at Half Maximum (FWHM) as seen in Equation 5. For the analysis only the peaks with clear phase assignment and phases, which are found in all samples, were taken into account. Therefore only α-Ti and Ti_2Cu are analysed. In Table 15 the results of the mean crystallite size are summarized.

$$D = \frac{K \cdot \gamma}{\beta \cdot cos\theta} \tag{5}$$

D ..... crystallite size (Å)
K ..... Scherrer constant (0.9)
γ ..... wavelength of X-rays(nm)
β ..... Full Width at Half Maximum FWHM(°)
θ ..... peak position (°)

The sample series at the preheating temperature of 800 °C shows a decrease of the crystallite size of α-titanium with increasing deformation degree. The crystallite size ranges from 358 down to 225 Å. In contrast, the size of the Ti_2Cu phase remains unchanged, but increases in the final two calibers, from 214 to 244 Å. This trend aligns with the observations in the SEM, as the intermetallic phase is only visible in the samples after a deformation degree of 0.7 (Figures 55 and 54).

The 1000 °C sample series follows the same trend regarding the α-titanium, but with a rapid decrease of the crystallite size to 162 Å in the final rolling step. The refinement of the microstructure can also be observed in the LOM and SEM. The grain refinement during the last deformation step explains the rapid increase in hardness (Figure 60). The decrease of the crystallite size suggests that recrystallisation occurred during the rolling process. In contrast to the 800 °C sample series, the intermetallic Ti_2Cu phase shows a slight refinement of crystallites during the rolling process, although the overall size remains larger compared to the 800 °C sample series. This observation does not align with the SEM results, as no intermetallic phases were resolved.

Due to the numerous influences on the calculation method, a very large standard deviation is observed, rendering the method less reliable.

Table 15: Summary of the calculated crystallite size of the rolled samples at different preheating temperatures (800 °C and 1000 °C). The phases α-Ti and Ti_2Cu were analysed.

		800 °C (Å)				1000 °C (Å)			
Caliber	φ	α-Ti	deviation	Ti_2Cu	deviation	α-Ti	deviation	Ti_2Cu	deviation
2	0.08	358	112	219	51	343	129	316	47
4	0.45	338	26	214	30	347	146	242	146
6	0.73	291	95	216	67	303	109	299	74
8	1.04	279	69	244	131	284	104	295	80
10	1.41	225	98	242	77	162	20	275	-

4.6 Deformation Dilatometry

The Archimedes density was measured to verify the suitability of the cylindrical samples produced in the arc furnace for measurement. Table 16 summarizes the density of the samples before the deformation. It is evident that a minimum of 97.5 % of the theoretical density could be achieved during the production of the samples. Therefore, the samples are considered suitable for the deformation experiments.

Table 16: Density of samples for the DIL; standard deviation of balance assumed to be 0.1 mg due to single weighing of entire sample

	Nr.	density g/cm^3	% theoretical density		Nr.	density g/cm^3	% theoretical density
Ti	1	4.492	99.82	Ti5Zr	1	4.534	99.19
	2	4.496	99.91		2	4.557	99.70
	3	4.482	99.61		3	4.527	99.05
	4	4.490	99.78	Ti10Zr	1	4.526	97.49
	5	4.507	100.15	Ti15Zr	1	4.671	99.01
	6	4.491	99.80		2	4.722	100.08
$Ti1ZrO_2$	1	4.470	99.13		3	4.649	98.54
	2	4.506	99.92	Ti6.5Cu3Zr	1	4.678	99.63
	3	4.511	100.03	Ti6.5Cu10Zr	1	4.771	99.33
	4	4.498	99.74		2	4.753	98.96
$Ti2ZrO_2$	1	4.507	99.74		3	4.689	97.61

To obtain the true stress/strain curve of the deformation experiment, it is important to consider the deformation of the sample during compression. During an ideal uniform uniaxial compression the sample maintains its cylindrical shape, hence only the change of length and height has to be taken into account. In this case, the true stress σ_t and true strain ϵ_t can be calculated from the engineering stress or strain using Equation 6. Because of inhomogeneous distribution of deformation, a barrelling effect, resulting in undeformed 'dead metal zone', takes place. This effect can be attributed to interface friction and axial temperature gradients [52]. In this thesis, the ideal scenario is considered, in which the barrelling effect is disregarded, thus using Equation 5.

$$\begin{aligned} \sigma_t &= \sigma(1+\epsilon) \\ \epsilon_t &= ln(1+\epsilon) \end{aligned} \tag{6}$$

σ_t ..... true stress (MPa)
σ ..... engineering stress (MPa)
ϵ_t ..... true strain (-)
ϵ ..... engineering strain (-)

Figure 63 depicts the true stress/strain diagrams of the four measured systems: Ti, TixZr, Ti6.5CuxZr and TixZrO_2. All samples achieved a true strain of approximately 0.47. With the exception of the Ti6.5Cu10Zr - 700 °C - 0.01^{-1} sample, all measurements show a general increase in stress during hot compression, characterized by a rapid ascent within the initial 0.05 true strain. Therefore, it is most likely that an error occurred during the measurement of the Ti6.5Cu10Zr - 700 °C - 0.01 s^{-1} sample. The lower density of 99.5% of the theoretical density, in comparison to the other samples, could provide a potential explanation for the observed error. Compression tests at 900 °C and a strain rate of 0.01 s^{-1} exhibit a steady-state flow, especially the samples Ti15Zr and Ti6.5Cu10Zr. At the same temperature but a strain rate of 10 s^{-1} the maximum σ_t is approximately four times higher. A similar trend is also observed in the deformation at 700 °C, as the true stress approximately doubles with the increase of the strain rate from 0.01 to 10 s^{-1}. This indicates a strong influence of the strain rate on the stress.

The maximum true stress of 812 MPa was measured in pure titanium at 700 °C and a strain rate of 10 s^{-1}. The addition of 5 wt% Zr led to a reduction in the maximum true stress to 716 MPa. Subsequent measurements on Ti1ZrO_2 under the same conditions revealed a further decrease to 624 MPa. Measurements under different conditions generally undergo this same trend. Therefore it is to be noted that the addition of alloying elements to titanium, ie. copper as a β stabilizer, results in a decrease of maximum true stress.

It is observed that with increase in temperature the stress decreases. With temperatures above the α/β transus temperature, in this case 900 °C, the deformation occurs in the more ductile β region, consequently requiring less stress for the deformation process. An increase in the strain rate results in an increase of the stress.

A pure titanium sample was measured twice at 900 °C and a strain rate of 0.01 s^{-1}, named Ti - 900 °C - 0.01 s^{-1}(_2). The course of the curve as well as the maximum value of true strain (149 and 120 MPa) are nearly identical, which gives a good insight of the reproducibility of the results.

Bodunrin et al. [53] investigated hot compression test of Ti6Al4V at temperatures ranging from 750 to 950 °C and strain rates from 0.01 to 10 s^{-1}. The deformation of the samples show an initial sharp peak due to strain hardening, followed by a decrease in flow stress due to restoration processes. A dynamic equilibrium adjusts as the dynamic softening and hardening effects equalize. All samples exhibited a continuous flow softening at deformation temperatures below 900 °C, whereas a steady state flow stress occurred at 950 °C. Afterwards a decrease in flow stress can be observed. The same trend was described in [54–56]. The stress decrease can be explained by various softening mechanism such as dynamic recovery (DRC), dynamic recrystallisation (DRX) or dynamic globularisation. As can be observed in Figure 63, no flow softening occurs in the measured samples. This indicates that no softening mechanism like DRC and DRX took place during the deformation. Subsequent heat treatment would be necessary to achieve recrystallisation.

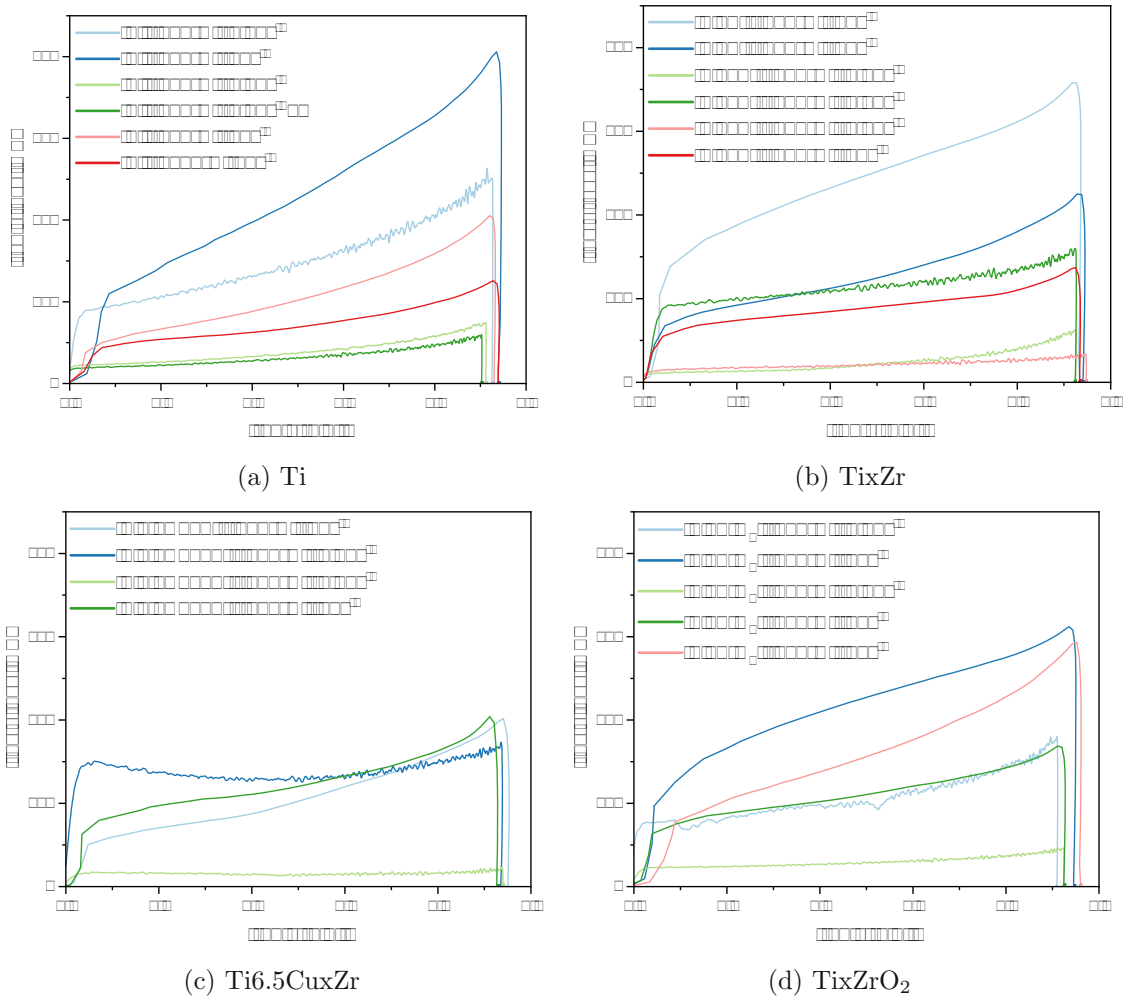

(a) Ti (b) TixZr

(c) Ti6.5CuxZr (d) $TixZrO_2$

Figure 63: True stress/strain diagrams of the measured sample series (Ti, TixZr, Ti6.5CuxZr, $TixZrO_2$) at different temperatures (700 and 900 °C) and strain rates (0.01 or 10 s^{-1}).

To investigate the impact of deformation parameters, various samples were selected for microstructure analysis. From the Ti6.5Cu10Zr series, samples deformed at 900 °C were chosen to study the effect of different strain rates. To analyse the temperature influence, two $Ti1ZrO_2$ samples, deformed at a strain rate of 10^{-1} but at different temperatures, were selected. For comparison, a Ti15Zr sample deformed at 900 °C and a strain rate of 10^{-1} was also analysed.

Figure 64 provides a cross-sectional view of the selected samples along the longitudinal deformation direction. The schematic representation of the deformed samples, shown in 64a, marks the deformation direction and the observed areas (center and edge). In all samples, a deformed area in the center and a dead metal zone at the edge, resulting from the barreling effect, can be observed (Figure 64b - f). In the center, the microstructure is more refined and elongated compared to the dead metal zone, where the microstructure did not undergo deformation. Further insights into the sample's microstructure are depicted in detailed images of the center and edge sections in Figures 65 to 68.

Ti6.5Cu10Zr samples, which were both deformed at 900 °C, but at different strain rates, are depicted in Figure 65a to d. The microstructure formed under the higher strain rate of 10 s^{-1} is coarser in both areas (center and edge). At the edge of the both samples equiaxed grains formed with α/β laths, which are aligned perpendicular to the deformation direction in the center. Compared to the as-cast sample (Figure 16d), the laths are coarser, and the interim areas, identified as retained β phase, are not as organized, as exemplified in the sample Ti6.5Cu10Zr - 900 °C - 10 s^{-1} (Figure 65d). In the center the retained β phase forms paths perpendicular to the deformation direction.

The α laths at the edge of the Ti6.5Cu10Zr samples refine with a higher strain rate, as seen in Figure 66b and d. The globular α grains, which are predominantly observed at the edges of the samples (Figure 66b), become more refined and pronounced in the center (Figure 66c). These globular grains are also visible in the sample deformed at a strain rate of 10 s^{-1}, though to a lesser extent in the dead metal zone (Figure 66d) and absent in the center (Figure 66c). The globularisation of α lamellae is influenced by strain, as this promotes the break-up of lamellae, and by diffusion, which completes the globularisation process. As diffusion is enhanced by an increase in temperature and a decrease in strain rate, the globularised volume fraction increases with these conditions [56]. This trend is evident, as the globularisation is more pronounced in the sample deformed at the lower strain rate of 0.01 s^{-1}. However, in the literature [56] the effect of globularisation was accompanied by a decrease in flow stress, which cannot be observed in this sample.

Sample Ti15Zr - 900 °C - 10 s^{-1} formed a coarser α/β microstructure with Widmannstätten features in the center, as can be observed in Figure 66e and f. The microstructure in the dead metal zone is comparable to the as-cast sample (Figure 14e), although a coarsening can be observed. The α microstructure is more refined in the center of the sample,

The sample Ti1ZrO_2 - 700 °C - 10 s^{-1} depicts coarse laths in the dead metal zone (Figure 67b), whereas the sample deformed at 900 °C exhibits equiaxed grains with laths colonies (Figure 67d). The laths of the lamellar structure in the sample deformed at 700 °C are noticeably longer than those in the colonies of the sample deformed at 900 °C (Figure 68b and d). The microstructure becomes more refined in the center, where deformation occurs (Figure 67a and c). In sample Ti1ZrO_2 - 900 °C - 10 s^{-1} fine equiaxed grains with no misorientation or deformation can be resolved under the SEM, as depicted in Figure 68c. Compared to the as-extruded sample in Figure 33c and d, the laths at the edge of sample Ti1ZrO_2 - 700 °C - 10 s^{-1} are significantly more refined. This refinement can be attributed to the production method of the sample. The samples used for the deformation dilatometry were prepared using an arc furnace, which resulted in rapid cooling of the samples. In contrast, the as-extruded samples experienced a slower cooling rate, resulting in a coarser microstructure.

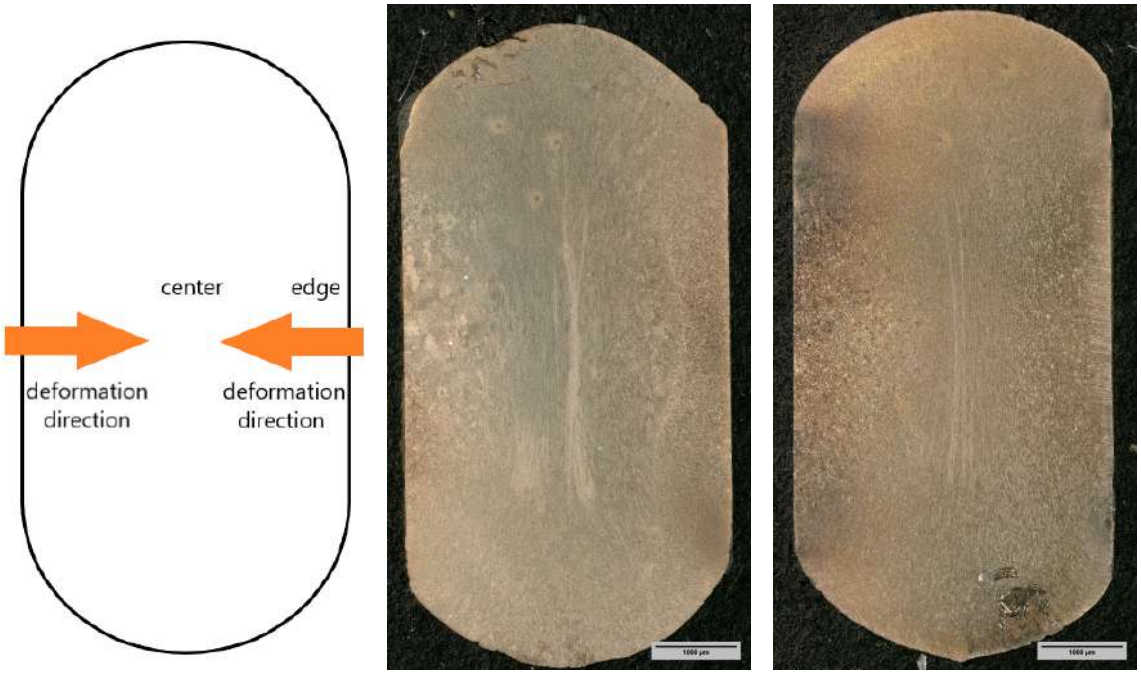

(a) schema of deformed sample

(b) Ti6.5Cu10Zr - 900 °C - 0.01 s^{-1}

(c) Ti6.5Cu10Zr - 900 °C - 10 s^{-1}

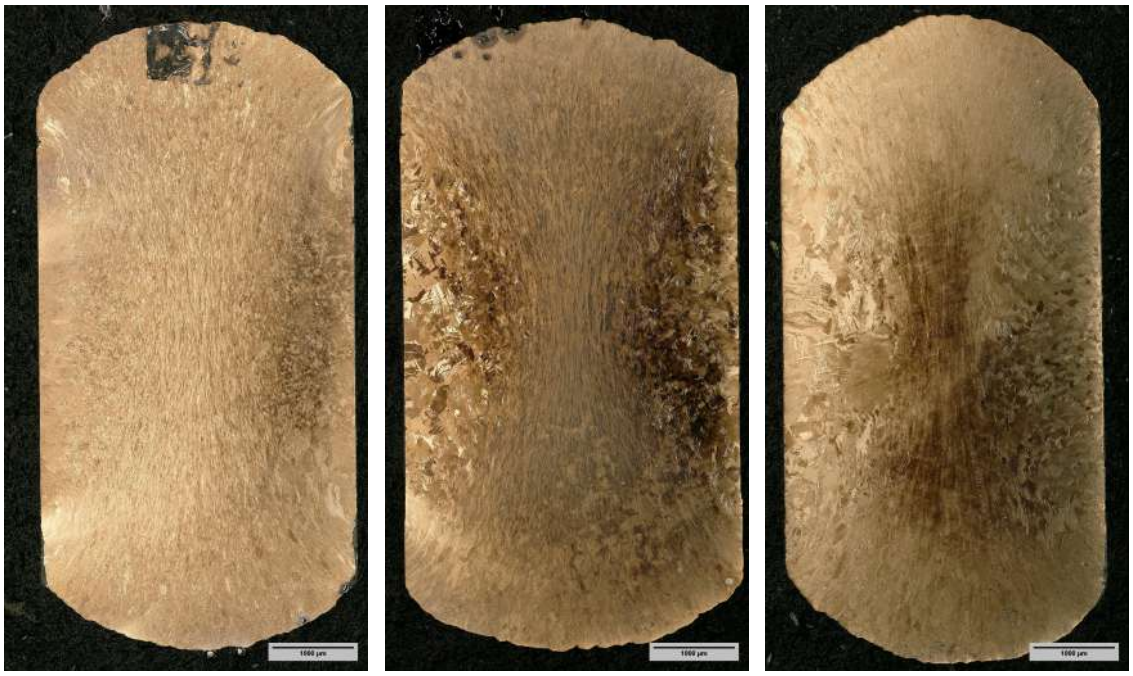

(d) Ti15Zr - 900 °C - 10 s^{-1}

(e) $Ti1ZrO_2$ - 700 °C - 10 s^{-1}

(f) $Ti1ZrO_2$ - 900 °C - 10 s^{-1}

Figure 64: LOM panorama images of deformed samples using deformation dilatometry. The samples were deformed at different temperatures (700 or 900 °C) with different strain rate (0.01 or 10 s^{-1}). For better understanding of the deformation direction and the location of the observed areas (center, edge) a schema of the deformed samples was added (a).

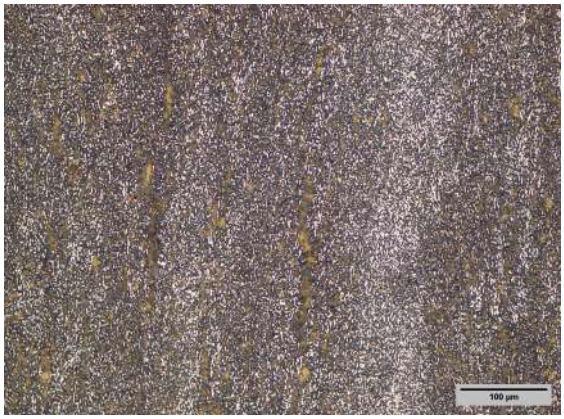

(a) Ti6.5Cu10Zr - 900 °C - 0.01 s^{-1}

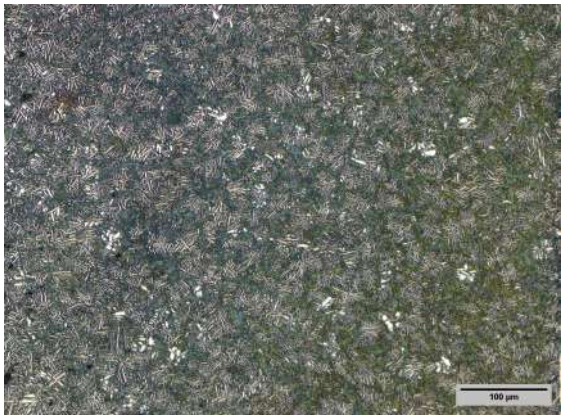

(b) Ti6.5Cu10Zr - 900 °C - 0.01 s^{-1} - edge

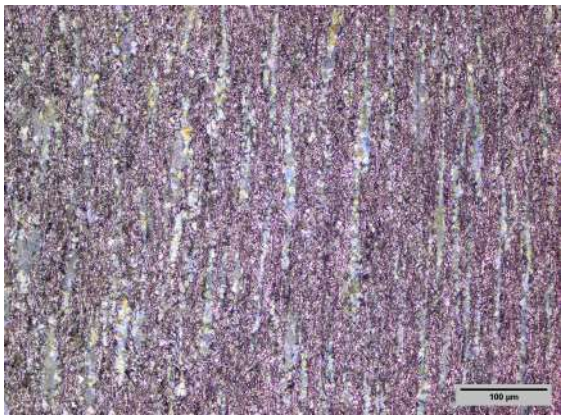

(c) Ti6.5Cu10Zr - 900 °C - 10 s^{-1}

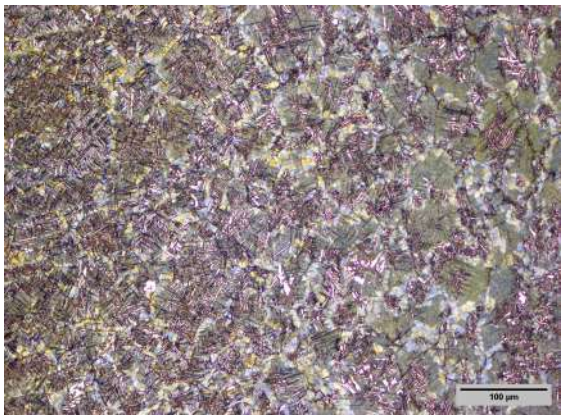

(d) Ti6.5Cu10Zr - 900 °C - 10 s^{-1} - edge

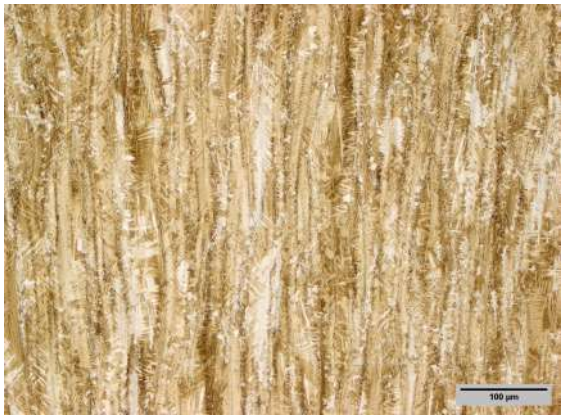

(e) Ti15Zr - 900 °C - 10 s^{-1}

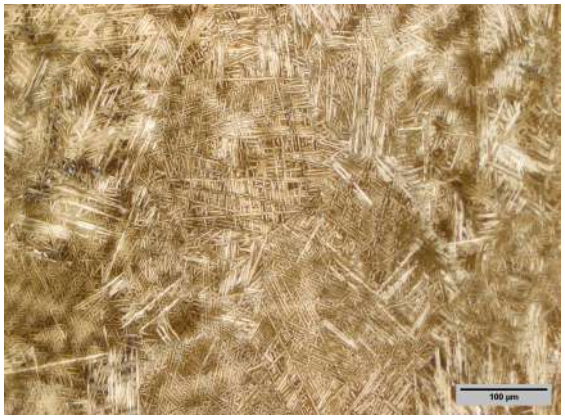

(f) Ti15Zr - 900 °C - 10 s^{-1} - edge

Figure 65: LOM images of deformed samples using deformation dilatometry. The samples were deformed at 900 °C with different strain rate (0.01 or 10 s^{-1}). The detailed images are taken from the center of the sample (a, c, e) and the edge ('dead metal zone') of the sample (b, d, f).

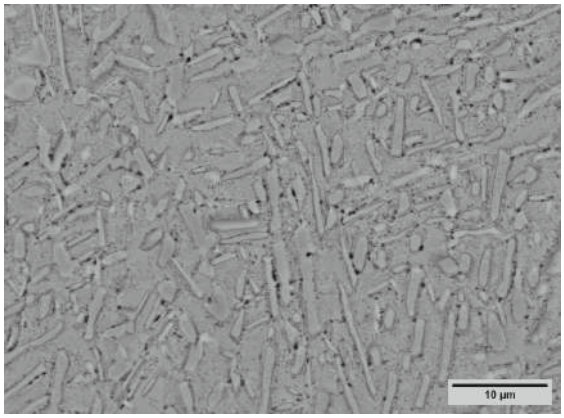

(a) Ti6.5Cu10Zr - 900 °C - 0.01 s^{-1}

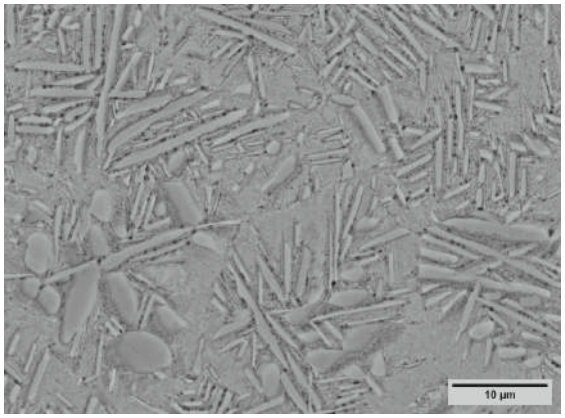

(b) Ti6.5Cu10Zr - 900 °C - 0.01 s^{-1} - edge

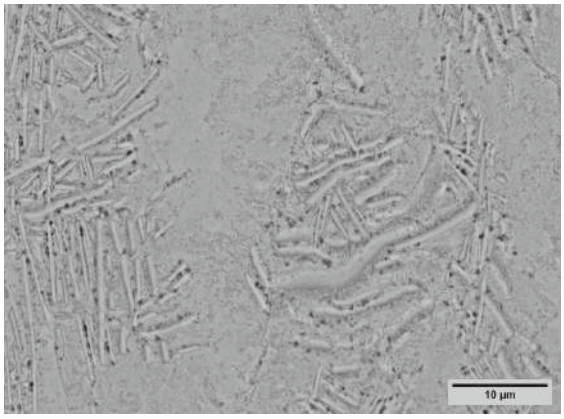

(c) Ti6.5Cu10Zr - 900 °C - 10 s^{-1}

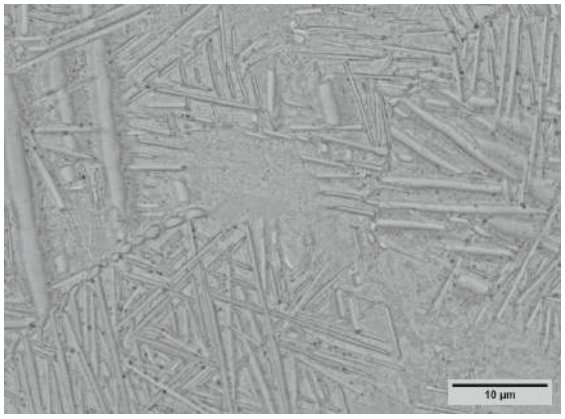

(d) Ti6.5Cu10Zr - 900 °C - 10 s^{-1} - edge

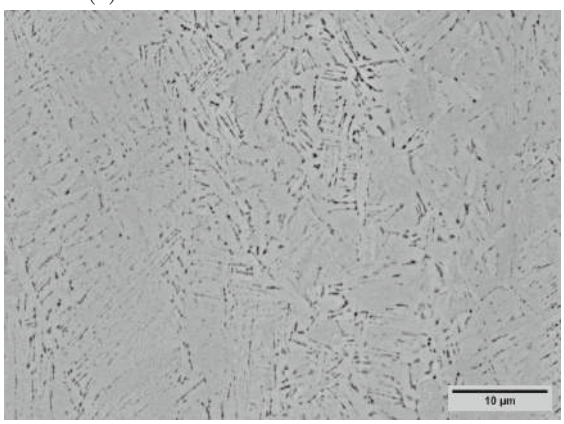

(e) Ti15Zr - 900 °C - 10 s^{-1}

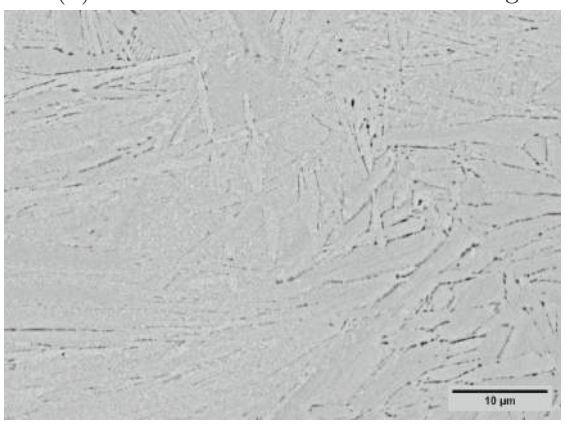

(f) Ti15Zr - 900 °C - 10 s^{-1} - edge

Figure 66: SEM images of deformed samples using deformation dilatometry. The samples were deformed at 900 °C with different strain rate (0.01 or 10 s^{-1}). The detailed images are taken from the center of the sample (a, c, e) and the edge ('dead metal zone') of the sample (b, d, f).

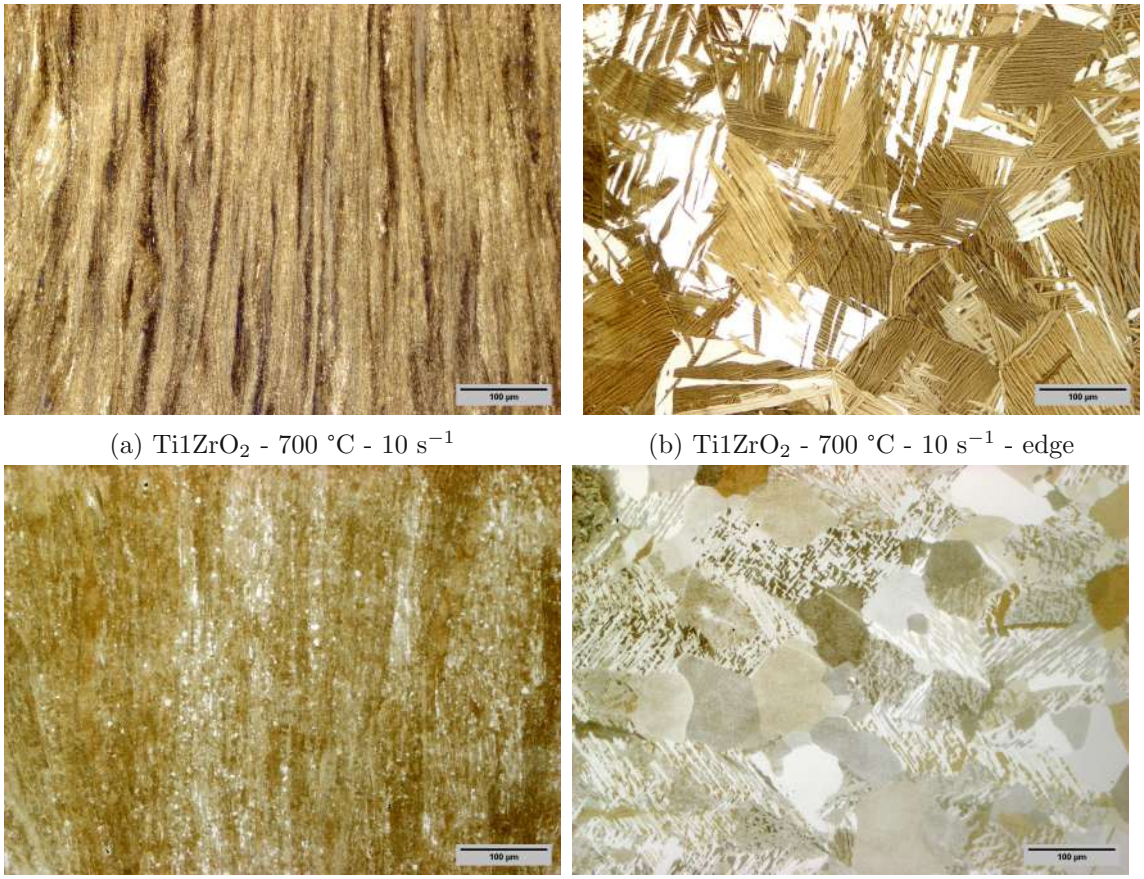

(a) $Ti1ZrO_2$ - 700 °C - 10 s^{-1}

(b) $Ti1ZrO_2$ - 700 °C - 10 s^{-1} - edge

(c) $Ti1ZrO_2$ - 900 °C - 10 s^{-1}

(d) $Ti1ZrO_2$ - 900 °C - 10 s^{-1} - edge

Figure 67: LOM images of deformed samples $Ti1ZrO_2$ using deformation dilatometry. The samples were deformed at different temperatures (700 or 900 °C) with a strain rate of 10 s^{-1}. The detailed images are taken from the middle of the sample (a, c) and the edge ('dead metal zone') of the sample (b, d).

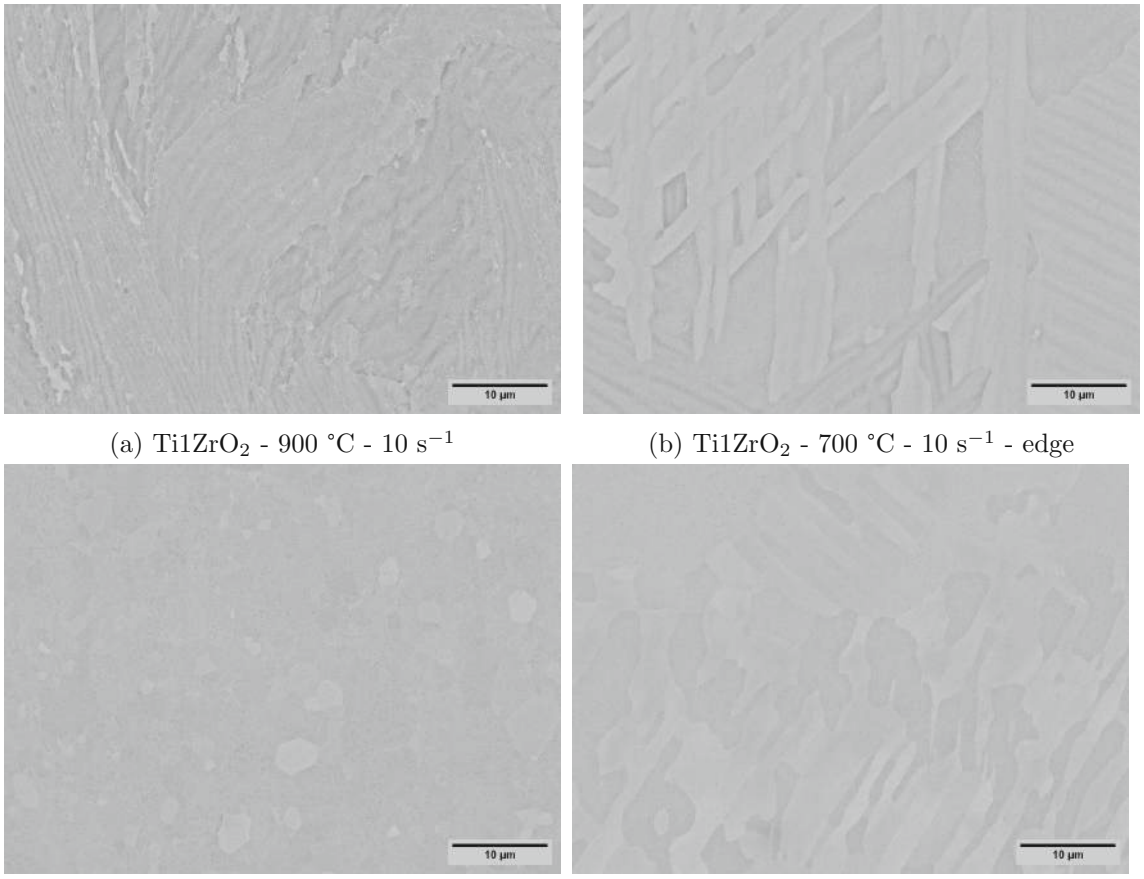

(a) $Ti1ZrO_2$ - 900 °C - 10 s^{-1}

(b) $Ti1ZrO_2$ - 700 °C - 10 s^{-1} - edge

(c) $Ti1ZrO_2$ - 900 °C - 10 s^{-1}

(d) $Ti1ZrO_2$ - 900 °C - 10 s^{-1} - edge

Figure 68: SEM images of deformed samples $Ti1ZrO_2$ using deformation dilatometry. The samples were deformed at different temperatures (700 or 900 °C) with a strain rate of 10 s^{-1}. The detailed images are taken from the middle of the sample (a, c) and the edge ('dead metal zone') of the sample (b, d).

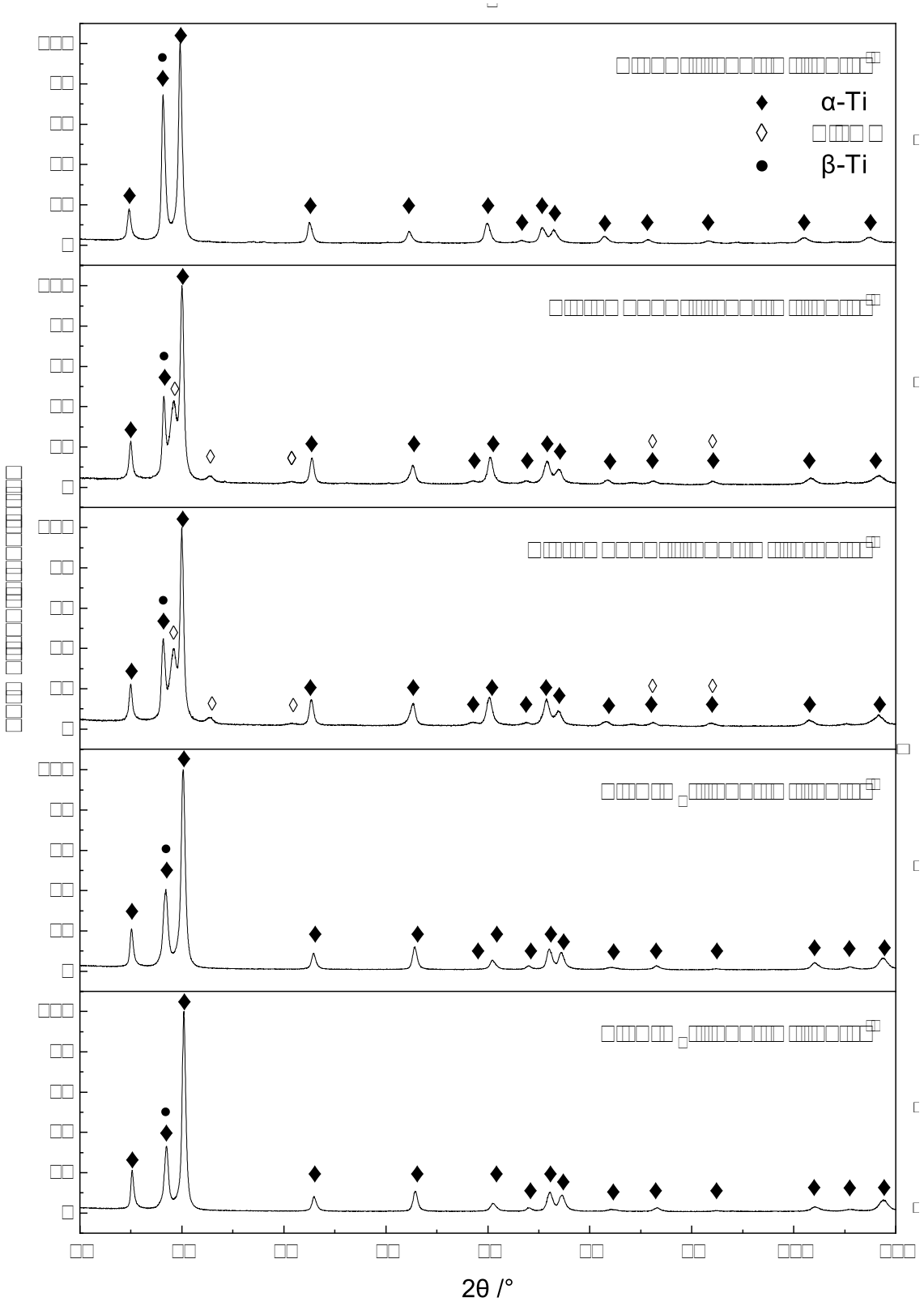

Figure 69: XRD measurements of the deformed sample series Ti15Zr, Ti6.5Cu10Zr and Ti1ZrO_2

Figure 69 depicts the XRD measurements of the previous discussed samples. Compared to the respective as-cast or as-extruded samples, no differences were observed. The phases α, β-titanium and Ti_2Cu could be identified. Compared to α and β-Ti, the eutectoid phase Ti_2Cu was not observed under the SEM due to its unresolvable size.

The development of the crystallite size depending on deformation parameters was analysed using the Scherrer calculation (Equation 5). For reference, the as-cast or as-extruded samples were also analysed. The results are summarized in Table 17.

In all sample series, a decrease in crystallite size is observed, attributed to deformation processes. The Ti6.5Cu10Zr sample series exhibits a relatively slight decrease in crystallite size, approximately 7 Å, after deformation. This reduction is notably less pronounced compared to the other two sample series, which exhibit an average decrease of around 47 Å.

The crystallite size decreases further with increasing temperature, as observed in the $Ti1ZrO_2$ sample series. This trend indicates that higher temperatures promote further refinement of the crystallite structure. In contrast, strain rate variations do not significantly influence the crystallite size in the Ti6.5Cu10Zr sample series. Therefore, it can be concluded that temperature has a greater impact on microstructural changes than strain rate.

Table 17: Summary of the calculated crystallite size of the samples deformed by the deformation dilatometry. For reference the as-cast and as-extruded samples were also analysed.

sample	α-Ti (Å)	deviation (Å)
Ti6.5Cu10Zr as-cast	306	71
Ti6.5Cu10Zr - 900 °C - 0.01 s^{-1}	299	65
Ti6.5Cu10Zr - 900 °C - 10 s^{-1}	301	60
Ti15Zr as-cast	225	47
Ti15Zr - 900 °C - 10 s^{-1}	268	77
$Ti1ZrO_2$ as-extruded	317	42
$Ti1ZrO_2$ - 700 °C - 10 s^{-1}	268	42
$Ti1ZrO_2$ - 900 °C - 10 s^{-1}	211	65

5 Conclusion

The Ti-Zr alloys were prepared by different production methods, including arc furnace, vacuum sintering, and hot extrusion. Arc furnace and hot extrusion produced samples with a high density above 99 % of the theoretical density. The sintered samples TixZrH_2 reached a minimum of 80 % of the theoretical density. The low density is attributed to unsuccessful pressing due to the globular Ti powder. To ensure a higher density in the sintered samples, a better pressing Ti powder can be used or pressing additives can be considered, however its easy removal has to be guaranteed.

The homogeneity of the TixZrH_2 samples was ensured by a prior milling process and a heat treatment with water quenching. A bi-modal microstructure with equiaxed α grains and α/β colonies formed. EDX mappings showed a partition of Zr, with higher content in the colonies transformed from β grains. Therefore, a slight β stabilizing effect of Zr could be observed, contrary to the categorization as a neutral element. As hydrogen in titanium can cause embrittlement, dehydrogenation is necessary to release hydrogen when using ZrH_2 as the Zr source. XRD analysis did not detect any hydrides, Zr or Ti, in the samples, indicating a successful dehydrogenation by vacuum sintering at 1100 °C for 3 h.

In hot extrusion, the dissolution of ZrO_2 particles posed a problem as heat treatment was necessary to ensure a homogeneous composition. The chosen heat treatment at 1000 °C for 24 h was not sufficient to reach complete dissolution, however a significant improvement was observed with respect to homogeneity.

The successful incorporation of Zr into the α-Ti lattice was confirmed by the increasing lattice parameters a and c, resulting in a leftward shift of the peaks with increasing Zr content. As Zr is a substitutional element the c/a ratio remained constant at 1.58, the value of pure Ti.

The hardness HV10 measurements show an initial decrease with the addition of Zr. The addition of 3 wt% Zr to the Ti6.5Cu matrix resulted in a hardness of approximately 300 HV10, a decrease of 20 HV10 compared to Ti6.5Cu. To increase the hardness above that of the matrix, the addition of 15 wt% Zr is required. A similar trend can be observed in the TixZr sample series. This indicates an increase in ductility, which is beneficial for the wire production used in WAAM. The TixZrO_2 sample series show steep increase in hardness with increasing alloying content. This can be attributed to the hardening effect of oxygen, which leads to a reduction in ductility.

The deformation dilatometry tests conducted with the produced alloys did not show a softening process, such as dynamic recovery or dynamic recrystallisation, as indicated by the literature. Therefore, further test at different temperatures and strain rates are necessary to investigate the deformation behaviour.

The cast material Ti5.9Cu2Fe2Al shows many impurities and inhomogeneities, which can also be observed in the hot-extruded samples. The produced rods with a 4 mm diameter show a grain refinement compared to the hot-extruded rods with a 8 mm diameter, explaining the increasing hardness.

The caliber rolling of cast material Ti5.9Cu2Fe2Al at 800 °C showed an elongation of the microstructure in the rolling direction. The increase of rolling temperature to 1000 °C results in a refined subgrain structure due to dynamic recrystallization. The refinement can also be observed in the crystallite size analysis via Scherrer calculation. The crystallite size decreases with an increasing degree of deformation at both rolling temperatures. However, the samples series deformed at 1000 °C experiences a significant decrease in crystallite size in the last deformation step, which can also be observed in the SEM. The microstructure change explains the high increase in hardness from 300 HV10 in the cast material to 520 HV after the last deformation step.

Zirconium was added to enhance ductility, thereby improving the mechanical properties for wire production while maintaining high strength. Consequently, further investigations are necessary to analyse mechanical properties, such as ductility, of the produced Ti-Zr alloys. In addition, accurate determination of the oxygen content is essential to better understand various material properties, including strength and ductility. However, such analyses were not performed in the present study, as they would have exceeded the scope of this work, and remain a subject of future investigations. Furthermore, microstructural stability — particularly the suppression of columnar grain growth — is crucial for the application of materials in WAAM. When this informations are available, it can be determined whether the alloys are suitable for wire production and thus for WAAM. To better understand the deformation behaviour of the investigated alloys, additional deformation dilatometry tests are needed, particularly at higher temperatures. These tests will help determine the parameters at which softening mechanisms, such as dynamic recrystallization, take place.

References

[1] M. Peters, J. Hemptenmacher, J. Kumpfert, C. Leyens in *Titanium and Titanium Alloys*, **2003**, pp. 1–36.

[2] J. C. Williams, R. R. Boyer, *Metals* **2020**, *10*, 705.

[3] T. Grover, A. Pandey, S. T. Kumari, A. Awasthi, B. Singh, P. Dixit, P. Singhal, K. K. Saxena, *Materials Today: Proceedings* **2020**, *26*, 3071–3080.

[4] U. Alonso, F. Veiga, A. Suárez, T. Artaza, *Metals (Basel)* **2020**, *10*, DOI 10.3390/met10010024.

[5] C. Yang, X. Shan, T. Xie, *The International Journal of Advanced Manufacturing Technology* **2016**, *83*, 645–655.

[6] G. Lütjering, J. C. Williams, *Titanium*, 2. ed., Springer, Berlin, **2007**.

[7] R. Boyer, G. Welsch, E. W. Collings, *Materials properties handbook : titanium alloys*, 1. print., ASM International, Metals Park, OH, **1994**.

[8] Z. Lin, K. Song, X. Yu, *Journal of Manufacturing Processes* **2021**, *70*, 24–45.

[9] T. Rodrigues, V. Duarte, R. M. Miranda, T. Santos, J. P. Oliveira, *Materials* **2019**, *12*, 1121.

[10] D. Zhang, D. Qiu, M. A. Gibson, Y. Zheng, H. L. Fraser, D. H. StJohn, M. A. Easton, *Nature* **2019**, *576*, 91–95.

[11] X. Wang, L.-J. Zhang, J. Ning, S.-J. Na, *Materials Science and Engineering: A* **2022**, *833*, DOI 10.1016/j.msea.2021.142316.

[12] R. RUH, *Journal of the American Ceramic Society* **1963**, *46*, 301–307.

[13] H.-C. Hsu, S.-C. Wu, Y.-C. Sung, W.-F. Ho, *Journal of Alloys and Compounds* **2009**, *488*, 279–283.

[14] T. Homma, Y. Matayoshi, R. Voskoboinikov, *Philosophical Magazine Letters* **2015**, *95*, doi: 10.1080/09500839.2015.1122243, 564–573.

[15] K. Kondoh, M. Fukuo, S. Kariya, K. Shitara, S. Li, A. Alhazaa, J. Umeda, *Journal of Alloys and Compounds* **2021**, *852*, DOI 10.1016/j.jallcom.2020.156954.

[16] A. Otsu, A. Doi, T. Onda, T. Kimura, T. Nakamoto, Z.-C. Chen, *Additive Manufacturing* **2024**, *85*, 104170.

[17] Y. Alshammari, Y. Alkindi, B. Manogar, F. Yang, L. Bolzoni, *Materials Science and Engineering: A* **2022**, *853*, DOI 10.1016/j.msea.2022.143768.

[18] V. Z. Shemet, V. A. Lavrenko, O. A. Teplov, V. Z. Ratushnaya, *Oxidation of Metals* **1992**, *38*, 89–98.

[19] C. Jiménez, F. Garcia-Moreno, B. Pfretzschner, M. Klaus, M. Wollgarten, I. Zizak, G. Schumacher, M. Tovar, J. Banhart, *Acta Materialia* **2011**, *59*, 6318–6330.

[20] H. Liu, P. He, J. C. Feng, J. Cao, *International Journal of Hydrogen Energy* **2009**, *34*, 3018–3025.

[21] K. Kondoh, I. Ammarueda, S. Kariya, L. Shufeng, A. Abdulaziz, J. Umeda, *World PM2022 – Session 12 : Light Materials - Titanium Alloys* **2022**.

[22] A. Issariyapat, J. Huang, T. Teramae, S. Kariya, A. Bahador, P. Visuttipitukul, J. Umeda, A. Alhazaa, K. Kondoh, *Additive Manufacturing* **2023**, *73*, 103649.

[23] K. Kondoh, S. Kariya, A. Khantachawana, A. Alhazaa, J. Umeda, *Materials* **2021**, *14*, 6561.

[24] R. F. Domagala, S. R. Lyon, R. Ruh, *Journal of the American Ceramic Society* **1973**, *56*, 584–587.

[25] C. Han, Y.-c. Li, X.-g. Liang, L.-p. Chen, N. Zhao, X.-k. Zhu, *Transactions of Nonferrous Metals Society of China* **2012**, *22*, 1855–1859.

[26] H. Wipf, B. Kappesser, R. Werner, *Journal of Alloys and Compounds* **2000**, *310*, 190–195.

[27] A. San-Martin, F. D. Manchester, *Bulletin of Alloy Phase Diagrams* **1987**, *8*, 30–42.

[28] E. Tal-Gutelmacher, D. Eliezer, *JOM* **2005**, *57*, 46–49.

[29] D. Eliezer, T. H. Böllinghaus in *Gaseous Hydrogen Embrittlement of Materials in Energy Technologies*, *Vol. 2*, (Eds.: R. P. Gangloff, B. P. Somerday), Woodhead Publishing, **2012**, pp. 668–706.

[30] N. Eliaz, D. Eliezer, D. L. Olson, *Materials Science and Engineering: A* **2000**, *289*, 41–53.

[31] X. C. Goso, A. Kale, *Journal of the Southern African Institute of Mining and Metallurgy* **2011**, *111*, 203–210.

[32] H. Okamoto, *Journal of Phase Equilibria and Diffusion* **2011**, *32*, 473–474.

[33] D. J. Simbi, J. C. Scully, *Materials Letters* **1996**, *26*, 35–39.

[34] J. M. Oh, B. G. Lee, S. W. Cho, S. W. Lee, G. S. Choi, J. W. Lim, *Metals and Materials International* **2011**, *17*, 733–736.

[35] S. L. Semiatin, V. Seetharaman, I. Weiss, *JOM* **1997**, *49*, 33–39.

[36] T. Furuhara, B. Poorganji, H. Abe, T. Maki, *JOM* **2007**, *59*, 64–67.

[37] I. Weiss, S. L. Semiatin, *Materials Science and Engineering: A* **1999**, *263*, 243–256.

[38] T. Seshacharyulu, S. C. Medeiros, W. G. Frazier, Y. V. R. K. Prasad, *Materials Science and Engineering: A* **2000**, *284*, 184–194.

[39] M. Motyka, *Metals* **2021**, *11*, 481.

[40] P. J. Bania, *JOM* **1994**, *46*, 16–19.

[41] Q. Wang, C. Dong, P. K. Liaw, *Metallurgical and Materials Transactions A* **2015**, *46*, 3440–3447.

[42] S. S. Sidhu, H. Singh, M. A.-H. Gepreel, *Materials Science and Engineering: C* **2021**, *121*, 111661.

[43] B. Friedrich, PhD thesis, Technische Universität Wien, **1993**.

[44] M.-K. Han, M.-J. Hwang, M.-S. Yang, H.-S. Yang, H.-J. Song, Y.-J. Park, *Materials Science and Engineering: A* **2014**, *616*, 268–274.

[45] X. Bao, X. Li, J. Ding, X. Liu, M. Meng, T. Zhang, *Materials Letters* **2022**, *318*, 132091.

[46] K. Banjongaxsorn, A. Khantachawana, C. Watanabe, K. Srirussamee, K. Kondoh, *Powder Metallurgy* **2023**, *66*, 472–481.

[47] I. W. S. P. G. Michael Schmid, Vapor Pressure Calculator, `https://www.tuwien.at/en/phy/iap/tools/vapor-pressure-calculator`, (accessed: 11.05.2025).

[48] T. Homma, A. Arafah, D. Haley, M. Nakai, M. Niinomi, M. Moody, *Materials Science and Engineering* **2018**, *709*, 312–321.

[49] S. Huang, J. Zhang, Y. Ma, S. Zhang, S. S. Youssef, M. Qi, H. Wang, J. Qiu, D. Xu, J. Lei, R. Yang, *Journal of Alloys and Compounds* **2019**, *791*, 575–585.

[50] M. Nico, MA thesis, Technische Universität Wien, **2023**.

[51] S. Haghighi, H. B. Lu, G. Y. Jian, G. H. Cao, D. Habibi, L. Zhang, *Materials Design* **2015**, *76*, DOI `10.1016/j.matdes.2015.03.028`.

[52] P. Jedrasiak, H. Shercliff, *Journal of Materials Science Technology* **2021**, *76*, 174–188.

[53] M. O. Bodunrin, L. H. Chown, J. W. van der Merwe, K. K. Alaneme, *International Journal of Material Forming* **2019**, *12*, 857–874.

[54] M. Dikovits, C. Poletti, F. Warchomicka, *Metallurgical and Materials Transactions A* **2014**, *45*, 1586–1596.

[55] V. I. Alekseev, B. K. Barakhtin, G. A. Panova, *Russian Metallurgy (Metally)* **2020**, *2020*, 1575–1578.

[56] I. Balasundar, T. Raghu, B. P. Kashyap, *Materials Science and Engineering: A* **2014**, *600*, 135–144.